ELEMENT-ROTATED AND MULTI-BEAM ANTENNA ARRAY DESIGN FOR WIRELESS COMMUNICATIONS

by

Ming Li

A thesis submitted in partial fulfilment of the requirements for the degree of

Doctor of Philosophy

in

Engineering

under the supervision of

Prof. Y. Jay Guo

to

School of Electrical and Data Engineering

Faculty of Engineering and Information Technology

University of Technology Sydney

NSW - 2007, Australia

June 2023

CERTIFICATE OF ORIGINAL AUTHORSHIP

I, Ming Li, declare that this thesis is submitted in fulfilment of the requirements for the award of DOCTOR OF PHILOSOPHY, in the Faculty of Engineering and Information Technology at the University of Technology Sydney.

This thesis is wholly my own work unless otherwise referenced or acknowledged. In addition, I certify that all information sources and literature used are indicated in the thesis.

This document has not been submitted for qualifications at any other academic institution.

This research is supported by the Australian Government Research Training Program.

Signature: Production Note: Signature removed prior to publication.

Date: 13/06/2023

Abstract

Antenna arrays play a significant role in many aspects of our lives, including wireless mobile communications, sensing, radio astronomy, etc. Researchers worldwide have developed many array pattern synthesis methods over the past decades. Most of them optimize both the excitation amplitudes and phases to achieve better performances, consequently increasing the complexity and cost of the beamforming networks. To facilitate simplified feeding networks, this dissertation presents several novel array synthesis methods that can be categorized into two parts.

The first part develops an antenna rotation technique. The rotation of an antenna can be regarded as approximated amplitude weighting to its co- and cross-polarized components. By properly rotating antennas in an array, favorable radiation patterns can be achieved. Specifically, a novel approach to synthesizing sum-and-difference patterns by rotating dipole antennas and adjusting their positions with linear arrays is first presented. Then the element rotation technique is extended to synthesize shaped patterns for linear and planar arrays considering mutual coupling. After that, the element rotation technique is further extended to deal with cylindrical conformal array synthesis. These approaches replace the traditional excitation amplitude weighting with the rotation of antennas for array synthesis, which significantly reduces the complexity and cost of the beamforming networks.

The second part of this dissertation focuses on multi-beam array synthesis. As a key technology for the fifth-generation (5G) wireless communication networks, multi-

beam antennas have drawn increased attention recently. A phase-only method based on a partitioned iterative Fourier transform (PIFT) method is presented to efficiently synthesize multi-beam patterns for uniformly spaced phased arrays. To achieve accurate beam control, the PIFT integrates a partitioned beam calibration strategy to calibrate the multi-beams individually without affecting each other. Additionally, multi-beam synthesis by utilizing the generalized joined coupler matrix (GJC) is presented. The GJC matrix is a recently developed matrix that can generate independently and individually scannable multi-beams using low-power-consumption and cost-effective analogue feeding networks. However, similar to other matrices, the lower beams will significantly distort and even split when they approach an upper beam. In this dissertation, an effective strategy of using reconfigurable directional couplers is adopted to address the beam splitting and to achieve continuously scannable multi-beams with a flexible synchronized optimization strategy.

Since modern wireless communication systems are evolving to be high-integration and low-cost ones, it is believed that the developed techniques could be highly attractive for numerous applications in both current and future terrestrial and non-terrestrial wireless communications.

ACKNOWLEDGMENTS

The past three and a half years have been one of the most valuable journeys in my life, despite that the outbreak of Covid-19 disrupted many of my plans. Throughout this unforgettable journey, I have gained immense knowledge and personal growth by collaborating with numerous intelligent and supportive professors, doctors, and friends. Their unwavering assistance and guidance have played a pivotal role in the completion of this thesis. I would like to express my deepest gratitude and heartfelt appreciation to all of them.

First of all, I would like to express my deepest gratitude to my supervisor, Prof Y. Jay Guo. Growing up in a small village, I had never imagined that I would have the opportunity to pursue a doctoral degree in Australia, such a beautiful country with hospitable people. Prof Guo provided me with this invaluable chance to study at the University of Technology Sydney (UTS), a young but creative university. As a researcher, he is so dedicated, experienced, and knowledgeable in multiple areas; as a supervisor, he is always supportive and has provided me a very free space so that I can do research I am interested in; as the director of the Global Big Data Technologies Centre (GBDTC), he has created an inclusive and positive research environment, where we can confidently grow to be qualified researchers. He is so wise and kind as well. I have learned a lot from him, and it is really my luck to work with him.

I want to express my sincere appreciation and gratitude to Prof Yanhui Liu, who is also a very knowledgeable, professional, and dedicated researcher. It was he who first led

me to the research world and ignited my passion for scientific research. He has offered me consistent guidance and help so that I can grow to be a dedicated researcher. I am greatly inspired by his rigorous academic attitude. His words and views about how to do good research influenced me a lot and will always remind me in the future.

I would like to thank Prof Richard W. Ziolkowski, Prof Bevan Jones, Prof Pei-Yuan Qin, and Dr Can Ding, for their insightful and profound suggestions on my works.

I am thankful to Dr Shu-Lin Chen for his suggestions and help with my research. He is so kind-hearted, enthusiastic, and always there when we need him. He is an outstanding researcher, an example who I should learn from. My thanks also goes to Dr Tianyu Yang, who first introduced me to UTS, and other members from the GBDTC, especially Dr Wei Lin, Dr He Zhu, Dr Jiwei Lian, Dr Lizhao Song, Dr Xuan Wang, Dr Maral Ansari, Yuenian Chen, Yubo Wen, Yang Xu, Fanchao Zeng, Xingyu Cheng, Gengming Wei, Yi He, Shang-Yi Sun and Zhaoqi Cui, for their kind help and support.

I am also thankful to my collaborators, seniors, and juniors in China, especially Dr Pengfei You, Dr Foxiang Liu, Yang Peng, Wei Zhang, JingJing Bai, Dingzhao Chen, Liyang Chen, Pan Wu, Zhimin Bao, Bin Kong, Rongxiang Guo, Siqing Liu, for their support in these years.

I would like to express my gratitude to my friends who are always there when I need them. Your help and accompany have made the three years messed up by the Covid-19 more meaningful and pleasant.

Finally, I would like to express my forever thankfulness to my parents, Jiating Li and Shuling Deng, for their unconditional love and support throughout my life.

List of Publications

Peer-reviewed Journal Articles :

1. **Ming Li**, Yanhui Liu, and Y. Jay Guo, "Design of Sum and Difference Patterns by Optimizing Element Rotations and Positions for Linear Dipole Array," *IEEE Transactions on Antennas and Propagation*, vol. 69, no. 5, pp. 3027-3032, May 2021.

2. **Ming Li**, Yanhui Liu, Shu-Lin Chen, Jun Hu, and Y. Jay Guo, "Synthesizing Shaped-Beam Cylindrical Conformal Array Considering Mutual Coupling Using Refined Rotation/Phase Optimization," *IEEE Transactions on Antennas and Propagation*, vol. 70, no. 11, pp. 10543-10553, Sep. 2022.

3. **Ming Li**, Yanhui Liu, Zhiming Bao, Liyang Chen, Jun Hu, and Y. Jay Guo, "Efficient Phase-Only Dual- and Multi-Beam Pattern Synthesis with Accurate Beam Direction and Power Control Employing Partitioned Iterative FFT," *IEEE Transactions on Antennas and Propagation*, vol. 71, no. 4, pp. 3719-3724, Apr. 2023.

4. Yanhui Liu*, **Ming Li***, Randy L. Haupt, Y. Jay Guo, "Synthesizing Shaped Power Patterns for Linear and Planar Antenna Arrays Including Mutual Coupling by Refined Joint Rotation/Phase Optimization," *IEEE Transactions on Antennas and Propagation*, vol. 68, no. 6, pp. 4648 - 4657, Jun. 2020.

5. Yang Peng, Yanhui Liu, **Ming Li**, Haiwen Liu, and Y. Jay Guo, "Synthesizing Circularly Polarized Multi-beam Planar Dipole Arrays with Sidelobe and Cross-

Polarization Control by Two-Step Element Rotation and Phase Optimization," *IEEE Transactions on Antennas and Propagation*, vol. 70, no. 6, pp. 4379-4391, Jun. 2022.

6. Dingzhao Chen, Yanhui Liu, **Ming Li**, Pan Guo, Zhuo Zeng, Jun Hu, and Y. Jay Guo, "A Polarization Programmable Antenna Array," *Engineering*, May 2022.

7. Yanhui Liu, Jinxiang Zheng, **Ming Li**, Qianke Luo, Yin Rui, and Y. Jay Guo. "Synthesizing Beam-Scannable Thinned Massive Antenna Array Utilizing Modified Iterative FFT for Millimeter-Wave Communication," *IEEE Antennas Wireless Propagation Letter*, vol. 11, no. 11, pp. 1983-1987, Nov. 2020.

8. Yanhui Liu, Yuqi Yang, Pan Wu, Xinyu Ma, **Ming Li**, Kai-Da Xu, and Y. Jay Guo, "Synthesis of multibeam sparse circular-arc antenna arrays employing refined extended alternating convex optimization," *IEEE Transactions on Antennas and Propagation*, vol. 69, no. 1, pp. 566-571, Jan. 2021.

PEER-REVIEWED CONFERENCE ARTICLES :

9. **Ming Li** and Yanhui Liu, "Saddle-Shaped Pattern Synthesis by Element Rotation and Phase Optimization for Linear Dipole Array," *International Applied Computational Electromagnetics Society (ACES-China) Symposium*, Chengdu, 2021.

10. **Ming Li**, Yanhui Liu, Shu-Lin Chen, Jun Hu, and Y. Jay Guo, "Element-Rotated Linear, Planar, and Conformal Arrays Radiating Shaped Patterns," *International Applied Computational Electromagnetics Society Symposium (ACES-China)*, Chengdu, 2021. (*First Prize of the Student Paper Competition*).

11. Dingzhao Chen, **Ming Li**, Pan Guo, and Yanhui Liu, "A Novel Multi-Linear Polarization Reconfigurable Antenna Array," *IEEE Asia-Pacific Conference on Antennas and Propagation (APCAP)*, Xiamen, 2022.

12. Bin Kong, Yanhui Liu, and **Ming Li**, “Binary Coded Genetic Algorithm Application for Array Diagnosis,” *International Conference on Microwave and Millimeter Wave Technology (ICMMT)*. Nanjing, 2021.

Table of Contents

List of Figures

Figure **Page**

List of Tables

Table **Page**

ABBREVIATIONS

5G - fifth generation

6G - sixth generation

AC - alternating current

B5G - beyond fifth generation

BFN - beamforming network

CoP - co-polarized

CP - circular polarization

CPM - contiguous partition methods

CPU - centre processing unit

DDE - dynamic differential evolution

FFT - fast Fourier transform

GA - genetic algorithm

GB - Gigabyte

GCS - global coordinate system

GJC - generalized joined coupler

HFSS - high-frequency structure simulator

HGAIFT - hybrid genetic algorithm and iterative Fourier transform

HGAIFT - hybrid genetic algorithm and modified iterative Fourier transform

IFFT - inverse fast Fourier transform

IFT - iterative Fourier transformation

JCAS - joint communications and radar/radio sensing

LCS - local coordinate system

MIFT - modified iterative Fourier transformation

MIMO - multiple-input multiple-output

MB - Megabyte

MBAA - multi-beam antenna array

PIFT - partitioned iterative Fourier transformation

PSO - particle swarm optimization

PTMP - point-to-multipoint

Q-PIFT - quantized partitioned iterative Fourier transform

RAM - random access memory

RF - radio frequency

RMSE - root mean squared error

RR - randomly rotated

SA - simulated annealing

SCM - single co-ordinate method

SLL - sidelobe level

SQP - sequential quadratic programming

SR - sequentially rotated

VAEP - vectorial active element pattern

XP - cross-polarized

XPL - cross-polarization level

LIST OF SYMBOLS

D_p - the number of variables in PSO

e - natural base

E - element electrical pattern

F - array pattern

f_c - frequency

f_c - cost function

f_{Int} - interpolation function

I_m - the number of iterations

j - imaginary unit

M - beam number

N - element number

N_p - the number of particles in PSO

P - the number of sampling points for the 1D/2D FFT

$\vec{p}_d$ - desired polarization direction unit vector

$\vec{p}_{co}$ - co-polarization unit vector

$\vec{p}_X$ - cross-polarization unit vector

Q - the number of sampling points for the 2D FFT

$\vec{r}$ - element position vector

T - matrix transpose

$\vec{u}$ - propagation unit vector

$\mathbf{w}$ - complex excitation vector

W - weighting factor

x_n - the n^{th} element position along x-axis

β - wavenumber

Γ_{SLL} - target sidelobe level

Γ_{XPL} - target cross-polarization level

Γ_P - target peak power

Γ_{slope} - target slope of the difference pattern

η_t - efficiency

ϵ_r - relative dielectric constant

θ - elevation angle

λ - wavelength

ξ - element rotation angle

ϕ - azimuth angle

φ - excitation phase

CHAPTER 1

INTRODUCTION

As the primary devices for transmitting and receiving electromagnetic waves, antennas are ubiquitous in our daily life. They utilize their structures to convert alternating current (AC) signals or guided waves on the transmission line into electromagnetic waves propagating in space, and vice versa [1]. A single antenna element (except for some special antennas like the lens antenna and the reflector antenna) often has limitations, such as low gain and high sidelobe level (SLL). In many wireless applications, however, high directivity or gain and flexible beam scanning ability are necessary. In such situations, a single antenna element is no longer suitable, and antenna arrays become imperative.

An antenna array is a system consisting of at least two antenna elements arranged in a specific configuration. Element antennas in the array operate based on the principle of interference superposition of the electromagnetic waves. Appropriate excitations can be fed to the antenna elements to obtain desired radiation characteristics for the array. In comparison to a single antenna element, an array pattern can be modulated through proper synthesis techniques that determine the excitations or positions for array

elements in order to have particular pattern characteristics for target applications. Array antennas have found many significant applications in mobile communications, radio, and television, navigation, radio astronomy, etc. They offer many advantages, including not only high gain and low SLL, but also complicated pattern modulations like beam steering, anti-interference nulling, multibeam, and beam shaping [2, 3].

1.1 Motivation and Scope

The development of modern terrestrial and non-terrestrial wireless communication networks has brought increasing demand on both array pattern performance as well as antenna array system itself. In terms of the array pattern performance, relatively low SLL is generally required to minimize the influence of noises and interferences from the environment. Besides, particular main lobe shapes like flattop and cosecant-squared shaped patterns with gentle ripples, sum-and-different patterns with steep slopes for the difference pattern, and multi-beam patterns are needed in many applications, including base stations for cellular communications networks, satellite communication, sensing, and imaging systems.

To meet those demands, many methods were developed in the past decades [4–18]. Most of them optimized both excitation amplitudes and phases in order to obtain good main lobe shapes and relatively low SLLs. As a result, the yielded excitation amplitudes generally had a relatively large dynamic range ratio. Although the dynamic range ratio can be reduced by employing some effective methods, nonuniform power dividers are still required in the beamforming network. As a consequence, it will not only increase the complexity of the beamforming network design but also increase the cost for the whole antenna array system.

Element rotations can serve as an available degree of freedom that can be exploited in the array pattern synthesis. Several studies have been presented in the past decade for

pattern synthesis by using the element rotation technique [19–24]. They have achieved outstanding array pattern performances. However, they only considered focused-beam patterns, and most of them did not consider mutual coupling as well as realistic antenna structure. In order to meet the above-mentioned demands, in the dissertation, the element rotation technique is first exploited to synthesize shaped-beam and sum-and-difference patterns. By replacing the excitation amplitude weighting with the rotation of antenna elements, it is shown that almost equivalent pattern performances can be achieved with much-simplified feeding networks by casting off many unequal power dividers.

Another topic that will be studied in this dissertation is the multi-beam antenna array (MBAA) design with simplified and cost-effective feeding networks. The MBAA is able to generate a number of independent directive beams to cover multiple angular ranges. It has significant applications in modern terrestrial and non-terrestrial wireless communication networks such as the fifth-generation (5G), point-to-multipoint (PTMP) data transmission and broadcasting, satellite communication, and sensing [25]. Especially in 5G wireless communications, MBAA is the key infrastructure to achieve the required independent beamforming that boosts the 5G [26].

Specifically, there are two kinds of multi-beams. One is to generate a radiation pattern with multiple simultaneous focused beams employing one set of excitations. The other is to generate multiple patterns with multiple sets of excitations, each of which affording one focused-beam pattern. Both of these two types of multi-beams are considered in this dissertation. For the former one, a fast phase-only synthesis method based on a partitioned iterative Fourier transform (PIFT) is presented to obtain multi-beam patterns with accurate beam directions. For the latter one, the beam splitting issue when dual or multiple beams are overlapping for the generalized joined coupler (GJC) matrix is first investigated, and a synchronized optimization strategy employing

reconfigurable directional couplers is presented to address the issue and to obtain continuously scannable multi-beam patterns with reduced SLLs.

In summary, this dissertation focuses on the following several main topics:

- 1. Sum and difference patterns synthesis for linear dipole arrays by optimizing element rotations and positions;
- 2. Shaped power pattern synthesis for linear and planar arrays considering mutual coupling with a refined joint rotation and phase optimization method;
- 3. Shape power pattern synthesis for cylindrical conformal arrays considering mutual coupling by a refined element rotation and phase optimization method;
- 4. Efficient and accurate phase-only multi-beam pattern synthesis for linear arrays based on the PIFT.
- 5. Optimization of the GJC matrix to achieve continuously scannable multi-beams with reduced SLLs.

1.2 Statement of Contributions

This dissertation presents several novel techniques to synthesize desired patterns with simplified and cost-effective feeding networks. Particularly, key contributions of this dissertation include exploiting the rotations of antenna elements to synthesize desired array patterns like sum-and-difference patterns and shaped patterns. Contributions also include synthesizing accurate multi-beam patterns employing the PIFT and optimization of the GJC matrix to achieve continuous multibeam steering. Detailed contributions are outlined below:

The first contribution is to present a sum and difference patterns synthesis method by employing the element rotation technique. The particle swarm optimization (PSO)

method is used to optimize the antenna rotation angles and positions of linear dipole arrays to yield sum and difference patterns. Besides, reduced SLL and constrained cross-polarization level (XPL) can be achieved. Moreover, the difference pattern slope is also optimized to be as steep slope as possible. It can result in sum-and-difference patterns arrays with sparsely distributed elements of uniform amplitude, thereby saving many unequal power dividers and antenna elements. It is shown that the synthesized arrays are able to radiate favorable sum and difference patterns meanwhile saving 34.69%-42.27% antenna elements comparing to half-wavelength-spaced arrays.

The second contribution is to present a refined element rotation and excitation phase optimization method to synthesize shaped power patterns for linear and planar antenna arrays considering mutual coupling. Vectorial active element patterns (VAEPs) are used, and the rotation of an element is approximately described by mathematically rotating its VAEP under the assumption that the mutual coupling from nearby elements remains unchanged during the rotation. Then the element-rotated array pattern can be approximately obtained by weighted summation of all the rotated VAEPs. Optimal element rotations and phases can be found by solving a vectorial shaped pattern synthesis problem such that desired shaped pattern with constrained SLL and XPL can be obtained. However, owing to the mutual coupling change, the synthesized pattern may deviate much from the real one. To improve the accuracy, several steps of successive refined joint element rotation/phase optimizations are conducted. The allowable rotation angle range is set smaller and smaller as the refining steps increases to improve the accuracy. Such a shaped power pattern synthesis technique does not need nonuniform amplitude weighting, thus saving many unequal power dividers. Examples of synthesizing shaped-beam linear and planar arrays with different antenna structures as well as pattern shape requirements are provided. Full-wave simulations and measurements are conducted to validate the synthesized results.

The third contribution is to extend the element rotation method to the shaped pattern synthesis for cylindrical conformal arrays. The pattern of an antenna element rotated on a curved surface is approximately described by mathematically rotating the VAEP of this element when without rotation. Coordinate transformation and scattered interpolation are employed to express all the rotated VAEPs at a unified angle sampling grid in a common global coordinate system (GCS), and then, the approximated array pattern can be calculated by summing the interpolated rotated VAEPs at the same sampling grid. Optimal element rotations and phases affording desired shaped pattern with controlled SLL and XPL can be found by using the PSO with the approximated array pattern expression. After that, a refined strategy is adopted to successively improve the accuracy of the synthesized pattern. The developed method can obtain shaped patterns for cylindrical conformal arrays by optimizing element rotations and phases only, and no amplitude weighting is required, thus saving many unequal power dividers. Three typical shaped patterns are synthesized for cylindrical arrays. A prototype of a cylindrical array with 24 rotated U-slot loaded patch antennas is fabricated and measured for validation.

The fourth contribution is to present a novel phase-only method based on the PIFT to efficiently synthesize radiation patterns with dual or multiple concurrent focused beams for uniformly spaced linear arrays. To achieve accurate main lobe peak directions, the PIFT integrates a partitioned beam calibration strategy into the iterative Fourier transform (IFT) to iteratively calibrate the beams by partitioning the multi-beam pattern into multiple single-beam patterns and calibrating them individually. In addition, the main lobes as well as the sidelobes of the multi-beam patterns are iteratively modified to achieve desired peak gains and relatively low SLLs. Several examples are presented to demonstrate the effectiveness and efficiency of the developed method. Comparisons to the convention IFT and other phase-only methods are presented for comprehensive evaluation of the proposed method. Mutual coupling can also approximately considered,

and full-wave simulations have demonstrated the validity of the PIFT method.

The fifth contribution is to present a novel synchronized optimization strategy for the design of the GJC matrix to achieve continuous multibeam steering with reduced SLLs. The beam distortion and splitting problem when multi-beams overlap for the GJC matrix is thoroughly investigated for the first time. An effective strategy of using reconfigurable directional couplers is adopted to address this issue and to achieve continuously scannable multi-beams. To this end, a flexible synchronized optimization strategy that can consider multiple cases where multi-beams can have different scanning angles is developed. In addition to the capability of addressing the beam splitting issue, consistent SLLs during scanning can also be achieved by using the developed method. Numerical results are provided to demonstrate the effectiveness of the developed method. Besides, comparison between the GJC matrix with a classical Blass matrix design method is presented.

Since a simple and cost-effective feeding system is key to the current and future terrestrial and non-terrestrial wireless communication networks, it is believed that the developed techniques in this dissertation can find a wide range of applications.

1.3 Organization of the Thesis

The structure of this dissertation is organized as follows:

In Chapter 2, relevant background and state-of-the-art works are reviewed.

In Chapter 3, a sum and difference pattern synthesis method which employs the element rotation technique is presented.

Chapter 4 presents a shaped pattern synthesis method based on element rotation and excitation phase optimization for linear and planar arrays.

In Chapter 5, the element rotation technique is extended to deal with shaped pattern synthesis for cylindrical conformal arrays.

Chapter 6 presents an accurate and efficient PIFT-based phase-only multi-beam pattern synthesis method.

In Chapter 7, the GJC matrix is optimized to yield continuously scannable multi-beam patterns by addressing the beam splitting issue.

Chapter 8 draws the conclusion.

CHAPTER 2

BACKGROUND AND STATE-OF-THE-ART

In this chapter, the backgrounds of the antenna array are discussed in the beginning. Then, detailed state-of-the-art works relevant to the array synthesis methods presented in this dissertation are reviewed to learn the backgrounds and the motivation of this dissertation.

2.1 Antenna Arrays and Their Far-Field Radiation Patterns

An antenna array is defined as a system of at least two antennas arranged in a specific layout [2]. Antenna elements in the array work together based on the principle of electromagnetic wave interference and superposition. According to the element distribution in the array, antenna arrays can be categorized into three types: linear array, planar array, and conformal array. Fig. 2.1 shows schematic diagrams of uniformly spaced linear, planar, and cylindrical conformal arrays. As can be seen, the elements (denoted by black dots) in the linear array are placed along a line, while those in the planar array are

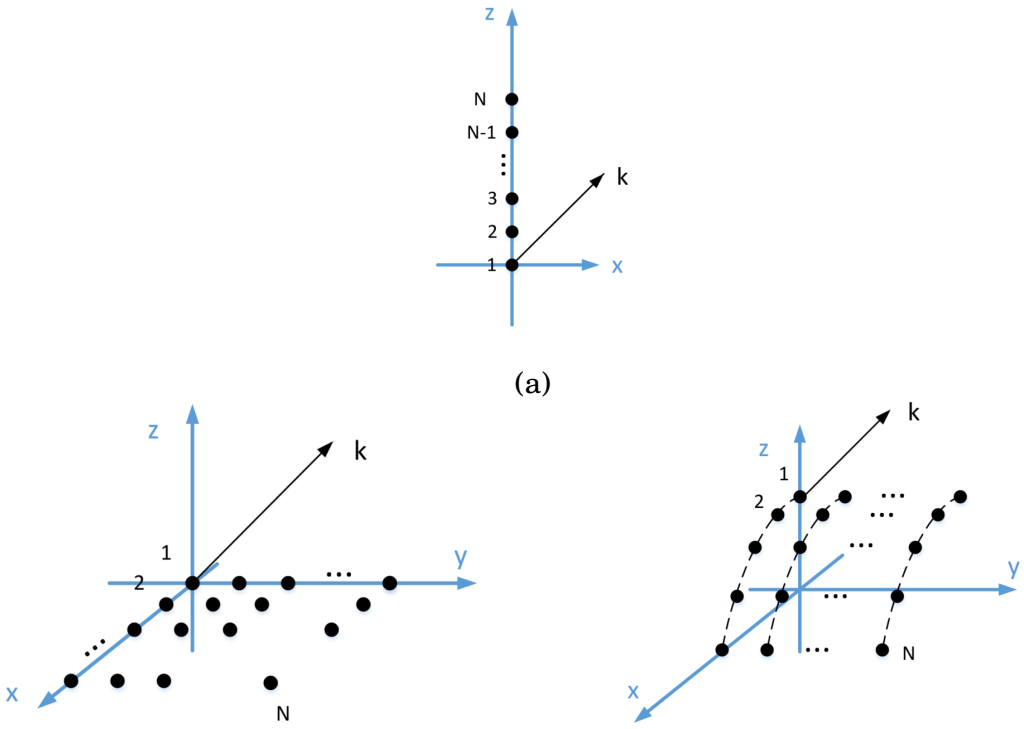

Figure 2.1: The schematic diagram of uniformly spaced (a) linear array, (b) planar array, and (c) conformal array.

placed on a plane. Particularly, in some applications, antenna elements are required to be tightly integrated onto curved surfaces such that the carriers can save much space or preserve their aerodynamic as well as hydrodynamic properties. Thus, conformal arrays are usually employed in these applications. According to the shape of the carrier, conformal arrays can be divided into spherical array, cylindrical array, conical array, etc. Fig. 2.1(c) shows the schematic diagram of a cylindrical conformal array.

Though having different element distributions, their array patterns can be expressed as a uniform equation. Generally, for an arbitrary antenna array, one can write the far-field pattern as [2]:

$$F(\mathbf{w};\theta,\phi) = \sum_{n=0}^{N-1} w_n E_n(\theta,\phi) e^{j\beta \vec{r}_n \cdot \vec{u}} \tag{2.1}$$

where $j = \sqrt{-1}$ is the imaginary unit, $\beta = 2\pi/\lambda$ is the propagation constant, with λ

being the wavelength in free space. $E_n(\theta,\phi)$ and $\vec{r}_n = [x_n, y_n, z_n]$ are the element pattern and position of the n^{th} element. $\vec{u} = [\sin\theta\cos\phi, \sin\theta\sin\phi, \cos\theta]$ is the propagation direction vector. $\mathbf{w} = [w_0, w_1, ..., w_{N-1}]^T$ is the complex excitation vector, where $[\cdot]^T$ denotes transpose of a matrix.

Traditional array synthesis is to find proper excitation vector $\mathbf{w}$ and/or element positions $\vec{r}_n$ to obtain desired pattern performance in terms of main lobe shape, side lobe level (SLL), and null for anti-interference, etc. In the past many years, a great many array synthesis methods have been developed. In the following, the state-of-the-art works associated with the contents that will be presented in this dissertation will be briefly reviewed.

2.2 State-of-the-Art

2.2.1 Sum-and-Difference Patterns Synthesis

Owing to the high demand in target tracking and positioning, antenna arrays radiating sum-and-difference patterns have received much attention in the past decades. The sum pattern, also known as the focused-beam pattern, has a peak in the target direction, whilst the difference pattern has a null therein. Together they play a very important role in detecting and tracking the potential target in wireless communications and monopulse radar systems [27]. The sum-and-difference patterns generally need to have high directivity for the sum pattern, a steep slope for the difference pattern, and low SLLs for both patterns in order to achieve high positioning and tracking accuracy.

A lot of advanced techniques and methods were developed for obtaining sum-and-difference patterns in the past several decades [28–34]. If the complexity and cost of a beam forming network (BFN) are affordable to the target application, classical methods like the Dolph-Chebyshev [28], the Bayliss approach [29], as well as some other methods

[30] that employ independent excitations will be adequate.

However, to result in a simplified BFN and reduce the system cost, compromised schemes to avoid two completely independent sets of excitations are preferred. In [31], a typical and common BFN known as two-section BFN shared by the sum and difference radiation modes is employed, and sum-and-difference patterns were synthesized by optimizing the excitation amplitudes. To achieve a sum pattern, one can apply identical phases to the two halves of the array. Similarly, a difference pattern can be obtained by feeding the two halves of the array with anti-phases. However, the sum-and-difference patterns produced by the two-section BFN have limited performance because only half of the excitation amplitudes can be optimized.

To improve the sum-and-difference patterns performance based on the two-section BFN, some researchers chose to additionally optimize the excitation phases and/or element positions along with the excitation amplitudes, such as those in [32, 33]. By doing so, they have achieved excellent performance, including steep slopes and relatively low SLLs. Besides, instead of sharing a common BFN, Morabito et al. chose to share only a part of excitation amplitudes between sum-and-difference modes to release more degrees of synthesis freedom [34], as shown in Fig. 2.2.

Another effective and widely-used approach to avoid two independent BFNs is using a subarray-based strategy. In such a strategy, the element excitations affording a required sum pattern are obtained at first (generally using either the Taylor or Dolph-Chebyshev approach). After that, the array is subdivided into a number of subarrays, and eventually, the difference pattern can be obtained by optimizing additional weights for the subarray outputs [35–39]. Based on the subarray-based strategy, the contiguous partition methods (CPM) in [35] and [36] and some stochastic optimization algorithms in [37–39] have been successfully employed to yield sum-and-difference patterns.

Despite their outstanding performance, most of the existing methods chose to opti-

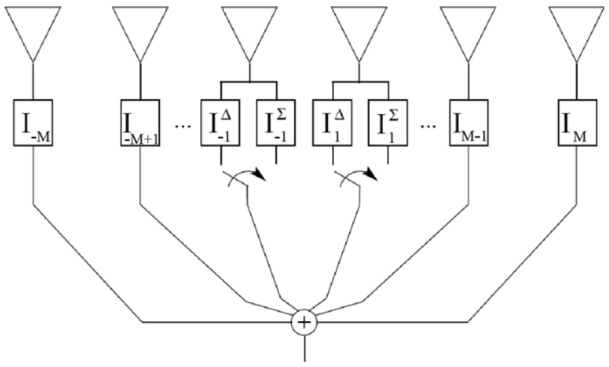

Figure 2.2: Array with partially switchable excitations for sum-and-difference modes [34]. I denotes element excitation in the figure.

mize the excitation amplitudes to acquire desired performance, such as low SLL and large slope. Consequently, they need multiple unequal dividers that lead to relatively complicated BFNs. To avoid nonuniform excitation amplitudes, a few methods have been presented for synthesizing a sum or difference pattern by using phase-only or joint phase and position optimization [40, 41]. However, these methods synthesize sum-and-difference patterns individually, which means that the BFNs for both of the patterns would not be shared [40, 41].

Simultaneously achieving good pattern performance and a simplified BFN has remained a challenge when aiming to achieve sum-and-difference patterns.

2.2.2 Shaped Power Pattern Synthesis for Linear and Planar Arrays

In applications such as satellite communications, sensing, and imaging systems, it is often necessary for the main lobes of antenna array radiation patterns to exhibit specific shapes, such as flat-top or cosecant-squared shapes, in order to achieve the desired spatial coverage with the desired power distribution. This requirement leads to the need for shaped-beam radiation patterns in these applications. Over the past decades,

numerous advanced methods have been developed to synthesize shaped patterns in antenna arrays. Owing to the fact that shaping an array pattern is quite a complicated process, most of the literature chose amplitude as one of the optimization variables.

The most classical methods of synthesizing shaped patterns are the Taylor and Woodward-Lawson methods [11, 12]. In the Taylor method, the distribution of a pencil beam with low SLL is obtained by using the Taylor method first. Then let the beams scan to the direction where the shaped region locates such that the sum of the scanned pattern will have a main lobe like a shape pattern. The angle values and the element weights can be determined, and by counting the shaped-beam pattern distribution with the new array factor function, the desired shaped pattern can be obtained [11]. Two patterns synthesized in [11], including a flat-top shaped and a cosecant-squared shaped pattern, are given in Fig. 2.3 of this thesis. As can be seen, the pattern performance in terms of the ripple and the SLL is outstanding. The corresponding excitation amplitudes and phases are also included in Fig. 2.3. The Woodward-Lawson method is also an analytical method that optimizes the excitation amplitudes and phases to synthesize shaped patterns for line source array or discrete element array [12]. However, these two methods deal with uniformly spaced arrays only. Moreover, they are unable to take the mutual coupling and practical antenna structures into consideration.

In addition, a number of other methods, like the alternating projection methods [13, 14], iterative fast Fourier transform (FFT) and its variants [16, 42], convex optimization techniques [6, 43], semi-definite relaxation methods [18, 44], and stochastic optimization algorithms [45–49] are also good candidates for the shaped pattern synthesis. They generally can deal with nonuniformly distributed arrays with mutual coupling considered. Shaped patterns with excellent performance were obtained with these methods.

However, due to the intricate nature of shaped pattern synthesis compared to focused-beam pattern synthesis, most existing methods have opted to optimize both excitation

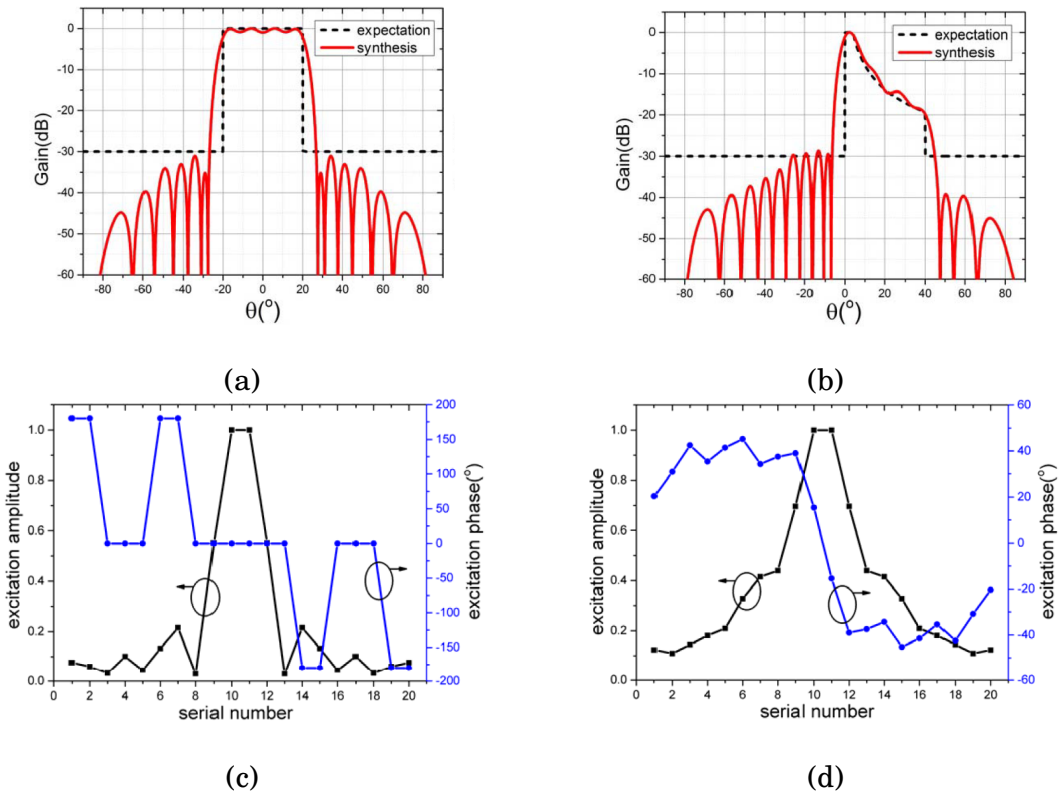

Figure 2.3: The flat-top and cosecant-squared patterns and their excitations obtained in [11] for a linear array of 20 elements. (a) flattop shaped pattern and (b) cosecant-squared shaped pattern, and their excitations (c) and (d), respectively.

amplitudes and phases to achieve precise control over the main lobe shape and SLL. Consequently, the resulting shaped-beam pattern array typically requires a complex feeding network to implement nonuniform element amplitudes, often with a large dynamic range ratio. The design of multiple unequal power dividers becomes necessary, requiring careful attention and leading to increased weight and system cost.

To circumvent the use of unequal power dividers, several methods have been proposed to achieve shaped beam patterns through phase-only optimization, such as those in [41, 50–52]. Owing to the limited degrees of freedom, however, the obtained overall performance in terms of main lobe shape accuracy, transition width, and SLL is usually considerably worse than those obtained with full control of both the excitation amplitudes and phases. As can be seen in Fig. 2.4(a) and (b), which were obtained with phase-only

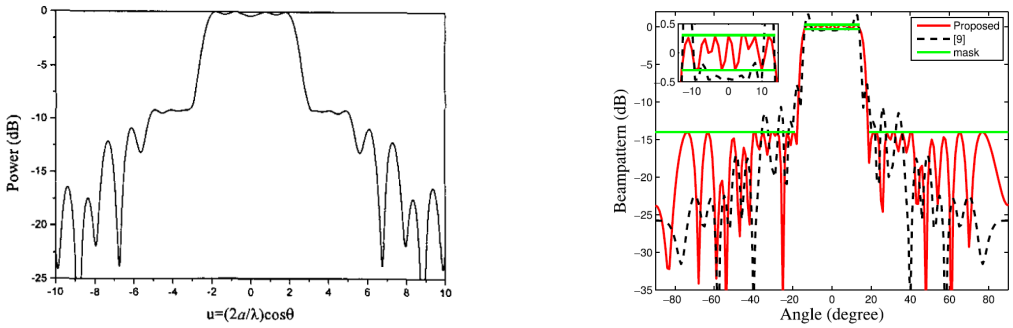

(a) (b)

Figure 2.4: The flat-top patterns obtained by phased-only methods in [41] and [52], respectively. (a) shows the pattern obtained in [41] with a 5λ-long line source and (b) is obtained in [52] for a linear array of 32 elements.

methods in [41] and [52], the SLLs are much higher than those obtained in the amplitude optimization method. The insufficient optimization degrees of freedom resulting from using excitation phase as the sole variable contribute to this disparity. In [53], element positions along with the excitation phases were optimized to improve the performance of the shaped pattern synthesis.

Further research is highly desired to synthesize shaped patterns with reduced SLLs while using uniform excitation amplitudes to simplify the feeding network.

2.2.3 Shaped Pattern Synthesis for Conformal Arrays

Conformal arrays are those required to be tightly integrated onto curved surfaces such that the carriers can save much space and preserve their aerodynamic and hydrodynamic properties. Shaped pattern synthesis for conformal arrays has been receiving considerable attention for their significant applications in space navigation and wireless communications. Synthesizing shaped power patterns for conformal arrays is more complicated than that for linear and planar arrays since elements in conformal arrays orient in different directions, and the array factor is no longer independent of the element radiation pattern. Despite its complexity, many techniques have been proposed to synthesize

shaped patterns for conformal array due to the high demands [54–57].

In [54], a modified least-squares optimization method was introduced. This method involved choosing the phases of non-zero values and non-zero constraint values through a rapid iteration process to achieve an optimal fit to the goal function amplitude. Such modification makes the least-squares optimization method a robust and fast synthesis method for large conformal arrays. In [55], an iterative linear programming method was proposed to synthesize patterns for an arbitrary array. As an example, the author synthesized a 3D cosecant-squared pattern for an 8×8 cylindrical array by using the proposed method. The obtained results are given in Fig. 2.5. As can be observed that a relatively low SLL and small ripple were obtained, which demonstrated the effectiveness of the proposed method. A versatile Bayesian compressive sampling (BCS) method was presented in [56] to design sparse conformal arrays with shaped patterns. Such a strategy optimized the element arrangement of the conformal arrays. Within a probabilistic formulation, the sparsest array distribution was derived by employing a suitable generalization to the conformal architectures of the Bayesian method [56]. In addition, a generalized projection algorithm was applied in the reconfigurable shaped pattern synthesis with near-field constraints in [57]. The synthesized results demonstrated the effectiveness of this method in achieving the desired shaped pattern while satisfying the near-field constraints.

Despite their outstanding effectiveness, all the above-mentioned methods did not take the mutual coupling into consideration. There are many strategies that consider mutual coupling when synthesizing the shaped pattern for conformal array [43, 44, 58–61]. They include, for example, the semidefinite relaxation method [44, 58], the alternate projection [59], the second-order cone programming method [43], and the stochastic algorithms [60, 61]. In [44], a semidefinite relaxation method is extended to obtain a co-polarized (CoP) pattern with good main lobe shape and reduced SLL, meanwhile maintaining a

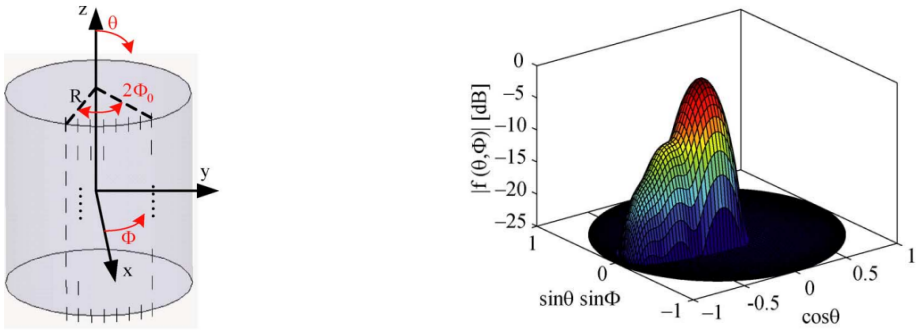

(a) (b)

Figure 2.5: The 8×8-element cylindrical array and the obtained cosecant-squared pattern in [55].

low cross-polarization level (XPL). The developed method considered mutual coupling by utilizing the vectorial element pattern. Several examples considering various array geometries and pattern requirements were provided. A circular flat-top shaped pattern synthesized for a cylindrical array is shown in Fig. 2.6. One can see that satisfactory results are obtained with arrays of realistic elements.

Again, most of these methods optimized excitation amplitudes to obtain desired patterns to get better main lobe and SLL performance. As a result, they will require unequal power dividers in the feeding network, thus increasing the complexity and cost of the array system. A method that can obtain satisfactory shaped patterns for the conformal array without using amplitude modulation is highly desired.

2.2.4 Dual- and Multi-Focused-Beam Shaped Pattern Synthesis

Multi-beam antenna arrays with multiple flexibly scannable beams are identified as a key technology for the fifth-generation (5G) and sixth-generation (6G) wireless communication and have undergone extensive development in recent years [26, 62, 63]. There are two kinds of multi-beams for antenna arrays. One of them is using phased arrays to generate multi-focused-beam shaped patterns. In other words, only one set of excitation is required to obtain a radiation pattern with multiple focused beams. It can be regarded

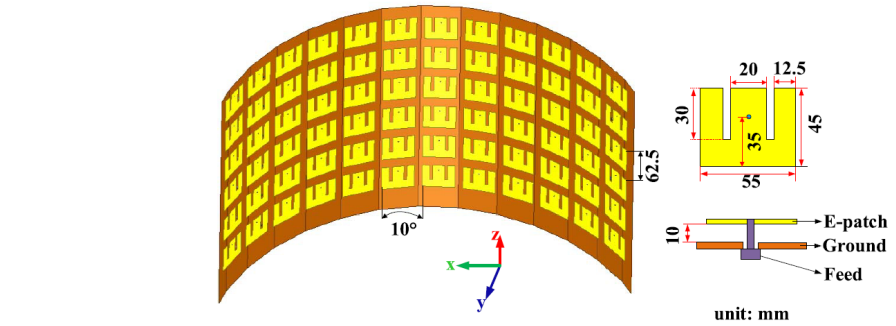

(a)

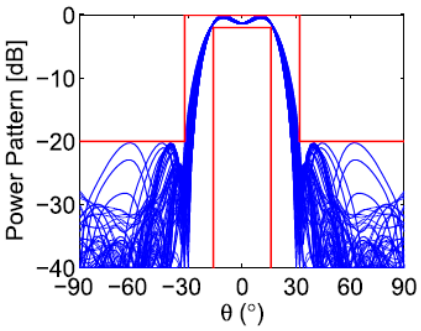

(b)

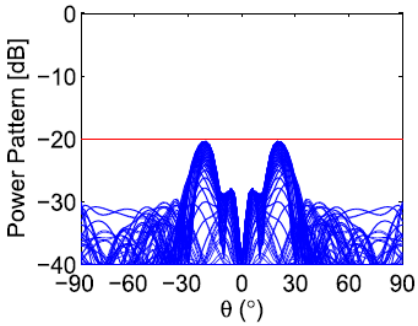

(c)

Figure 2.6: The cylindrical conformal array with 6×12 E-shaped patch antennas (a), and the synthesized flat-top shaped CoP pattern (b) and XP pattern (c) [44].

as a special case of shaped pattern, which can usually be used to achieve two or multiple small angular coverages. Fig. 2.7 shows an example with dual focused beams.

Antenna arrays that can radiate a pattern with dual or multiple focused beams have been widely applied in many significant applications, typically in point-to-multipoint (PTMP) data transmission, PTMP broadcasting, reconfigurable reflecting surface-assisted wireless communications, and multi-target vital-signs monitoring [64–66]. A simple but effective way of generating a dual-focused-beam pattern is to design a single antenna element that can radiate dual concurrent beams, like those in [67–69]. However, a single antenna element is very limited both in gain and beam steering flexibility, which makes it hardly attractive in long-range communication with mobile users. Antenna arrays, which can generate high-directivity, flexibly steerable, and narrower beams, are much preferable in most multibeam applications.

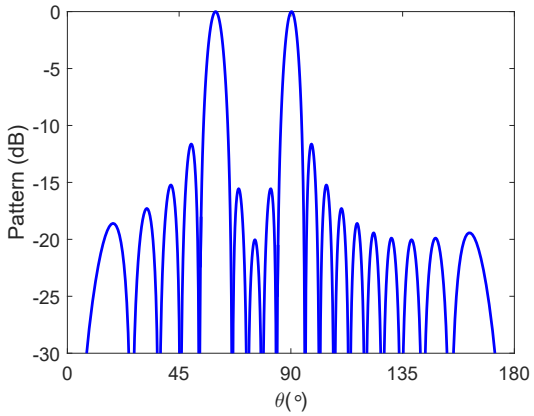

Figure 2.7: An array pattern with dual focused beams.

Over the past many years, many sophisticated methods were developed to synthesize multibeam antenna arrays [26, 70–79]. For example, in [72], an auxiliary function with a desired amplitude pattern and a generic phase pattern was adopted, and the multibeam pattern was obtained by iteratively modifying the phase pattern. In [73], by perturbing locations of the array factor zeros, multibeam patterns with low SLLs were obtained. However, to obtain multibeam patterns with desired beam directions as well as low SLLs, these methods optimized both the excitation amplitudes and phases. Moreover, the resulting excitation amplitudes could fluctuate severely, and the amplitude dynamic range ratio could be considerably large due to the complexity of generating a multibeam pattern, thus leading to complicated feeding networks and low aperture efficiency.

To maintain the simplicity of the array system, a few attempts have been made to synthesize dual or multibeam patterns using uniform excitation amplitudes [72, 74, 76–78]. For example, in [77], the grating lobes were developed to generate a dual-beam pattern. However, for determined element distribution, dual beams obtained using grating lobes will always have fixed distance in uv-space ($u = \sin\theta\cos\phi$, $v = \sin\theta\sin\phi$), which greatly restricts the beam steering flexibility. To achieve flexibly steerable beams, several works have been reported to synthesize dual- or multibeam patterns employing phase-only method [72, 74, 76, 78]. In [72, 76], the single co-ordinate method (SCM) was

employed to efficiently synthesize dual-beam patterns for arbitrary array geometries by optimizing the excitation phases only. In [74], the sequential quadratic programming (SQP) algorithm was utilized to synthesize multibeam patterns with prescribed nulls for linear arrays. In [78], the neural networks based on a back-propagation algorithm were developed to synthesize multibeam patterns with adaptive nulls. However, these reported approaches are either time-consuming or unable to achieve accurate beam control and relatively low SLL.

An efficient phase-only method that can synthesize multiple-focused-beam shaped patterns with accurate beam directions and reduced SLLs for phased arrays is highly desired.

2.2.5 Multibeam Enabled by Analog Beamforming Matrix

The aforementioned multibeam with multiple focused beams in a radiation pattern will split the total gain of an antenna array. Another kind of multibeam uses different sets of excitations to afford multiple radiation patterns, each affording one focused beam in different directions. In comparison to the former one, the latter can achieve higher gain for the same antenna array since there is only one main lobe in the radiation pattern.

Digital beamforming, such as multiple-input-multiple-output (MIMO) signal processing, is a powerful and attractive approach to achieve the latter kind of multibeams with very much flexibility [80–83]. However, digital beamforming multibeam antennas can lead to high power consumption and economic cost. An alternative low-power-consumption and cost-effective approach to generating multibeams is employing circuit-type analogue beamforming networks. Butler matrix is a well-known and effective analogue approach to generate multibeams [84–88]. Despite their excellent performance, multibeams generated by Butler matrices are always orthogonal. This feature is acceptable in some applications, such as the conventional base station where multi-sector

coverage is required. However, for the 5G and 6G systems, more flexible and dynamic beam scanning is indispensable [62].

Blass matrix and Nolen matrix, whose beams have arbitrary directions, are preferable in the 5G and 6G wireless communications. The Blass matrix and Nolen matrix are comprised of a number of nodes, each containing a directional coupler and a phase shifter [89, 90]. Blass matrix is a rectangular matrix that consists of $M \times N$ nodes, where M is the number of beams and N is the number of antenna elements, connected with matching loads at the end of each row and column. Therefore, Blass matrices allow for generating an arbitrary number of beams, but they are usually lossy. On the other hand, Nolen matrix can save half of the nodes compared to Blass matrix since the nodes along the diagonal are directly connected to rows above [91–93]. Nevertheless, the maximum number of beams M generated by Nolen matrix is no larger than the element number N.

In [94], the authors developed a systematic method of designing analogue mutlibeam antennas by employing the generalized joined coupler (GJC) matrices including Blass matrices, Nolen matrices, and their variants. It has shown that multibeams can be obtained by optimizing the coupler values in each row of the GJC matrix, and scanning can be achieved by simply adjusting the phase shifter values. As a first-order approximation, a GJC matrix can be regarded as multiple connected series-fed linear phased arrays, as shown in Fig. 2.8. Therefore, individual and independent beam scanning can be achieved by just tuning the phase shifters. Most recently, in [95], the authors presented a more robust optimization method for the GJC matrix design, which is capable of obtaining multibeam patterns with lower SLL, as well as nulls at specific directions for anti-interference.

An intrinsic issue of the GJC matrix is that when the multibeams are close to each other or overlap, the beams generated by lower rows will significantly distort and even split into difference-pattern-like beams. That is because when two or more rows have

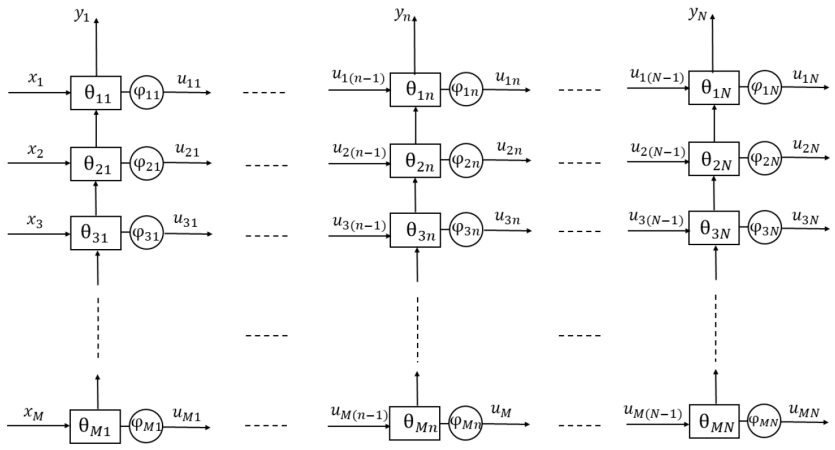

Figure 2.8: Part of a general GJC matrix [94].

their beams pointing to identical directions, the phases of some output ports would be anti-phase with respect to the rest ports. Although this issue can be avoided by simply dividing the whole scanning region as multiple sectors to avoid beam overlapping, like the authors did in [94, 95], it is unacceptable in many applications like the emerging joint communications and sensing (JCAS) systems whose beams for sensing are required to scan to arbitrary directions including angles close to or overlapping the communication beams [96–98]. This issue should be addressed carefully to make the GJC matrix more attractive in future wireless communications.

2.2.6 Linearly Polarized Element Rotation Technique

Polarization is an inherent attribute of electromagnetic waves, describing the trajectory followed by the electric field vector as observed in space along the direction of wave propagation [2]. Different polarization types include linear polarization (LP), circular polarization (CP), and elliptical polarization, each characterized by specific field vector trajectories. LP occurs when the trajectory forms a straight line, CP when it forms a circle, and elliptical polarization when it forms an ellipse. Strictly speaking, polarization must be taken into account in the array synthesis. But in most array synthesis, cross-

polarization (XP) components are not considered because they are actually negligible. However, for some arrays such as conformal arrays, owing that the orientation and radiation direction of each element are different, there is a difference in the polarization direction of the electromagnetic wave each element transmitted or received. In this situation, polarization must be taken into consideration in the array synthesis.

Actually, the polarization of an antenna can be considered as an optimization variable that can be used in the array pattern synthesis. And indeed, several researchers have considered polarization as a degree of freedom in the array synthesis [20–24, 99–101]. In the following, these polarization rotation techniques are briefly reviewed.

In [24], a method optimizing the rotation of every dipole in the array to obtain low SLL for the CoP pattern whilst maintaining the XP pattern gain under a desired level was proposed. The authors declared that except for controlling the SLL using the appropriate element weighting, an alternative way to modify the element excitation to obtain low SLL was to rotate the antenna elements individually. The element rotation changes the CoP and XP element pattern at a fixed cut of the antenna pattern. To illustrate this, the authors presented a figure, which is shown in Fig. 2.9. It is clearly shown in the figure that the θ gain pattern gets smaller and smaller with the increase of the rotation angle. The element pattern becomes less isotropic as the rotation angle increases. The gain change caused by the element rotation should be enough to generate a low SLL taper in a fixed cut of the antenna pattern. Numerical results provided in [24] verified this idea.

In [21], Echeveste et al. developed a method for synthesizing arrays of coupled antennas using the element rotation technique. The antenna array was analyzed using a hybrid method on the basis of 3D finite element method, modal analysis, and generalized scattering matrix. The array patterns were optimized by utilizing the gradient method, according to a cost function, with successive element rotations. Several low SLL patterns were synthesized with constrained XPL to evaluate the proposed method. One of them

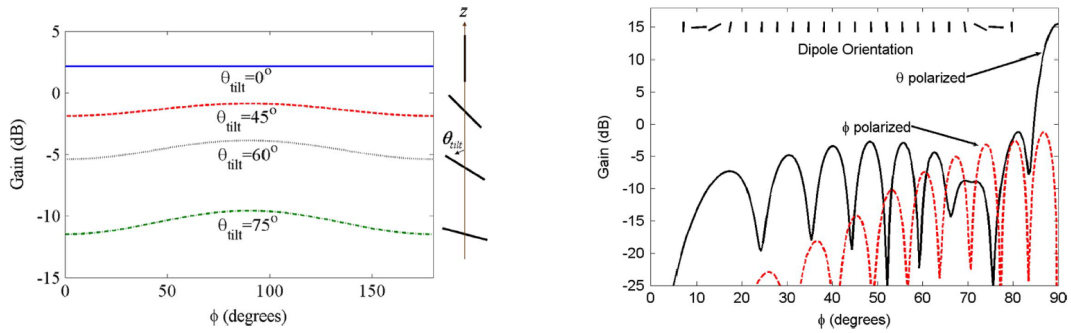

(a) (b)

Figure 2.9: Pattern of a rotated dipole and the synthesized array pattern obtained by rotating the antenna elements in [24]. (a) theta gain pattern of a dipole when it is rotated with different angles and (b) CoP and XP patterns of a linear array with rotated dipoles.

was a 10×10-element planar array. The element rotation angles were optimized, and the CoP and XP patterns with constrained low SLL and XPL were obtained. Fig. 2.10 shows the optimized results. As is seen, the element rotation technique is quite effective in focused beam pattern synthesis. Compared with [24], realistic antenna elements were considered in this method, which demonstrated its wide applicability.

In addition to the LP pattern synthesis, the rotation of the LP elements was also used in the CP pattern synthesis. In [22], a sequential rotation technique was proposed to enhance the axial ratio of the mm-wave phased-array patterns. A random sequential rotation method for synthesizing CP patterns of arrays consisting of LP antennas with SLL and axial ratio control was presented in [23]. It is shown that, although a uniform array element layout was used in the synthesis, similar properties as a randomly spaced antenna array were achieved. In such a way, wideband performance can be facilitated without introducing any grating lobes. Furthermore, owing that no amplitude weighting was used, the gain of the array pattern was maximized. A 4×4 planar array was fabricated and measured in [23]. The pictures and patterns of the fabricated array are shown in Fig. 2.11. It can be observed that favorable pattern performance in terms of the XPL, SLL, and axial ratio was obtained.

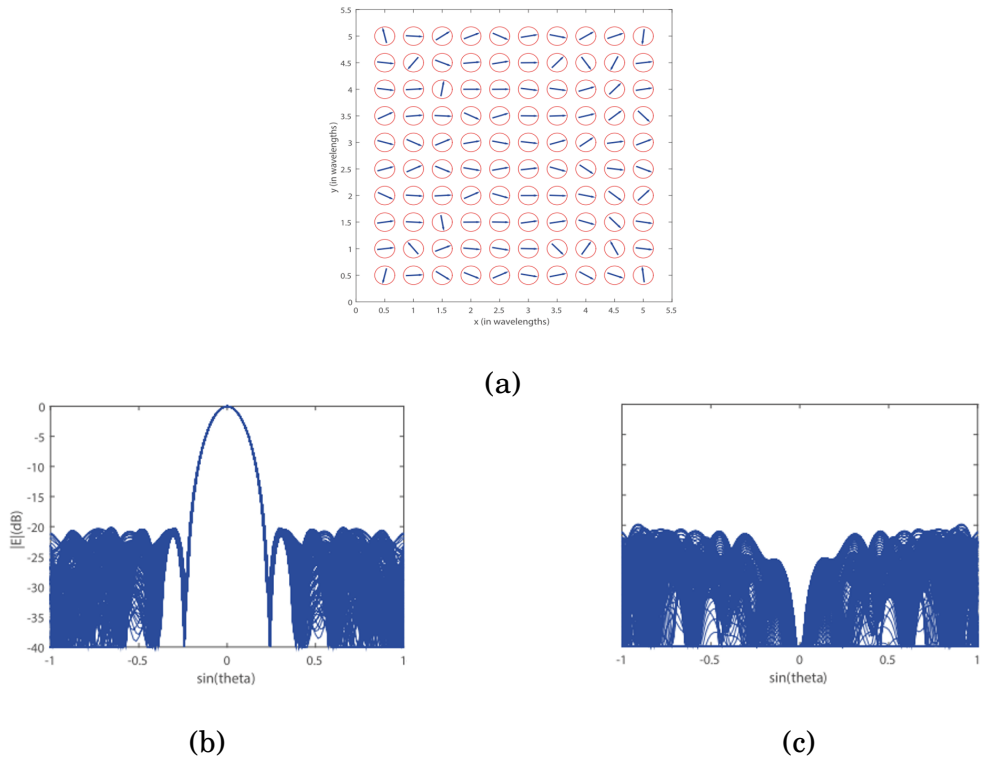

(a)

(b) (c)

Figure 2.10: The obtained rotation status of the 10×10-element array and the synthesized array patterns in [21]. (a) the optimized rotation status of the array; (b) and (c) the CoP and XP patterns, respectively.

In [99], a mapping-based optimization method was developed for synthesizing array patterns using the element rotation technique. The orientation of every element in the array was optimized to obtain low SLL and XPL meanwhile maintain the main lobe peak gain. In that paper, the variable definition domain problem was converted to a fixed definition domain problem using coordinate transformation. Then the method of moments was integrated with the optimization, which made it convenient to obtain the array pattern properties and their sensitivities concerning the design variables. Therefore, the optimization can be efficiently solved by utilizing the gradient-based optimization. Moreover, the mutual coupling was also considered.

These existing LP element rotation methods only deal with focused beam patterns with low SLL, low XPL, and large axial ratio bandwidth. Shaped-beam as well as sum-and-difference patterns synthesis employing the element rotation technique is not found

(a) (b)

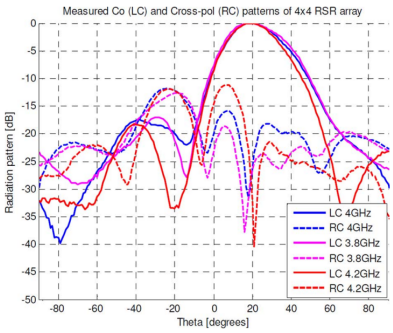

(c)

Figure 2.11: The 4×4-element array with random sequential rotation method and the CoP as well as XP patterns obtained in [23]. (a) shows the 4×4-element array obtained with random sequential rotation method, (b) and (c) show its CoP and XP patterns, respectively.

in the literature. Hence, in this dissertation, sum-and-difference patterns synthesis for linear dipole arrays employing the element rotation is first studied. Then, shaped power patterns synthesis for linear, planar, and conformal arrays using the element rotation technique considering mutual coupling are studied.

CHAPTER 3

SUM-AND-DIFFERENCE PATTERNS SYNTHESIS EMPLOYING THE ELEMENT ROTATION TECHNIQUE

3.1 Introduction

In Chapter 2, state-of-the-art works related to the sum-and-difference patterns synthesis have been reviewed. It was shown that sum-and-difference patterns synthesis employing excitation amplitude and phase modulation would lead to excellent results, yet results in complicated feeding networks and low aperture efficiency. Although phase-only methods can avoid the use of nonuniform excitation amplitudes, the pattern performances will inevitably deteriorate compared to amplitude modulation methods. In this chapter, a novel joint rotation and phase position optimization method is presented to synthesize sum-and-difference patterns. The synthesized arrays have sparsely rotated elements with uniform amplitudes, thereby leading to reductions of both the element number and unequal power dividers.

In this chapter, the following challenges are addressed: a) first, based on the two-

section beamforming network (BFN) model, common element rotations and positions are optimized for synthesizing sum-and-difference patterns; b) second, common element rotations and positions should be found to simultaneously meet multiple pattern requirements including low sidelobe levels (SLL) and cross-polarization levels (XPL) for the sum pattern, and low SLL, low XPL and large slope for the difference pattern. Several sum-and-difference patterns synthesis examples by using the developed method are presented. It is shown that favorable sum-and-difference patterns with reduced SLLs and XPLs, as well as steep slopes are obtained with uniform excitation amplitudes. Comparisons with other synthesis methods are provided to show the advantages of the proposed method.

This chapter is organized as follows. Formulation and algorithm are discussed in Section 3.2. Section 3.3 presents some numerical results. A summary is drawn in Section 3.4.

3.2 Formulations and Optimization Algorithm

3.2.1 Nouniformly Spaced Dipole-Rotated Linear Array with Sum-and-Difference Patterns

Assume there is a linear array with $2N$ nonuniformly-spaced elements located along x-axis. For convenience, the number of elements is assumed to be even. However, it should be noted that the following analysis is also applicable with slight modifications when the number of elements is odd. The sum-and-difference array is usually divided as two halves. To obtain a sum pattern, the two halves of the array can be fed with identical phases, resulting in an in-phase superposition of the elements. Conversely, to produce a difference pattern, the two halves of the array are fed with a phase difference of π. Fig. 3.1 shows a nonuniformly spaced linear array radiating sum-and-difference patterns

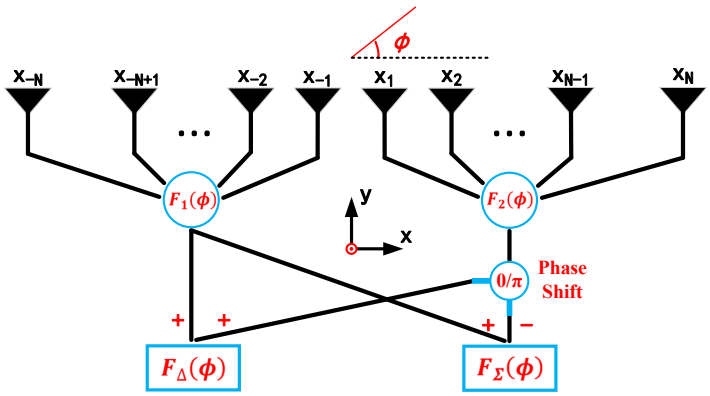

Figure 3.1: A nonuniformly spaced linear array radiating sum-and-difference patterns.

based on a typical two-section BFN.

In general, excitation amplitudes are optimized for synthesizing low-SLL sum-and-difference patterns. Thus, other than the π phase shifter, unequal power dividers are also needed. Here, instead of excitation amplitude, the element rotations and locations are optimized to synthesize sum-and-difference patterns. Such a method is not only capable of simplifying the BFN, but also improving the aperture efficiency and reducing the system cost. Let $\xi_n \in [-\pi, \pi]$ $(n = -N, -N+1, ..., -1, 1, ..., N)$ denote the arbitrary rotation angle of the n^{th} element as shown in Fig. 3.1. In the principal observation plane (xoy-plane), the vectorial sum-and-difference patterns is given as:

$$\begin{cases} \vec{F}_{\Sigma,\theta}(\phi) = \vec{F}_{1,\theta}(\phi) + \vec{F}_{2,\theta}(\phi) \\ \vec{F}_{\Sigma,\phi}(\phi) = \vec{F}_{1,\phi}(\phi) + \vec{F}_{2,\phi}(\phi) \end{cases} \tag{3.1}$$

$$\begin{cases} \vec{F}_{\Delta,\theta}(\phi) = \vec{F}_{1,\theta}(\phi) - \vec{F}_{2,\theta}(\phi) \\ \vec{F}_{\Delta,\phi}(\phi) = \vec{F}_{1,\phi}(\phi) - \vec{F}_{2,\phi}(\phi) \end{cases} \tag{3.2}$$

where

$$\begin{cases} \vec{F}_{1,\theta}(\phi) = \sum_{n=-N}^{-1} E_{n,\theta}(\phi;\xi_n) e^{j\beta r_n \cos\phi} \hat{\theta} \\ \vec{F}_{2,\theta}(\phi) = \sum_{n=1}^{N} E_{n,\theta}(\phi;\xi_n) e^{j\beta r_n \cos\phi} \hat{\theta} \end{cases} \tag{3.3}$$

$$\begin{cases} \vec{F}_{1,\phi}(\phi) = \sum_{n=-N}^{-1} E_{n,\phi}(\phi;\xi_n) e^{j\beta r_n \cos\phi} \hat{\phi} \\ \vec{F}_{2,\phi}(\phi) = \sum_{n=1}^{N} E_{n,\phi}(\phi;\xi_n) e^{j\beta r_n \cos\phi} \hat{\phi}. \end{cases} \tag{3.4}$$

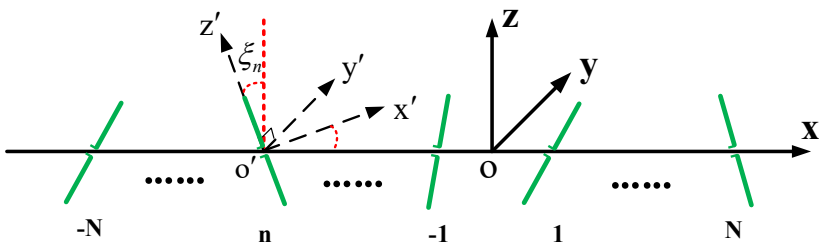

Figure 3.2: A linear array of rotated dipoles.

In the above, $\phi \in [0,\pi]$ is the azimuth angle, $j=\sqrt{-1}$, $\beta = 2\pi/\lambda$. $\vec{E}_n(\phi;\xi_n) = E_{n,\theta}(\phi;\xi_n)\hat{\theta} + E_{n,\phi}(\phi;\xi_n)\hat{\phi}$ and $r_n = x_n$ are the n^{th} rotated element pattern and position. $\vec{F}_{\Sigma,\theta}(\phi)$ and $\vec{F}_{\Sigma,\phi}(\phi)$ are the two polarization components of of the sum pattern, whilst $\vec{F}_{\Delta,\theta}(\phi)$ and $\vec{F}_{\Delta,\phi}(\phi)$ are the two polarization components of the difference pattern.

In this chapter, the effectiveness of synthesizing sum-and-difference patterns employing joint rotation and position optimization is verified with dipole arrays. Suppose the dipoles are placed in parallel (perpendicular to x-axis) along x-axis in xoz plane initially. Then, assume every dipole is rotated with an angle ξ_n with respect to their centre in xoz plane, as can be seen in Fig. 3.2. To facilitate the pattern derivation, a local coordinate $x'y'z'$ is built with z'-axis aligning with the rotated dipole and y'-axis being parallel to y-axis. In $x'y'z'$, it is easy to know the two components of radiation patterns of the rotated dipole. Then its θ- and ϕ-polarized patterns in xyz can be obtained by using coordinate transform. Finally, in the principal xoy-plane ($\theta = 90°$), its θ- and ϕ-polarized patterns can be obtained as given below [20]:

$$E_{n,\theta}(\phi;\xi_n) = \frac{\cos\xi_n \cos(\frac{\pi}{2}\sin\xi_n\cos\phi)}{1-\sin^2\xi_n\cos^2\phi} \tag{3.5}$$

$$E_{n,\phi}(\phi;\xi_n) = \frac{\sin\xi_n \sin\phi\cos(\frac{\pi}{2}\sin\xi_n\cos\phi)}{\sin^2\xi_n\cos^2\phi-1}. \tag{3.6}$$

By substituting (3.5) and (3.6) into (3.1)-(3.4), one can obtain the sum-and-difference pattern expression.

3.2.2 Cost Function for Sum-and-Difference Patterns Synthesis

The problem concerned is finding the optimal combination of element rotation angles ξ_n and positions x_n, such that the sum-and-difference patterns exhibit minimal SLLs and XPLs, while ensuring that the difference pattern has the steepest slope achievable. To result in a symmetrical BFN, the element distribution x_n are assumed to be symmetrical with respect to the array center. Therefore, only N element positions need to be optimized. On the other hand, all the element rotation angles are chosen as optimization variables to achieve better pattern performance. Therefore, the optimization problem involves optimizing a total of N positions and $2N$ rotation angles. To achieve this, a cost function is constructed that incorporates five different terms aimed at penalizing SLLs, XPLs, and the slope of the difference pattern.

$$\begin{aligned} f_c = \frac{W_1}{B}\sum_{b=1}^{B}\frac{1}{4}(X_b+|X_b|)^2 + \frac{W2}{C}\sum_{c=1}^{C}\frac{1}{4}(Y_c+|Y_c|)^2 + \frac{W_3}{D}\sum_{d=1}^{D}\frac{1}{4}(Z_{\Sigma,d}+|Z_{\Sigma,d}|)^2 \\ + \frac{W_4}{D}\sum_{d=1}^{D}\frac{1}{4}(Z_{\Delta,d}+|Z_{\Delta,d}|)^2 + \frac{W_5}{4}(|S|-S)^2 \end{aligned} \tag{3.7}$$

where

$$\begin{cases} X_b = |F_{\Sigma,\theta}(\phi_b)|^2 - \Gamma_{SLL1} \\ Y_c = |F_{\Delta,\theta}(\phi_c)|^2 - \Gamma_{SLL2} \\ Z_{\Sigma,d} = |F_{\Sigma,\phi}(\phi_d)|^2 - \Gamma_{XPL1} \\ Z_{\Delta,d} = |F_{\Delta,\phi}(\phi_d)|^2 - \Gamma_{XPL2} \\ S = |\frac{\partial F_{\Delta,\theta}(\phi)}{\partial \phi}|_{\phi=\phi_0}|^2 - \Gamma_{slope}. \end{cases} \tag{3.8}$$

In the above, W_1, W_2, W_3, W_4 and W_5 are weighting factors. Γ_{SLL1} and Γ_{SLL2} are the target SLLs for $F_{\Sigma,\theta}(\phi)$ and $F_{\Delta,\theta}(\phi)$, respectively, whereas Γ_{XPL1} and Γ_{XPL2} are the target XPLs for $F_{\Sigma,\phi}(\phi)$ and $F_{\Delta,\phi}(\phi)$, respectively. Without loss of generality, the θ-polarized pattern is considered as the co-polarized (CoP) pattern. Γ_{slope} denotes the target difference pattern slope. The sampling angles in the SLL regions of $F_{\Sigma,\theta}(\phi)$ and $F_{\Delta,\theta}(\phi)$ are denoted by $\phi_b (b = 1,2,...,B)$ and $\phi_c (c = 1,2,...,C)$, respectively. Additionally, ϕ_d $(d = 1,2,...,D)$ represents the sampling angle in the range of $\phi \in [0,\pi]$. The target

direction ϕ_0 is chosen as $\phi_0 = \pi/2$ throughout this chapter and, hence, the difference pattern slope can be obtained as:

$$\frac{\partial F_{\Delta,\theta}(\phi)}{\partial \phi}|_{\phi=\pi/2} = \sum_{n=-N}^{N} sgn(n) j\beta x_n \cos\xi_n \tag{3.9}$$

where $sgn(n)$ is the sign function of n ($n = -N, -N+1, ..., -1, 1, ..., N$). It should be noted that if nulls are required in some applications, more penalization terms can be added to the cost function of (3.7).

The cost function (3.7) is defined as the summation of five terms, each targeting a specific aspect. In a sequential manner, these terms aim to penalize SLLs of the sum-and-difference patterns, XPLs of the sum-and-difference patterns, and the slope of the difference pattern, respectively. Let us take the first term, $\frac{W_1}{B}\sum_{b=1}^{B}\frac{1}{4}(X_b+|X_b|)^2$, as an example for explanation. In this term, $X_b = |F_{\Sigma,\theta}(\phi_b)|^2 - \Gamma_{SLL1}$ represents the difference between the actual SLL of the sum pattern and the target value Γ_{SLL1} at the observation angle ϕ_b. If the SLL $|F_{\Sigma,\theta}(\phi_b)|^2$ at angle ϕ_b is greater than Γ_{SLL1}, indicating that it exceeds the target value and requires penalization, X_b will be a positive value. Otherwise, if X_b is non-positive, it means that the SLL is within the acceptable range and no penalization is needed. When X_b is positive, we have $X_b + |X_b| = 2X_b$. In this case, $\frac{1}{4}(X_b+|X_b|)^2 = X_b^2$. On the other hand, when X_b is non-positive, $X_b + |X_b| = 0$, resulting in $\frac{1}{4}(X_b+|X_b|)^2 = 0$. Therefore, the summation $\frac{W_1}{B}\sum_{b=1}^{B}\frac{1}{4}(X_b+|X_b|)^2$ accounts only for SLLs at the sampling angles where they are worse than the target value.

Similar explanation applies to the remaining four terms in (3.7). Therefore, only the SLLs, XPLs, and slope that do not meet the requirements will contribute to the cost. As a result, when utilizing a stochastic algorithm to optimize rotation angles and positions guided by the cost function (3.7), achieving a minimized value of (3.7) as 0 ensures the satisfaction of all requirements.

3.2.3 Element Rotation and Position Optimization with the Particle Swarm Optimization

Minimizing the cost function (3.7) to find optimal ξ_n and x_n ($x_{-n} = -x_n$ for $n = -N, -N+1, ..., -1, 1, ..., N$) is a highly non-linear problem. In general, a global stochastic algorithm would be adequate for the optimization. The particle swarm optimization (PSO) method is adopted here. The PSO is a population-based algorithm that is developed by mimicking the behavior of social animals like bird flocks. It is computationally inexpensive in terms of both memory requirements and speed [102]. In PSO, each particle keeps its own track which is related to the best position called $pbest$ it has achieved in the problem space. Another position is the global best location called $gbest$. The PSO finds the global best solution by changing the speed of every particle to its $pbest$ and $gbest$ with an acceleration factor weighted by a random term in every iterative generation. The PSO has found many different applications in array synthesis problems [8, 103]. **Algorithm** 1 lists the detailed optimization procedure based on the PSO.

3.3 Synthesis Results

In this section, three examples are provided to demonstrate the effectiveness of the developed sum-and-difference patterns synthesis method based on joint rotation and position optimization. Comparisons with other methods are also provided. All the examples were conducted on a Dell Workstation with an Intel Xeon E5-2697 CPU at 2.30 GHz.

3.3.1 Sum-and-Difference Patterns Synthesis for a 32-Element Linear Array

A 32-element linear dipole array is employed to synthesize sum-and-difference patterns with reduced SLLs as the first example. The element positions are assumed to be

Algorithm 1 The developed sum-and-difference patterns synthesis procedure based on element rotation.

1: Input the parameters including Γ_{SLL1}, Γ_{SLL2}, Γ_{XPL1}, Γ_{XPL2}, and Γ_{slope}. Set the maximum iteration I_m, population size N_p, problem dimension D_p as well as weighting factors W_1, W_2, W_3, W_4, and W_5.
2: Randomly generate N_p particles composed of $\xi_n(n = -N, -N+1, ..., -1, 1, ..., N)$ and $x_n(n = 1, 2, ..., N)$ with random velocities and positions in the given D_p dimensional solution space.
3: Evaluate the cost function value of each particle using (3.7).
4: Compare the cost function value of the current particle with that of the $pbest$. If the current value is smaller than that of $pbest$, let $pbest$ equal the current location, and update the cost function value with the current cost function value.
5: Compare the current cost function value with that of $gbest$, which is the best solution all the particles achieved so far. If the current value is smaller than that of $gbest$, replace the location and cost function value of $gbest$ with those of the current particle.
6: Update the velocity and position of the current particle.
7: Loop to step 3 until the maximum iteration I_m is reached or the best rotations ξ_n and positions x_n remain unchanged for multiple iterations.

symmetric, and all the element intervals are restricted in $[0.5\lambda, \lambda]$. The available element rotation angle is set as $\xi_n \in [-\pi, \pi]$. In the PSO-based optimization, the weighting coefficients of the cost function are set as $W_1 = W_2 = W_3 = W_4 = 1$, and $W_5 = 5$, respectively. The target SLLs and XPLs are set as $\Gamma_{SLL1} = \Gamma_{SLL2} = \Gamma_{XPL1} = \Gamma_{XPL2} = -17$ dB. The target difference pattern slope is chosen as $\Gamma_{slope} = 45$ dB. The number of optimization variables is $D_p = 48$. The population size of the PSO is set as $N_p = 96$, whilst the iteration number is set as $I_m = 2000$.

Fig. 3.3 shows the synthesized sum-and-difference patterns. It is observed that the achieved SLL and XPL for the sum pattern are -17.00 and -19.71 dB, respectively, whereas the difference pattern has a SLL and XPL of -17.01 dB and -17.04 dB, respectively. All of them meet the specified bound of -17 dB. The difference pattern has a slope of 59.21 dB. Table 3.1 lists the obtained element rotations as well as positions. The obtained minimum, maximum, and average element intervals are 0.50λ, 1.00λ, and 0.77λ, respectively. It means that the synthesized array by the developed method saved around 34.69% elements comparing to a half-wavelength-spaced array that has an

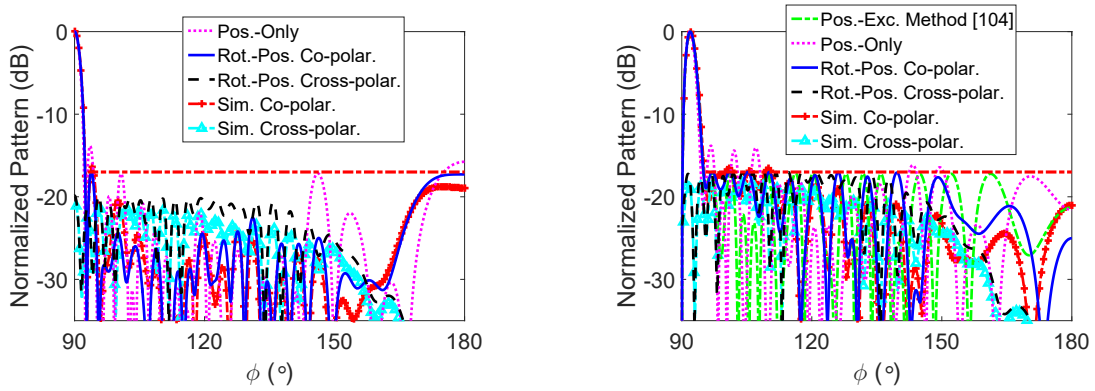

(a) The sum pattern (b) The difference pattern

Figure 3.3: The synthesized sum-and-difference patterns and the corresponding full-wave simulated ones, patterns synthesized by a position-only method, and the difference pattern obtained with the position and excitation optimization in [104] for a 32-dipole linear array.

identical array aperture. The time cost of the PSO-based optimization for this example is about 4.12 minutes.

For comparison purpose, the sum-and-difference patterns are also synthesized by employing position-only optimization using the same PSO. In this case, only element positions are optimized. The number of variables is set as $D_p = 16$, and the population size is $N_p = 2D_p = 32$. The inter-element spacing restriction and other parameters are used the same as above. The synthesized patterns are plotted in Fig. 3.3(a) and (b). It is observed that the SLLs are increased to -13.80 dB and -13.84 dB, respectively, due to the lack of the element rotations as the additional degrees of freedom.

In addition, the hybrid approach of convex programming and simulated annealing (SA) that was developed in [104] is also adopted here to produce the same difference pattern for further comparison. The constraint on the element intervals is set as $[0.5\lambda, \lambda]$, which is the same as that of the developed method, and the parameters for the SA, including the initial temperature and the scaling factor for the temperatures, are used the same as those used in [104]. The obtained difference pattern by this hybrid method is shown in Fig. 3.3(b). It can be seen that the maximum SLL is almost the same as that

of the developed method. However, in this hybrid method, amplitude weighting along with position optimization is used, and the amplitude dynamic range ratio required for generating this pattern is 4.49. This leads to a relatively complicated BFN with multiple unequal power dividers. In contrast, the array synthesized using the developed method does not need amplitude weighting, as it achieves the desired pattern characteristics through appropriate element rotations.

Besides, with the element rotations and positions obtained by the developed method, the array is modeled by using the high-frequency simulation software (HFSS) [105]. A 1 mm diameter dipole operating at a frequency of $f = 3$ GHz with an overall length of 48 mm is used as the element. Figure 3.3 depicts the full-wave simulated patterns, which demonstrate excellent agreement with the synthesized patterns. The full-wave simulated SLLs of the two patterns increase by 0.64 dB and 0.50 dB, respectively, meanwhile the XPLs remain below the target bound. The high level of agreement between the synthesized and simulated patterns can be attributed to the weak mutual coupling between elements, which is a result of the relatively large spacing between them.

3.3.2 Sum-and-Difference Patterns Synthesis for a 56-Element Linear Array

As another example, sum-and-difference patterns in Fig. 6 and Fig. 7 of [33] obtained with excitation amplitude and position optimization using a linear programming method are synthesized. The obtained SLLs in [33] were -20 dB and -16.5 dB for the sum-and-difference patterns, respectively. Here, for comparison, sum-and-difference patterns under the same SLL and XPL constraints are synthesized with a 56-element linear dipole array through optimization of the element rotations and positions. The element spacing is restricted in $[0.5\lambda, 1.28\lambda]$ (smaller than $[0.43\lambda,\ 1.28\lambda]$ in [33]). A minimum spacing of 0.5λ is utilized to avoid the intersection between elements. In the PSO-based

optimization, the target SLLs and XPLs are chosen to be identical as those in [33]. The target difference pattern slope is still Γ_{slope} = 45 dB. The number of variables to be optimized is $D = 84$. The population size and the maximum iterations are set as $N_p = 168$ and $I_m = 2000$, respectively. Other parameters are chosen to be identical as those in the first example.

The PSO-based synthesis procedure takes about 41.98 minutes to find the solution in this example. Fig. 3.4(a) and (b) show the results obtained by the developed method as well as those obtained in [33]. It is shown that the developed method yields a sum pattern with SLL and XPL values of −20.01 dB and −20.03 dB, respectively. The difference pattern, on the other hand, has SLL and XPL values of −16.50 dB and −16.51 dB, respectively. The slope of the difference pattern is 68.68 dB. The pattern performance is comparable to that obtained in [33]. But it should be mentioned again that the synthesized array by the developed method does not utilize nonuniform amplitude weighting, so no unequal power dividers are required. The corresponding element rotations and positions are listed in the middle column of Table 3.1. For this particular example, the minimum, maximum, and average element spacings of the synthesized array are 0.5λ, 1.07λ, and 0.88λ, respectively. Fig. 3.4 also shows the full-wave simulated patterns. One can see that the simulated SLLs are −17.82 dB and −15.35 dB, respectively. They are 2.19 dB and 1.15 dB worse than the synthesized values. The simulated XPLs remain below the target levels.

To demonstrate the advantage of optimizing both the element positions and rotations, the rotation-only optimization method is utilized here to synthesize the same sum-and-difference patterns. A 97-element dipole array with uniform spacing of $\lambda/2$ is adopted since it occupies almost the same aperture as that of the sparse array obtained by the developed method, and thus sum-and-difference patterns with similar beamwidths and slope can be obtained. In the PSO-based rotation-only optimization, $D_p = 97$ and

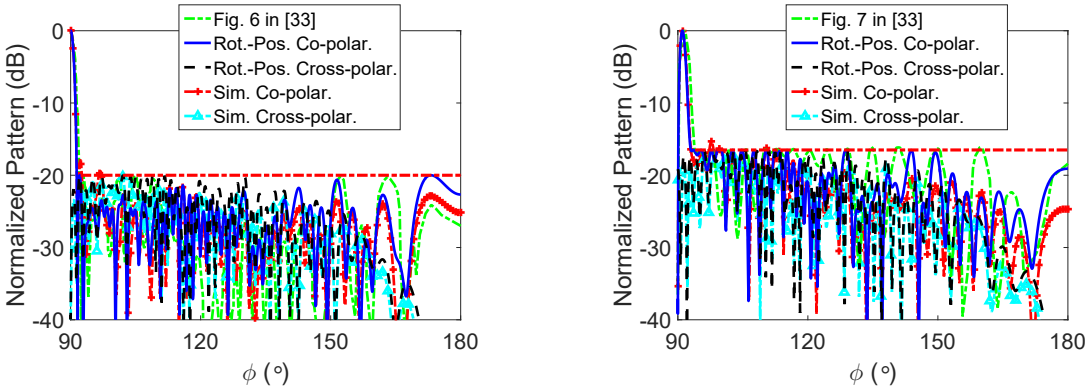

(a) The sum pattern (b) The difference pattern

Figure 3.4: The synthesized sum-and-difference patterns and the corresponding full-wave simulated results, as well as patterns in [33] for a linear array of 56 elements.

$N_p = 2D_p = 194$. The rotation angle range and other parameters are used the same as those of the developed method. Fig. 3.5 shows the obtained sum-and-difference patterns. The SLL and XPL values of the sum pattern are -19.71 dB and -19.85 dB, respectively, while the difference pattern has SLL and XPL values of -16.42 dB and -16.43 dB, respectively. These values are slightly higher than the corresponding ones obtained by the developed method. Besides, the developed method requires much fewer elements than the rotation-only optimization method, and the element saving is up to 42.27%.

3.3.3 Sum-and-Difference Patterns Synthesis with Nulls for Anti-Interference

In electromagnetic environments where jamming is present from specific directions, it becomes necessary to introduce nulls to mitigate the interference. As an example, a same 56-element dipole array is used to synthesize both sum-and-difference patterns with an additional requirement of a -30 dB null in the region of $\phi \in [40°, 45°] \cup [135°, 140°]$. To meet this requirement, the cost function (3.7) needs to be modified slightly. While the first four terms in the cost function are used to generate a -20 dB SLL and XPL for the

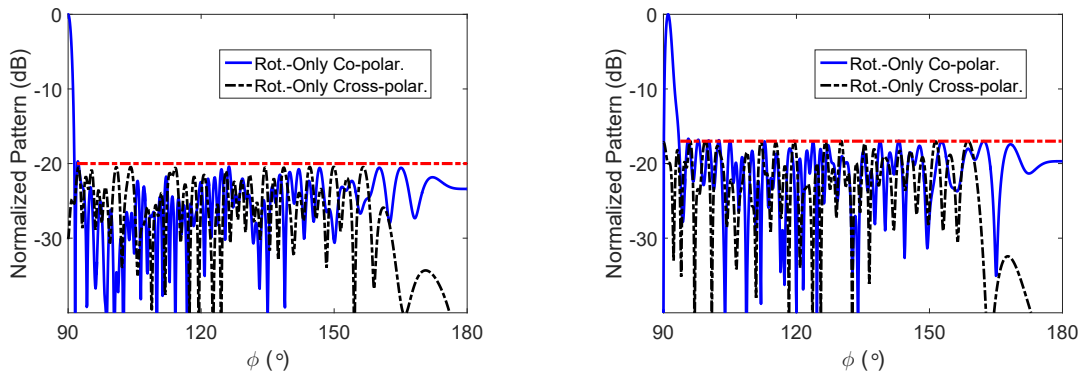

(a) The sum pattern (b) The difference pattern

Figure 3.5: The sum-and-difference patterns obtained using a rotation-only method with a 97-element $\lambda/2$-spaced linear dipole array.

sum pattern, and a -16.5 dB SLL and XPL for the difference pattern, an additional four terms are added to penalize the -30 dB nulls in the specified regions for all patterns. All other parameter settings for the PSO-based synthesis procedure are used the same as those in the second example.

The PSO-based pattern synthesis takes about 42.35 minutes in this example. Fig. 3.6(a) and (b) show the obtained patterns with enlarged views of peaks and -30 dB SLL/XPL regions. The results demonstrate that the obtained patterns meet the requirements, even for complex null specifications, except for a slightly higher first sidelobe in the sum pattern (approximately 0.55 dB above the target level). The difference pattern slope in the target direction is 68.84 dB. It is noted that the nulls for both patterns are restricted below -30 dB in $\phi \in [40^\circ, 45^\circ] \cup [135^\circ, 140^\circ]$. These results further demonstrate the outstanding capability of the developed method.

Table 3.1 lists the obtained element rotations and positions in the right column. The minimum, maximum, and average element spacings achieved are 0.50λ, 1.18λ, and 0.88λ, respectively. Around 42.27% elements have been saved in this example comparing to a half-wavelength-spaced array with an identical array aperture. Fig. 3.6 also shows the full-wave simulated patterns of the dipole-rotated array. The full-wave simulated

Table 3.1: THE ELEMENT ROTATIONS AND POSITIONS ($x_{-n} = -x_n$) OBTAINED BY THE DEVELOPED METHOD FOR THE THREE EXAMPLES.

	Example 1		Example 2		Example 3	
n	Rot. (°)	Pos. (λ)	Rot. (°)	Pos. (λ)	Rot. (°)	Pos. (λ)
1	−46.74	−12.19	24.72	−24.10	−58.70	−24.08
2	85.26	−11.19	−83.14	−23.23	91.32	−22.90
3	−49.09	−10.43	152.22	−22.17	−29.12	−21.91
4	56.22	−9.46	10.77	−21.10	71.44	−20.93
5	14.78	−8.56	−66.37	−20.03	94.69	−19.87
6	21.84	−7.72	−23.75	−19.04	60.82	−19.02
7	14.33	−6.93	71.53	−18.09	48.28	−18.16
8	1.10	−6.17	−61.46	−17.33	23.68	−17.18
9	−3.60	−5.51	−35.25	−16.38	59.38	−16.29
10	−2.28	−4.78	−42.79	−15.32	−33.20	−15.32
11	−12.74	−4.09	20.44	−14.44	−10.64	−14.41
12	−6.65	−3.36	2.38	−13.53	−5.25	−13.50
13	−2.88	−2.55	−17.80	−12.68	−4.94	−12.58
14	−0.42	−1.67	−3.38	−11.71	4.90	−11.74
15	−0.72	−0.88	6.52	−10.85	4.07	−10.84
16	1.98	−0.25	15.16	−9.96	20.32	−10.06
17	−0.97	0.25	−4.56	−9.18	−4.38	−9.28
18	3.67	0.88	−3.21	−8.46	4.48	−8.45
19	6.31	1.67	−10.39	−7.60	3.40	−7.68
20	4.52	2.55	−9.93	−6.80	−7.84	−6.80
21	3.48	3.36	0.60	−5.89	1.86	−5.93
22	5.43	4.09	5.71	−5.05	−10.03	−5.05
23	−7.19	4.78	3.80	−3.99	9.82	−4.27
24	2.53	5.51	−5.30	−3.15	−15.60	−3.39
25	0.31	6.17	35.09	−2.21	5.90	−2.36
26	10.73	6.93	−4.83	−1.40	−8.25	−1.54
27	12.87	7.72	−0.13	−0.75	0.24	−0.80
28	36.80	8.56	2.80	−0.25	−0.86	−0.25
29	−21.19	9.46	−1.41	0.25	−0.61	0.25
30	−53.67	10.43	3.54	0.75	−1.17	0.80
31	75.97	11.19	4.53	1.40	−7.78	1.54
32	67.89	12.19	−2.61	2.21	6.03	2.36
33			−2.56	3.15	−1.43	3.39
34			2.01	3.99	18.74	4.27
35			−1.23	5.05	−9.34	5.05
36			−0.29	5.89	3.56	5.93
37			11.08	6.80	−12.19	6.80
38			−3.14	7.60	−0.89	7.68
39			−15.88	8.46	10.76	8.45
40			10.68	9.18	7.04	9.28
41			6.05	9.96	4.71	10.06
42			−3.86	10.85	1.86	10.84
43			−4.59	11.71	9.70	11.74
44			−16.40	12.68	−2.38	12.58
45			9.71	13.53	−1.84	13.50
46			18.59	14.44	−31.45	14.41
47			−1.01	15.32	−37.48	15.32
48			−41.83	16.38	41.17	16.29
49			−46.77	17.33	63.99	17.18
50			−55.55	18.09	−0.54	18.16
51			83.30	19.04	−29.74	19.02
52			55.06	20.03	−109.26	19.87
53			84.40	21.10	26.57	20.93
54			39.19	22.17	119.04	21.91
55			−80.79	23.23	−55.72	22.90
56			77.53	24.10	60.95	24.08

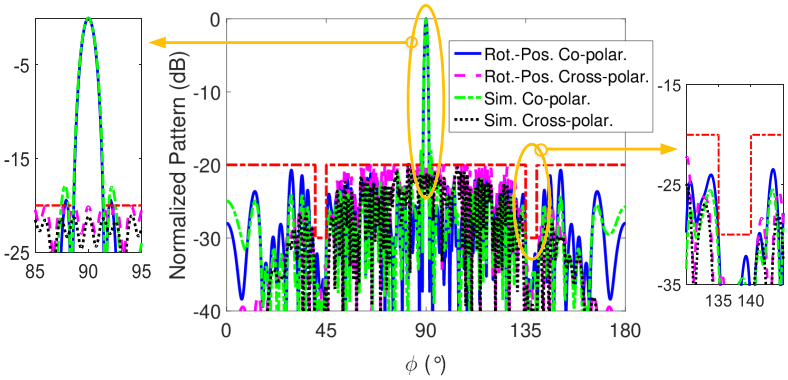

(a) The sum patterns

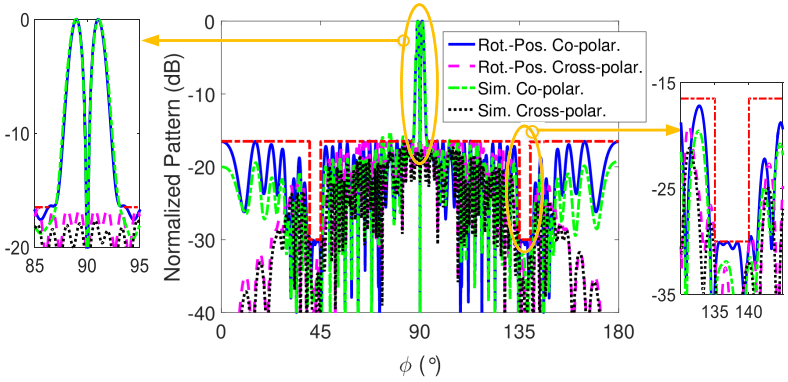

(b) The difference patterns

Figure 3.6: The synthesized and full-wave simulated sum-and-difference patterns with nulls for a linear array of 56 rotated dipoles.

SLLs are 1.57 dB and 1.28 dB higher than the synthesized values, whereas the XPLs of both patterns still keep below the target bound. The simulated patterns match the synthesized ones very well in total.

3.4 Summary

A novel method that synthesizes sum-and-difference patterns through the optimization of the element rotation angles and positions of uniform amplitude dipole arrays is presented in this chapter. Numerical examples are presented, and it is shown that the

developed method can obtain much better sum-and-difference patterns performance than the position-only optimization method. Compared with the joint optimization of element excitations and positions, the developed method can obtain comparable pattern performance but without the requirement of nonuniform amplitude weighting, thus saving many unequal power dividers for the BFN. Synthesis results also validated the ability of the developed method to synthesize sum-and-difference patterns with nulls at specific angles. In the presented examples, the element reduction achieved is around 34.69% - 42.27% compared to the uniformly distributed arrays using $\lambda/2$-spaced elements to occupy the same aperture. Hence, the overall advantages, including the BFN simplification and element reduction, make the developed method very attractive for applications where the cost, complexity, and weight of the antenna system are highly restricted.

CHAPTER 4

SHAPED-BEAM PATTERN LINEAR AND PLANAR ARRAY DESIGN BASED ON ELEMENT ROTATION

4.1 Introduction

In Chapter 3, sum and difference patterns are synthesized employing the element rotation technique. Linear dipole arrays with analytical expressions were considered. In this chapter, the element rotation technique is extended to deal with shaped pattern synthesis considering mutual coupling and arbitrary antenna elements for linear and planar arrays. To this end, the vectorial active element pattern (VAEP) is employed to consider mutual coupling. Element rotations are approximately achieved by mathematically rotating the full-wave simulated VAEPs. After that, rotation angles, as well as excitation phases of the array, are optimized by using the particle swarm optimization (PSO) to achieve desired shaped patterns. To improve the approximation accuracy, a refined strategy is adopted. Several examples are provided to show the effectiveness of this method. The synthesis results are validated through full-wave simulation. A

prototype of a 24-element linear array is fabricated and measured. Measured results turn out to agree very well with the simulated ones.

This chapter is organized as follows. Formulation and algorithm are discussed in Section 2. Section 3 presents some numerical results. In Section 4, measurement results are presented. A summary is drawn in Section 5.

4.2 Formulations and Optimization Algorithm

This section presents the derivation of the antenna-rotated array pattern model as well as the refined element rotation/phase synthesis procedure by utilizing the PSO.

4.2.1 Vectorial Pattern Expression of a General Antenna-Rotated Array

The expression of an antenna-rotated array is derived first. Consider a 3×3 planar patch array without element rotation as shown in Fig. 4.1(a). Note that the following formulation is valid for any antenna-rotated linear and planar arrays regardless of element count and placement. According to equation (2.1), the vectorial array pattern can be given by:

$$F_\theta(\theta,\phi) = \sum_{n=1}^{N} E_{n,\theta}(\theta,\phi;0)e^{j\{\beta\vec{r}_n\cdot\vec{u}(\theta,\phi)+\varphi_n\}} \tag{4.1}$$

$$F_\phi(\theta,\phi) = \sum_{n=1}^{N} E_{n,\phi}(\theta,\phi;0)e^{j\{\beta\vec{r}_n\cdot\vec{u}(\theta,\phi)+\varphi_n\}} \tag{4.2}$$

where $\beta = 2\pi/\lambda$, $j = \sqrt{-1}$, $\vec{u} = [\sin\theta\cos\phi, \sin\theta\sin\phi, \cos\theta]$. $\vec{r}_n$ and φ_n are the n^{th} element location and excitation phase, respectively. $\vec{E}_n(\theta,\phi;0) = E_{n,\theta}(\theta,\phi;0)\vec{\theta} + E_{n,\phi}(\theta,\phi;0)\vec{\phi}$ is the VAEP for the n^{th} antenna without rotation, i.e., with the state of '0' rotation angle [106]. A VAEP is a vectorial pattern of an array with one element is excited, whilst the rest elements are terminated with matching loads. In general, VAEPs can be obtained by using measurements or full-wave simulations. VAEPs usually vary for different elements.

(a) (b)

Figure 4.1: Configuration of a 3×3-element planar array with (a) no element rotation, and (b) elements rotated by different angles.

However, for the case of uniformly spaced linear or planar arrays with the elements rotated by an identical angle (for example, all with '0' rotation angle), VAEPs for different elements can be considered identical if one ignores the edge effect of the array. That is, $\vec{E}_n(\theta,\phi;0) = \vec{E}(\theta,\phi;0) = E_\theta(\theta,\phi;0)\vec{\theta} + E_\phi(\theta,\phi;0)\vec{\phi}$ for $n = 1,2,\cdots,N$. In this situation, the simulated VAEP using periodic boundaries can be utilized to approximate the real VAEPs, which simplifies the process of obtaining those VAEPs.

Now, assume that those N elements are separately rotated in the xoy plane with respect to the z'-axis in their own local coordinate systems (LCSs) $x'y'z'$ as shown in Fig. 4.1(b). With ξ_n denoting the n^{th} element rotation angle, the vectorial array patterns are expressed as:

$$F_\theta^{\text{Rot}}(\theta,\phi) = \sum_{n=1}^{N} E_{n,\theta}(\theta,\phi;\xi_n) e^{j\{\beta\vec{r}_n\cdot\vec{u}(\theta,\phi)+\varphi_n\}} \tag{4.3}$$

$$F_\phi^{\text{Rot}}(\theta,\phi) = \sum_{n=1}^{N} E_{n,\phi}(\theta,\phi;\xi_n) e^{j\{\beta\vec{r}_n\cdot\vec{u}(\theta,\phi)+\varphi_n\}} \tag{4.4}$$

where $\vec{E}_n(\theta,\phi;\xi_n) = E_{n,\theta}(\theta,\phi;\xi_n)\vec{\theta} + E_{n,\phi}(\theta,\phi;\xi_n)\vec{\phi}$ is the n^{th} VAEP with an rotation range of ξ_n. The condition $\xi_n > 0$ indicates an anticlockwise rotation. The definition of the VAEP specifies that the n^{th} VAEP is not only dependent on its own rotation angle, but also on the rotation angles of neighboring elements.

As mentioned previously, all VAEPS can be acquired using measurements or full-wave simulations. However, in the considered problem, element rotation angles and phases

are unknown variables to be optimized. Hence, their values are actually unknown. To deal with this issue, an assumption is made that the mutual coupling among the current element and other elements remains unchanged during the rotation. Thus the rotated element pattern can be approximately obtained by mathematically rotating its original VAEP from the '0' rotation state. It can be easily proved that, for the n^{th} element rotated with an angle of ξ_n with respect to z'-axis in the LCS, the phase-adjusted VAEP can be approximated as:

$$E_{n,\theta}(\theta,\phi;\xi_n) \approx E_{n,\theta}(\theta,\phi-\xi_n;0) \tag{4.5}$$

$$E_{n,\phi}(\theta,\phi;\xi_n) \approx E_{n,\phi}(\theta,\phi-\xi_n;0). \tag{4.6}$$

By substituting (4.5) and (4.6) into (4.3) and (4.4), one can obtain:

$$F_{\theta}^{\mathrm{Rot}}(\theta,\phi) \approx \sum_{n=1}^{N} E_{n,\theta}(\theta,\phi-\xi_n;0)e^{j\{\beta\vec{r}_n\cdot\vec{u}(\theta,\phi)+\varphi_n\}} \tag{4.7}$$

$$F_{\phi}^{\mathrm{Rot}}(\theta,\phi) \approx \sum_{n=1}^{N} E_{n,\phi}(\theta,\phi-\xi_n;0)e^{j\{\beta\vec{r}_n\cdot\vec{u}(\theta,\phi)+\varphi_n\}}. \tag{4.8}$$

The accuracy of the above approximation greatly depends on the rotation angles ξ_n for $n = 1,2,\cdots,N$, given determined element spacing and radiating structure. As a general rule, larger rotation angles result in lower approximation accuracy. This means that when an algorithm is used to optimize the element rotations and phases using the approximated expressions (4.7) and (4.8), the actual array pattern including mutual coupling variations may differ from the synthesized one calculated from the approximated expressions. The extent of the discrepancy depends on the allowable range of ξ_n. To reduce this discrepancy, a refining strategy can be utilized. For example, after optimizing the element rotations and phases using the approximated expressions, full-wave simulation can be used to obtain all the real rotated VAEPs for the new configurations. Then, the element rotations can be fine-tuned within a smaller range to improve the synthesized results and reduce the errors.

The refined joint optimization process for element rotations and excitation phases can be repeated multiple times until the difference between the synthesized and actual array patterns is negligible or below a predetermined tolerance level. Let $\xi_n^{(0)}$ and $\xi_n^{(k)}$ represent the rotation angle for the n^{th} element at the initial step and the k^{th} refining step ($k = 1, 2, \cdots, K$), respectively. Similarly, let $\varphi_n^{(0)}$ and $\varphi_n^{(k)}$ denote the element phases at the initial step and the k^{th} refining step, respectively. At the k^{th} refining step, the approximated array pattern can be expressed as:

$$F_\theta^{(k)}(\theta,\phi) \approx \sum_{n=1}^{N} E_{n,\theta}(\theta,\phi-\xi_n^{(k)};\sum_{l=0}^{k-1}\xi_n^{(l)})e^{j\{\beta\vec{r}_n\cdot\vec{u}(\theta,\phi)+\varphi_n^{(k)}\}} \tag{4.9}$$

$$F_\phi^{(k)}(\theta,\phi) \approx \sum_{n=1}^{N} E_{n,\phi}(\theta,\phi-\xi_n^{(k)};\sum_{l=0}^{k-1}\xi_n^{(l)})e^{j\{\beta\vec{r}_n\cdot\vec{u}(\theta,\phi)+\varphi_n^{(k)}\}}. \tag{4.10}$$

To reduce the error, the allowed range of the element rotation angle $\xi_n^{(k)}$ at the refining steps are set smaller and smaller as the increase of k. When $\xi_n^{(k)}$ is small enough, the synthesized array patterns will show good agreement with the full-wave simulated ones including mutual coupling variation.

4.2.2 Shaped Pattern Synthesis Using the Element Rotation and Excitation Phase Optimization

To facilitate the formulation, the realizable co-polarization (CoP) and cross-polarization (XP) definitions presented in [44] is adopted to calculate the CoP and XP patterns. As is seen in Fig. 4.2, the CoP is given by:

$$\vec{p}_{co} = \frac{\vec{p}_d - [\vec{p}_d\cdot\vec{u}(\theta,\phi)]\vec{u}(\theta,\phi)}{|\vec{p}_d - [\vec{p}_d\cdot\vec{u}(\theta,\phi)]\vec{u}(\theta,\phi)|}. \tag{4.11}$$

The realizable XP direction $\vec{p}_X$ is orthogonal with respect to both $\vec{p}_{co}$ and $\vec{u}(\theta,\phi)$, which is given as:

$$\vec{p}_X = \vec{p}_{co}\times\vec{u}(\theta,\phi). \tag{4.12}$$

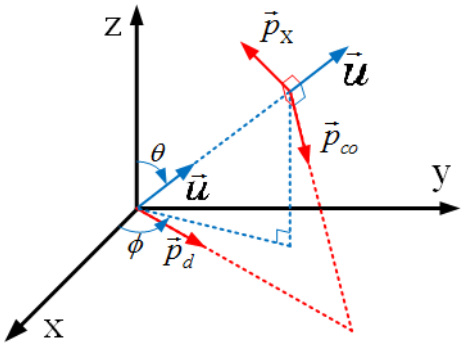

Figure 4.2: The CoP and XP defined in [44].

With (4.11) and (4.12), one then can calculate the approximated CoP and XP array patterns at the k^{th} step:

$$F_{co}^{(k)}(\theta,\phi) \approx \sum_{n=1}^{N} E_{n,co}(\theta,\phi-\xi_n^{(k)};\sum_{l=0}^{k-1}\xi_n^{(l)})e^{j\{\beta\vec{r}_n\cdot\vec{u}(\theta,\phi)+\varphi_n\}} \tag{4.13}$$

$$F_{X}^{(k)}(\theta,\phi) \approx \sum_{n=1}^{N} E_{n,X}(\theta,\phi-\xi_n^{(k)};\sum_{l=0}^{k-1}\xi_n^{(l)})e^{j\{\beta\vec{r}_n\cdot\vec{u}(\theta,\phi)+\varphi_n\}}. \tag{4.14}$$

where

$$E_{n,co}(\theta,\phi;\textstyle\sum_{l=0}^{k-1}\xi_n^{(l)}) = E_{n,\theta}(\theta,\phi;\textstyle\sum_{l=0}^{k-1}\xi_n^{(l)})\vec{\theta}\cdot\vec{p}_{co} + E_{n,\phi}(\theta,\phi;\textstyle\sum_{l=0}^{k-1}\xi_n^{(l)})\vec{\phi}\cdot\vec{p}_{co} \tag{4.15}$$

$$E_{n,X}(\theta,\phi;\textstyle\sum_{l=0}^{k-1}\xi_n^{(l)}) = E_{n,\theta}(\theta,\phi;\textstyle\sum_{l=0}^{k-1}\xi_n^{(l)})\vec{\theta}\cdot\vec{p}_{X} + E_{n,\phi}(\theta,\phi;\textstyle\sum_{l=0}^{k-1}\xi_n^{(l)})\vec{\phi}\cdot\vec{p}_{X}. \tag{4.16}$$

In the above, $E_{n,\theta}(\theta,\phi;\sum_{l=0}^{k-1}\xi_n^{(l)})$ and $E_{n,\phi}(\theta,\phi;\sum_{l=0}^{k-1}\xi_n^{(l)})$ are obtained with full-wave simulation after the $(k-1)^{th}$ refining step.

To synthesize a power pattern with desired shape, subject to constraints on sidelobe level (SLL) and XP level (XPL), the cost function utilized in [20] is referenced with proper extension. Suppose that the desired CoP main lobe is denoted by $P_t(\theta,\phi)$, and the anticipated SLL and XPL are denoted by Γ_{SLL} and Γ_{XPL}, respectively. The cost function can be constructed as:

$$f = \frac{W_1}{B}\sum_{b=1}^{B}\{|F_{co}^{(k)}(\theta_b,\phi_b)|^2 - P_t(\theta_b,\phi_b)\}^2 + \frac{W_2}{C}\sum_{c=1}^{C}\frac{1}{4}(X_c+|X_c|)^2 + \frac{W_3}{D}\sum_{d=1}^{D}\frac{1}{4}(Y_d+|Y_d|)^2 \tag{4.17}$$

where

$$\begin{cases} X_c = |F_{co}^{(k)}(\theta_c,\phi_c)|^2 - \Gamma_{SLL};\ \theta_c,\phi_c \in \text{SLL region} \\ Y_d = |F_X^{(k)}(\theta_d,\phi_d)|^2 - \Gamma_{XPL};\ \theta_d,\phi_d \in \text{XPL region.} \end{cases} \tag{4.18}$$

In the above, W_1, W_2, and W_3 are weighting factors. (θ_b,ϕ_b) for $b = 1,2,\cdots,B$ represent sampling angles within the main lobe region of the CoP, whereas (θ_c,ϕ_c) for $c = 1,2,\cdots,C$ represent sampling angles in the sidelobe region. (θ_d,ϕ_d) for $d = 1,2,...,D$ correspond to sampling angles in the region of interest where XPL control is necessary. The principle behind the construction of the cost function (4.17) is similar to that for the cost function (3.7) in Chapter 3. Further explanations are thus omitted here.

4.2.3 The Refined Antenna Rotation and Excitation Phase Optimization Strategy

The overall process of the developed method is listed in **Algorithm 2**. Note that, at the k^{th} step, the rotation angle range is set as:

$$\xi_n^{(k)} \in s^k(1+\delta(-k))[-\pi/2,\pi/2] \tag{4.19}$$

where $\delta(\cdot)$ is a step function, which is equal to 1 for $k = 0$ and 0 for $k > 0$. s $(0 < s < 1)$ is a scale factor. The choice of the parameter s has an impact on the number of refining steps needed to minimize the error. A larger value of s (e.g., closer to 1) typically requires more refining steps and increases the computation time. On the other hand, selecting a smaller value for s leads to faster convergence of the optimization procedure but may affect the resulting performance of the array pattern. s is set to 1/3 throughout this chapter, which has been found to achieve acceptable accuracy in the synthesis examples with typically only three refining steps.

The PSO algorithm, which was used in the Chapter 3, is adopted for the optimization of rotation angles and excitation phases at each step. The optimization procedure using the PSO is outlined in **Algorithm 3**.

Algorithm 2 The developed refined joint rotation/phase optimization algorithm for vectorial shaped pattern synthesis

1: Set the configurations of the antenna array such as element structure, element count and array geometry. Set $P_t(\theta_b, \phi_b)$, Γ_{SLL}, and Γ_{XPL};
2: Acquire VAEPs with full-wave simulation of the array, or by using analytical expressions, or simulation of a single element with periodical boundaries;
3: Set $k = 0$, and initialize $s = 1/3$;
4: Optimize $\xi_n^{(k)} \in s^k[1+\delta(k)][-\pi/2, \pi/2]$ and $\varphi_n^{(k)} \in [0, 2\pi]$ for $n = 1, 2, \cdots, N$ by using the PSO-based shaped pattern synthesis given in **Algorithm 3**.
5: Update the element rotations $\xi_n^{(k)} = \xi_n^{(k)} + \xi_n^{(k-1)}$ for $n = 1, 2, \cdots, N$.
6: With the optimized $\xi_n^{(k)}$ and $\varphi_n^{(k)}$, full-wave simulate the element-rotated array to obtain the real array pattern and acquire all VAEPs at current states of rotations from the simulation;
7: Check if the error meet the prescribed tolerance: if yes, exit the whole procedure; otherwise, set $k = k + 1$ and repeat Step 4 to 7.

Algorithm 3 The developed PSO-based shaped pattern synthesis sub-procedure.

1: Input the desired pattern characteristics including $P_t(\theta_b, \phi_b)$, Γ_{SLL}, Γ_{XPL}, and input the maximum iteration I_m, population size N_p, problem dimension D_p, as well as weighting factors W_1, W_2 and W_3.
2: Randomly generate N_p particles consist of $\{(\xi_n^{(k)}, \varphi_n^{(k)}); |n = 1, 2, ..., N\}$ in the given D_p dimensional solution space.
3: For each particle in the population, evaluate its cost using the designed cost function (4.17).
4: Compare the cost value of the current particle with that of the $pbest$, which is best solution this particle achieved so far. If it is better than $pbest$, let $pbest$ equal the current location, and update the cost value with the current cost value.
5: Compare the current cost value with $gbest$, which is the best solution the whole swarm achieved so far. If the current value is better than that of $gbest$, replace the location and cost value of $gbest$ with that of the current particle.
6: Update the velocity and position of the current particle.
7: Loop to step 3 until the maximum iteration I_m is reached or the best fit rotation angles $\xi_n^{(k)}$ and excitation phases $\varphi_n^{(k)}$ remain unchanged for multiple iterations.

4.3 Synthesis Results

In this section, three typical examples are provided to evaluate the performance of the developed method. Comparisons between synthesized and full-wave simulated results are provided. Furthermore, comparisons with other methods are also included.

4.3.1 Cosecant-Squared Pattern Synthesis for a 29-Dipole Array

In the first example, a cosecant-squared pattern that was obtained in [53] by optimizing 29 nonuniform positions and phases is synthesized with the developed method. This pattern was also synthesized in [20] by optimizing the antenna rotations and excitation phases with the analytical expression of a rotated ideal dipole array without considering the mutual coupling effect. Now, the developed refined joint rotation/phase optimization method is applied to synthesize this pattern. Suppose $\vec{p}_d = \vec{y}$. According to (4.11) and (4.12), it can be known that on the xoz plane, $\vec{p}_{co}$ and $\vec{p}_X$ are parallel to $\vec{\varphi}$ and $\vec{\theta}$, respectively. The same cosecant-squared function as that used in [53] is chosen for the desired main lobe shape, and $\Gamma_{SLL} = \Gamma_{XPL} = -22$ dB are set for the SLL and XPL. In the sub-procedure of PSO-based shaped pattern synthesis, the parameters are set as follows: $D_p = 58$ for the problem dimension, $N_p = 110$ for the population size, $I_m = 2000$ for the maximum number of iterations, and $W_1 = 5$ and $W_2 = W_3 = 1$ for the weighting factors in the cost function.

At the initial step ($k = 0$), the developed method adopts analytical element patterns of rotated dipoles to find initial element rotation angles and phases. The obtained array patterns are given in Fig. 4.3(a). One can see that the SLL is much lower than that obtained in [53]. However, the pattern performance can deteriorate considerably when the mutual coupling is included in practice. To illustrate this, a real rotated dipole array working at 3 GHz is built in which each dipole having a length of 48 mm and diameter of 1 mm is rotated and excited according to the synthesized results in the initial step. The real array pattern is obtained through full-wave simulation, and it is also plotted in Fig. 4.3(a). One can see that the full-wave simulated array pattern including mutual coupling deteriorates significantly in both sidelobe and main lobe regions. The SLL greatly increases from -21.90 dB to -14.73 dB.

To improve the synthesis accuracy, the developed method adopts several refining

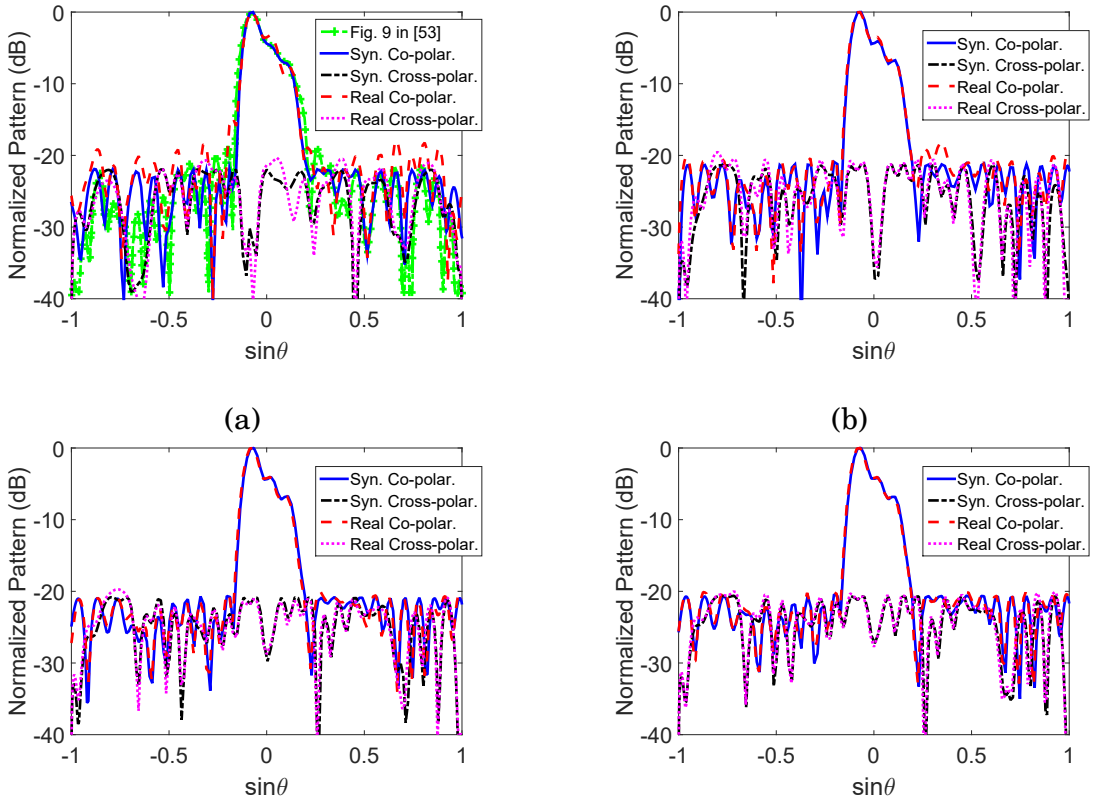

Figure 4.3: The cosecant-squared shaped patterns synthesized by the developed method as well as the full-wave simulated real patterns. (a) shows the results at the initial step, as well as the pattern obtained in [53] for comparison, and (b)-(d) show results obtained in the 1^{st}, 2^{nd} and 3^{rd} refining step, respectively.

steps, as described in **Algorithm 3**. By setting $s = 1/3$, the allowable element rotation angle range becomes smaller and smaller as k increases. Fig. 4.3(b)-(d) show the patterns using the rotations and phases obtained at three refining steps, respectively. As can be seen, as the number of refining steps increases, the synthesized pattern becomes more and more approaching the real one. At the 3^{rd} step, they become almost the same. Table 4.1 shows the SLL and XPL for the synthesized and real array patterns at different refining steps of the developed method. At the 3^{rd} step, the obtained real SLL is reduced to -20.05 dB, and the XPL is -20.04 dB. In comparison to the result without refining, 5.32 dB reduction in the SLL is achieved.

Table 4.1: THE SYNTHESIZED AS WELL AS FULL-WAVE SIMULATED SLLS AND XPLS AT THE FOUR STEPS FOR THE ROTATED DIPOLE ARRAY.

k^{th}	Synthesized (dB)		Simulated (dB)	
	SLL	XPL	SLL	XPL
0	−21.90	−21.93	−14.73	−20.32
1	−20.91	−21.23	−18.07	−19.56
2	−20.65	−20.82	−20.04	−19.71
3	−20.42	−20.62	−20.05	−20.04

Fig. 4.4(a) shows the obtained element rotation angles at the four steps, and Fig. 4.4(b) shows the excitation phases. One can see that the synthesized rotations and phases vary significantly from the initial step to the 1^{st} refining step, while they have not changed much from the 2^{nd} and 3^{rd} refining step as expected. Further refining is thus unnecessary.

4.3.2 Synthesis of a 24-Element U-Slot Patch Antenna Array with a Flat-Top Pattern

For further validation, a 24-element 0.55λ-spaced linear array is considered for synthesizing a flat-top power pattern. The array element is designed as a U-slot loaded patch antenna operating at 10 GHz (analysis and design procedure for this antenna can be found in [107]). The geometry of the antenna model with detailed parameters is shown in Fig. 4.5. Assume $\vec{p}_d = \vec{y}$, in the xoz plane, the CoP and XP are $\vec{\varphi}$ and $\vec{\theta}$, respectively. The main lobe region is chosen as $|\theta| \leq 9^\circ$ whilst the sidelobe region is $|\theta| \geq 13^\circ$. Set $\Gamma_{SLL} = \Gamma_{XPL} = -16$ dB, $D_p = 48$, $N_p = 60$ in this example, and other parameters including M, W_1, W_2, and W_3 are the same as those in the first example.

At the initial step, VAEPs are obtained through simulations of a periodic-bounded U-slot loaded patch antenna. The flat-top power pattern is synthesized using the approximated array expressions, but it is observed that there is a difference between the synthesized pattern and the actual one, as depicted in Fig. 4.6(a). The synthesized

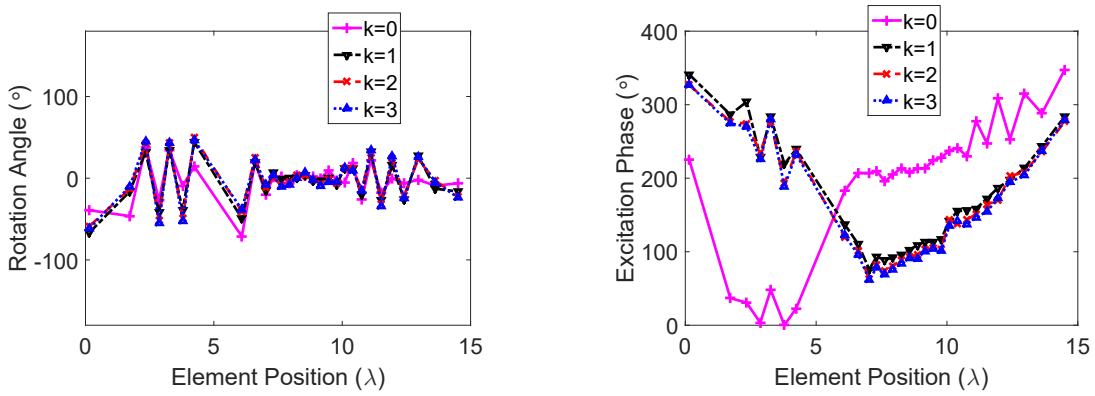

(a) (b)

Figure 4.4: The optimized rotations and excitation phases at the four steps for the cosecant-squared pattern synthesis case. (a) the rotation angles, and (b) the excitation phases.

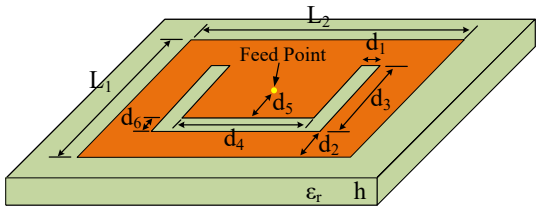

Figure 4.5: Geometry of the U-slot loaded patch antenna. The sizes are given as follows: $d_1 = d_6 = 0.55$ mm, $d_2 = 1.85$ mm, $d_3 = 6.60$ mm, $d_4 = 4.40$ mm, $d_5 = 2.30$ mm, $L_1 = 9.40$ mm, $L_2 = 9.20$ mm, $h = 1.575$ mm, and $\varepsilon_r = 2.2$.

pattern has an SLL of -15.85 dB, XPL of -15.97 dB, and main lobe ripple of ± 0.45 dB. However, the actual pattern has higher values of SLL, XPL, and main lobe ripple, which are -12.75 dB, -13.11 dB, and ± 0.73 dB, respectively. In order to improve the performance of the actual pattern, three refining steps are employed to refine the rotations and phases. The synthesized and full-wave simulated patterns at these refining steps are shown in Figures 4.6(b)-(d), respectively. It is observed that the synthesized patterns increasingly match the corresponding actual ones as the number of refining steps increases. The maximum SLLs, XPLs, and main lobe ripples for both synthesized and actual patterns at different refining steps are listed in Table 4.2. At the 3^{rd} step, the actual SLL and XPL are -14.58 dB and -14.57 dB, respectively, which are very close to

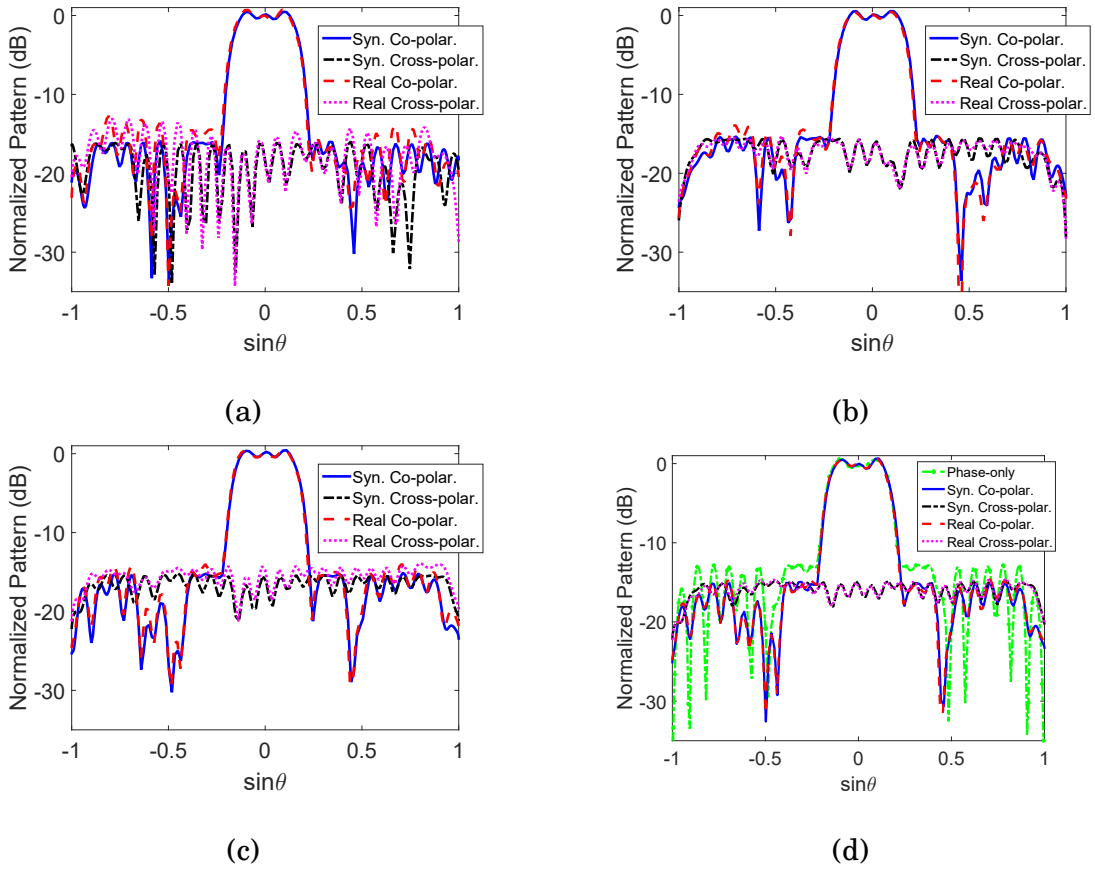

Figure 4.6: The synthesized and full-wave simulated flat-top shaped patterns at different steps. (a) shows the results at the initial step, and (b)-(d) show results obtained in the 1^{st}, 2^{nd}, and 3^{rd} refining step, respectively.

Table 4.2: THE SYNTHESIZED AND FULL-WAVE SIMULATED SLLS, XPLS, AND MAIN LOBE RIPPLE AT THE FOUR STEPS FOR THE ROTATED U-SLOT MICROSTRIP ANTENNA ARRAY.

k^{th}	Synthesized Results (dB)			Simulated Results (dB)		
	SLL	XPL	Ripple	SLL	XPL	Ripple
0	−15.85	−15.97	±0.45	−12.75	−13.11	±0.73
1	−15.23	−15.57	±0.55	−13.92	−15.23	±0.44
2	−15.09	−15.14	±0.44	−13.98	−13.92	±0.45
3	−14.94	−14.74	±0.65	−14.58	−14.57	±0.58

their corresponding synthesized values. Fig. 4.7(a) shows the obtained element rotations, and Fig. 4.7(b) shows the excitation phases. The resulting 24-element rotated U-slot loaded microstrip antenna array after the third refining step is shown in Fig. 4.8.

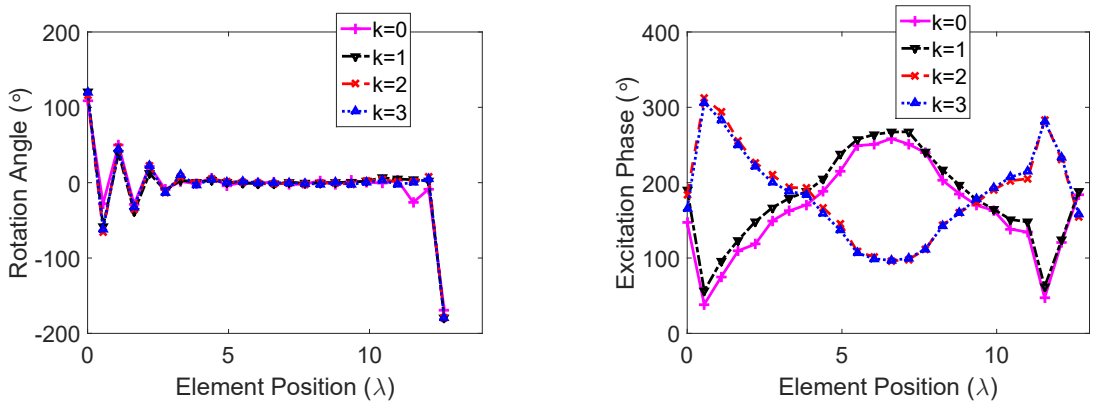

(a) (b)

Figure 4.7: The obtained rotation angles and excitation phases at the four steps in the flat-top shaped pattern synthesis case. (a) the rotation angles, and (b) the excitation phases.

Figure 4.8: The 24-element rotated U-slot loaded patch antenna array obtained in the flat-top shaped pattern synthesis case.

4.3.3 Circular Flat-Top Pattern Synthesis for a 121-Element Cavity-Backed Patch Antenna Planar Array

In this example, the developed method is applied to synthesize a shaped power pattern for a planar array. A circular flat-top pattern was previously synthesized for an 11×11 half-wavelength-spaced planar array in [6] by optimizing the excitation amplitudes and phases without taking into account mutual coupling effects. The main lobe region was defined as $\theta \leq 15^\circ$ and $\phi \in (0^\circ, 360^\circ)$, with a maximum SLL smaller than -10 dB in $\theta \geq 20^\circ$ and $\phi \in (0^\circ, 360^\circ)$, as shown in Fig. 4(a) of [6]. Now, the developed method is utilized to reproduce the pattern by optimizing element rotations and phases without amplitude weighting. The same planar array size is considered, and the element chosen is a cavity-backed patch antenna designed in [108]. Suppose $\vec{p}_d = \vec{y}$, unlike the linear array pattern synthesis cases, the realizable CoP and XP will be changing with (θ, φ)

according to the definitions (4.11) and (4.12). In this example, the same circular flat-top function as that in [6] is set as the target pattern, and the parameters are set as: $\Gamma_{SLL} = \Gamma_{XPL} = -11$ dB, $D_p = 242$, $N_p = 400$. Other parameters are used the same as those in the first example.

Fig. 4.9(a) to (h) show the CoP and XP of both the synthesized and full-wave simulated array patterns synthesized by the developed method, at both the initial and the third refining steps. As is seen, in the end, the synthesized and real patterns are nearly identical for both the CoP and XP components. Table 4.3 lists the maximum SLLs, XPLs, and main lobe ripples for both the synthesized and real array patterns at all four steps. The real SLL and XPL decrease as the refining process is performed. At the 3^{rd} step, the obtained real SLL and XPL are -10.32 dB and -10.18 dB, respectively, and the ripple is ± 1.23 dB. Fig. 4.10 shows the array arrangement obtained with optimized element rotations. When compared with the result in Fig. 4(a) of [6], the current obtained pattern, including mutual coupling, has better sidelobe performance, and the synthesized array does not require amplitude weighting, thereby saving many unequal power dividers.

4.4 Fabrication and Measurement

The 24 rotated U-slot antenna array with a flat-top shaped pattern obtained in Example 2 has been fabricated, as shown in Fig. 4.11. The array is designed and constructed using two substrates with the same relative permittivity ($\varepsilon_r = 2.2$), but with different dimensions. The upper substrate measures 429 mm × 131 mm with a thickness of 1.575 mm, while the lower substrate measures 429 mm × 58 mm with a thickness of 0.508 mm. The array is structured as follows, from top to bottom: rotated U-slot antennas, a radio frequency (RF) ground, and a feeding network. The feeding network of the antenna array is implemented as a Wilkinson power divider. The Wilkinson power divider is a commonly used microwave component that enables power splitting or combining in RF

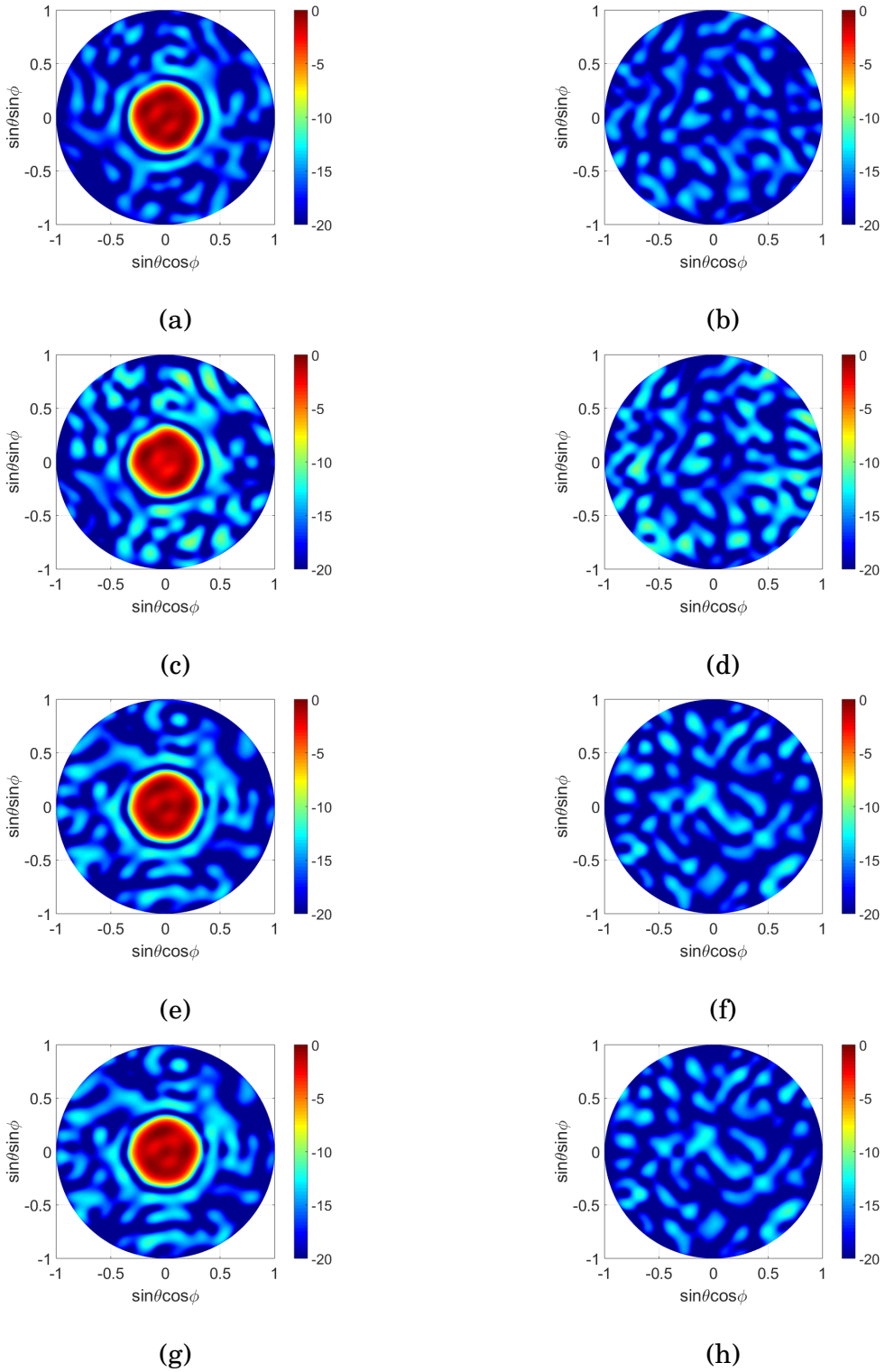

Figure 4.9: The circular flat-top shaped patterns synthesized by the developed method and the corresponding full-wave simulated ones. (a) and (b) show the synthesized CoP and XP at the initial step; (c) and (d) show the full-wave simulated CoP and XP at the initial step; (e) and (f) show the synthesized CoP and XP at 3^{rd} refining step; (g) and (h) show the full-wave simulated CoP and XP at the 3^{rd} refining step.

Table 4.3: THE SYNTHESIZED AS WELL AS THE FULL-WAVE SIMULATED SLLS, XPLS, AND MAIN LOBE RIPPLE AT THE FOUR STEPS IN THE CIRCULAR FLAT-TOP SHAPED PATTERN SYNTHESIS EXAMPLE.

k^{th}	Synthesized Results (dB)			Simulated Results (dB)		
	SLL	XPL	Ripple	SLL	XPL	Ripple
0	−10.62	−10.83	±1.14	−7.57	−8.25	±1.60
1	−10.77	−10.63	±1.09	−9.25	−9.88	±1.19
2	−10.30	−10.20	±1.14	−9.83	−10.39	±1.17
3	−10.32	−10.32	±1.17	−10.32	−10.18	±1.23

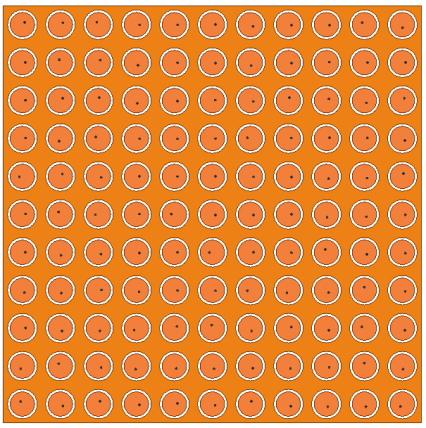

Figure 4.10: The obtained element-rotated planar array in the circular flat-top shaped pattern synthesis example.

and microwave systems. The designed Wilkinson power divider in this study features one input port for connection to the feeding cables and 24 output ports for connection to the rotated antennas through 24 metal vias, which are insulated from the RF ground. 50 Ω resistors are inserted between each pair of branched transmission lines to improve isolation. The Wilkinson power divider is designed to provide equal output amplitudes but different phases. The optimized phases required for achieving the desired flat-top shaped pattern are achieved by incorporating phase shifting lines with varying lengths in the design, as can be seen in Fig. 4.11(b). Finally, to keep the whole structure flat, a hard plastic plate has been attached to the lower substrate, as the substrate layer is thin and long and tends to bend easily.

The measured patterns, along with the simulated ones, are shown in Fig. 4.12. The

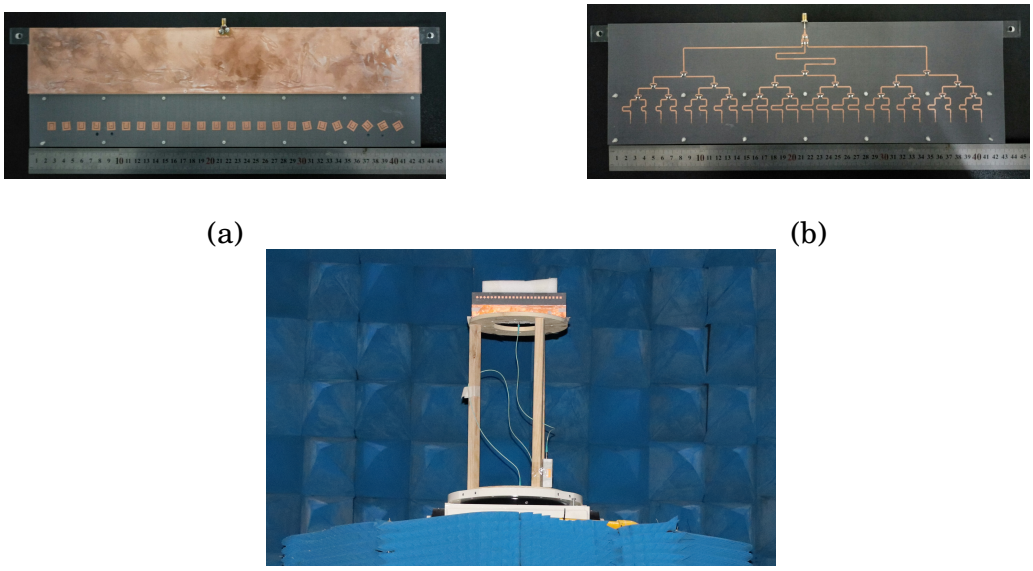

(a) (b)

(c)

Figure 4.11: The fabricated 24-element rotated U-slot microstrip antenna array with a feeding network and a supportive plastic plate, as well as the photo of this array under the test.

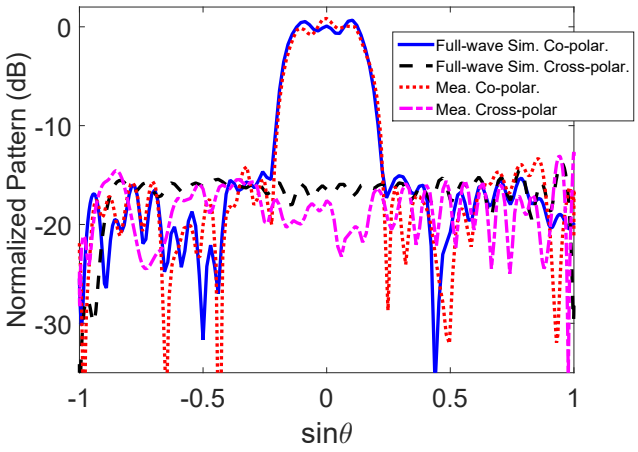

Figure 4.12: The measured and full-wave simulated CoP and XP patterns for the 24-element antenna array integrated with the feeding network.

results indicate that the measured CoP pattern exhibits a main lobe ripple of ±0.84 dB, which is slightly higher than the simulated ripple of ±0.67 dB. Additionally, the measured SLL and XPL are −13.33 dB and −12.67 dB, respectively, which are 1.27 dB and 1.11 dB worse than the simulated values. Although there is a slight degradation

in performance, probably due to fabrication and assembly errors and a non-ideal measurement environment, the measured patterns are in good agreement with the full-wave simulation results.

4.5 Summary

A refined joint element rotation and excitation phase optimization strategy has been developed to synthesize shaped power patterns for linear and planar antenna arrays considering mutual coupling. This strategy is a significant extension of the element rotation technique used only for synthesizing linear arrays with ideally rotated dipoles where an analytical dipole pattern expression is used and mutual coupling effect for practical antenna arrays cannot be considered. For a more general antenna array, the key problem of synthesizing vectorial shaped power patterns by using joint element rotation/phase optimization is that one does not know the pattern expression for an element-rotated array with rotation angles to be optimized. The developed refined optimization strategy provides a very useful solution. Three synthesis examples have been provided. Synthesized results show that the developed refined rotation/phase optimization strategy is quite effective and robust for obtaining shaped patterns for different antenna arrays. The synthesized patterns exhibits the desired CoP main lobe shapes while maintaining reasonable SLL and XPL control. Measured results agree well with the simulated results.

Last but not least, it is noted that the developed strategy does not require nonuniform amplitude weighting which is usually required in conventional shaped pattern synthesis methods, thus avoiding the use of many unequal power dividers.

CHAPTER 5

SHAPED-BEAM PATTERN CYLINDRICAL CONFORMAL ARRAY DESIGN BASED ON ELEMENT ROTATION

5.1 Introduction

In Chapter 4, shaped-beam patterns were synthesized employing the element rotation technique. Linear and planar arrays with arbitrary antenna structures were considered. In many applications like aircraft, antenna arrays are required to be tightly conformed to a curved surface to preserve their aerodynamic or hydrodynamic properties. In this case, conformal arrays must be employed. In this chapter, the element rotation method is extended to synthesize shaped patterns for conformal arrays. Different from linear or planar arrays, antennas in conformal arrays are conformed to curved surfaces. In this case, the rotation will not only change the mutual coupling but cause severe deformation to the rotated antennas. In addition, since different antennas have different normal directions in the conformal array, coordinate transformations for both scalar element patterns and polarization vectors are required to calculate the array pattern of rotated

antennas. Moreover, proper interpolation is also necessary to make all the element patterns transformed into the global coordinate system (GCS) to calculate the array pattern. This chapter will address all these issues and try to synthesize shaped patterns for cylindrical conformal arrays considering mutual coupling employing the element rotation technique.

In this chapter, formulation and algorithm are discussed in the Section 5.2. Section 5.3 presents some numerical results. In Section 5.4, measurement results are presented. Section 5.5 draws the conclusion.

5.2 Formulations and Optimization Algorithm

This section describes the formulations and algorithm that are used to achieve shaped pattern synthesis for cylindrical conformal arrays considering mutual coupling and arbitrary antenna structure.

5.2.1 Vectorial Pattern Approximation of a Rotated Element in Cylindrical Conformal Array

While the following formulation is applicable to cylindrical arrays with multiple rows of elements, for simplicity, a single row configuration is assumed. Consider a cylindrical conformal array with N uniformly distributed elements arranged in a row on the surface of a cylinder with a radius r_0. A GCS xyz with an origin O is established with its y-axis coinciding with the center axis of the cylinder, as illustrated in Fig. 5.1 from a side view in the $+y$-axis direction. For the n^{th} ($n = 1,2,...,N$) element, a local coordinate system (LCS) $x'_n y'_n z'_n$ is established, with x'_n-axis being tangent to the cylinder circular arc, y'_n-axis being parallel to y-axis, and z'_n-axis directed along the radial line passing through the origin O and O'_n, where O'_n denotes the origin of the LCS.

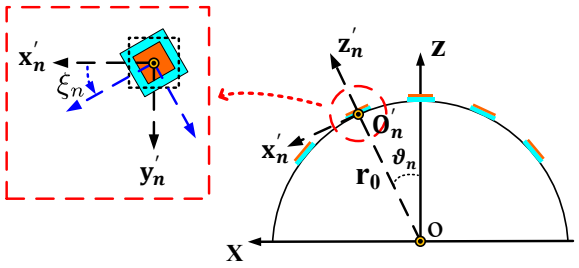

Figure 5.1: Element rotation in cylindrical conformal array.

As depicted in the left inset of Fig. 5.1, suppose the n^{th} element is rotated by an azimuth angle ξ_n with respect to z'_n-axis in its LCS. Its far-field radiation pattern in the LCS can be written as:

$$\vec{E}_n(\theta'_{n,m},\phi'_{n,m};\xi_n) = E_{\theta'_n}(\theta'_{n,m},\phi'_{n,m};\xi_n)\vec{\theta}'_n + E_{\phi'_n}(\theta'_{n,m},\phi'_{n,m};\xi_n)\vec{\phi}'_n \tag{5.1}$$

where $\theta'_{n,m}$ and $\phi'_{n,m}$ denote the elevation and azimuth angle of the LCS, $m = 1,2,...,M$ denote discrete sampling points, $\vec{\theta}'_n$ and $\vec{\phi}'_n$ are the polarization unit vectors in the θ'_n and ϕ'_n directions, respectively. $E_{\theta'_n}(\theta'_{n,m},\phi'_{n,m};\xi_n)$ and $E_{\phi'_n}(\theta'_{n,m},\phi'_{n,m};\xi_n)$ are the θ'_n- and ϕ'_n-components of the vectorial active element pattern (VAEP). Similarly, VAEPs of the elements in the cylindrical array environment can be acquired through full-wave simulation using the high-frequency simulation software (HFSS).

For any given rotation angles ξ_n ($n = 1,2,...,N$), the rotated VAEPs in the cylindrical conformal array can be obtained from a single full-wave simulation of this array. However, in this particular problem, the rotation angles ξ_n are not initially available. Therefore, a suitable method is required to predict the VAEPs of elements with any possible rotation angles for evaluating the pattern performance. An effective method, which has been used in Chapter 4, is to first obtain non-rotated VAEPs by full-wave simulating the array with non-rotated elements. Then, the VAEP of each element rotated by an angle ξ_n can be predicted through mathematical calculations based on the non-rotated VAEP as:

$$\vec{E}_n(\theta'_{n,m},\phi'_{n,m};\xi_n) = E_{\theta'_n}(\theta'_{n,m},\phi'_{n,m}-\xi_n;0)\vec{\theta}'_n + E_{\phi'_n}(\theta'_{n,m},\phi'_{n,m}-\xi_n;0)\vec{\phi}'_n \tag{5.2}$$

Clearly, some inaccuracies caused by the variations of antenna curvature and mutual coupling after rotation are introduced in the rotated VAEP prediction (5.2).

As an illustration, Fig. 5.2 shows the rotation of a conformed antenna. With the VAEP $E_{\theta'_n}(\theta'_{n,m},\phi'_{n,m};0)$ and $E_{\phi'_n}(\theta'_{n,m},\phi'_{n,m};0)$ of the non-rotated element shown in Fig. 5.2 (a), the rotated VAEP can be predicted using (5.2). But owing to the neglect of the antenna curvature variation, the element is actually considered to be rotated with its curvature maintained, as shown in Fig. 5.2 (b). It is much different from the element rotated with the same angle but with real curvature, as shown in Fig. 5.2 (c). Nevertheless, the direct rotation in Fig. 5.2 (b) can be an approximation of the real situation in Fig. 5.2 (c). Generally, given the antenna structure and cylinder configuration, the approximation would be more accurate when the rotation angle is small.

To analyze the effect of rotation angles on the approximation error, a rotated element pattern approximation example is presented. A 9-element cylindrical array with a radius of $r_0 = 255.5$ mm is considered, and the U-slot loaded patch antenna shown in Fig. 4.5 is selected as the element. The antennas are evenly distributed with an inter-element spacing of 0.59λ in the circumferential direction, corresponding to an angular interval of 4°. Initially, all elements are not rotated. The array is simulated using the HFSS, and the θ- and ϕ-component element patterns of the center element are acquired from the simulation. The proposed approximation method is then applied to predict the element patterns with rotation angles of 3.33°, 10°, 30°, and 60° using the acquired element patterns. In parallel, several full-wave simulations are conducted with the center element rotated by 3.33°, 10°, 30°, and 60°, respectively (the rest elements remain unchanged). The simulated rotated element patterns are obtained from these simulations and serve as comparisons to evaluate the error of the approximated patterns.

The predicted and full-wave simulated θ- and ϕ-component electrical patterns are illustrated in Fig. 5.3 and Fig. 5.4, respectively. It can be observed that both electrical

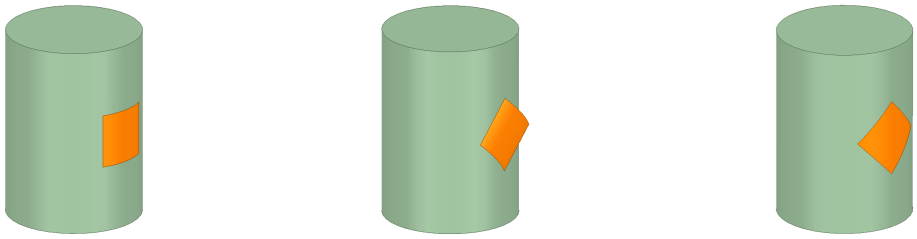

(a) (b) (c)

Figure 5.2: Illustration of the antenna curvature variation when rotating an antenna in conformal array. (a) without rotation, (b) directly rotated without considering deformation, and (c) actual antenna rotation status.

components generally exhibit increasing variations between the approximated and simulated patterns as the rotation angle increases. To quantify the approximation error, the root mean squared errors (RMSEs) are calculated between the predicted and simulated electrical field amplitudes. The RMSE values corresponding to different rotation angles are depicted in Fig. 5.5, further demonstrating a general increase in error with larger rotation angles. These investigations demonstrate that as the rotation angle decreases, the approximation accuracy is generally improved. Therefore, a refined strategy can naturally be exploited to gradually increase the approximation accuracy.

In order to calculate the array pattern, it is necessary to express the rotated VAEPs of the different elements as functions of θ and ϕ in the common GCS by performing a proper transformation. It is important to note that different elements in the cylindrical array have different normal directions, which means that the LCSs in which the elements are rotated have both translational and rotational transformation relations with the GCS, as shown in Fig. 5.1. This is a more complicated situation than that of linear and planar arrays, where the LCSs only have a translational transformation relation with the GCS. Therefore, in addition to transforming both components of the scalar pattern, i.e., $E_{\theta'_n}(\theta'_{n,m},\phi'_{n,m}-\xi_n;0)$, $E_{\phi'_n}(\theta'_{n,m},\phi'_{n,m}-\xi_n;0)$, it is also necessary to transform the polarization unit vectors $\vec{\theta}'_n$ and $\vec{\phi}'_n$ from LCS to GCS.

Firstly, $\vec{\theta}'_n$ and $\vec{\phi}'_n$ can be expressed in the LCS by the Cartesian unit vectors $\vec{x}'_n$, $\vec{y}'_n$,

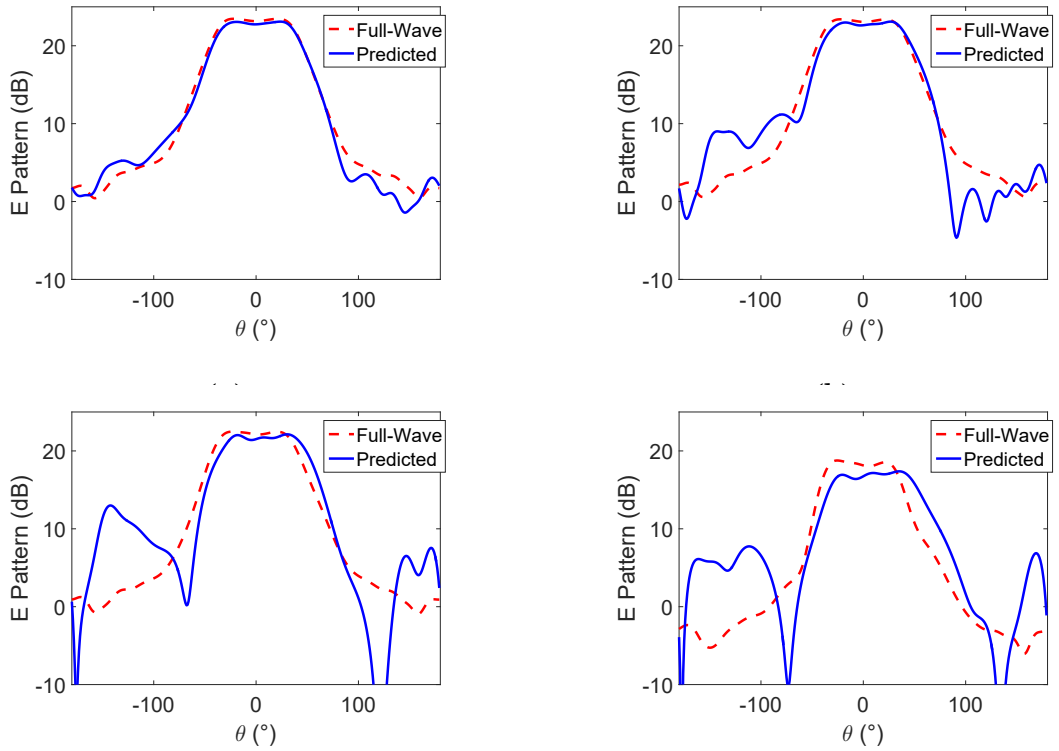

(c) (d)

Figure 5.3: The predicted and full-wave simulated θ-component electrical patterns in the main observation cut of a center element with rotation angles of (a) 3.33°, (b) 10°, (c) 30°, and (d) 60°, respectively.

and $\vec{z}'_n$ as:

$$\vec{\theta}'_n = \cos\theta'_{n,m}\cos\phi'_{n,m}\vec{x}'_n + \cos\theta'_{n,m}\sin\phi'_{n,m}\vec{y}'_n - \sin\theta'_{n,m}\vec{z}'_n \tag{5.3}$$

$$\vec{\phi}'_n = -\sin\phi'_{n,m}\vec{x}'_n + \cos\phi'_{n,m}\vec{y}'_n \tag{5.4}$$

By using the coordinate transformation matrix from LCS to GCS

$$\mathbf{M}_t = \begin{bmatrix} \cos\vartheta_n & 0 & -\sin\vartheta_n \\ 0 & 1 & 0 \\ \sin\vartheta_n & 0 & \cos\vartheta_n \end{bmatrix}, \tag{5.5}$$

$\vec{\theta}'_n$ and $\vec{\phi}'_n$ can be expressed in the GCS as:

$$\vec{\theta}'_n = [\cos\theta'_{n,m}\cos\phi'_{n,m}, \cos\theta'_{n,m}\sin\phi'_{n,m}, -\sin\theta'_{n,m}]\mathbf{M}_t[\,\vec{x},\vec{y},\vec{z}\,]^T \tag{5.6}$$

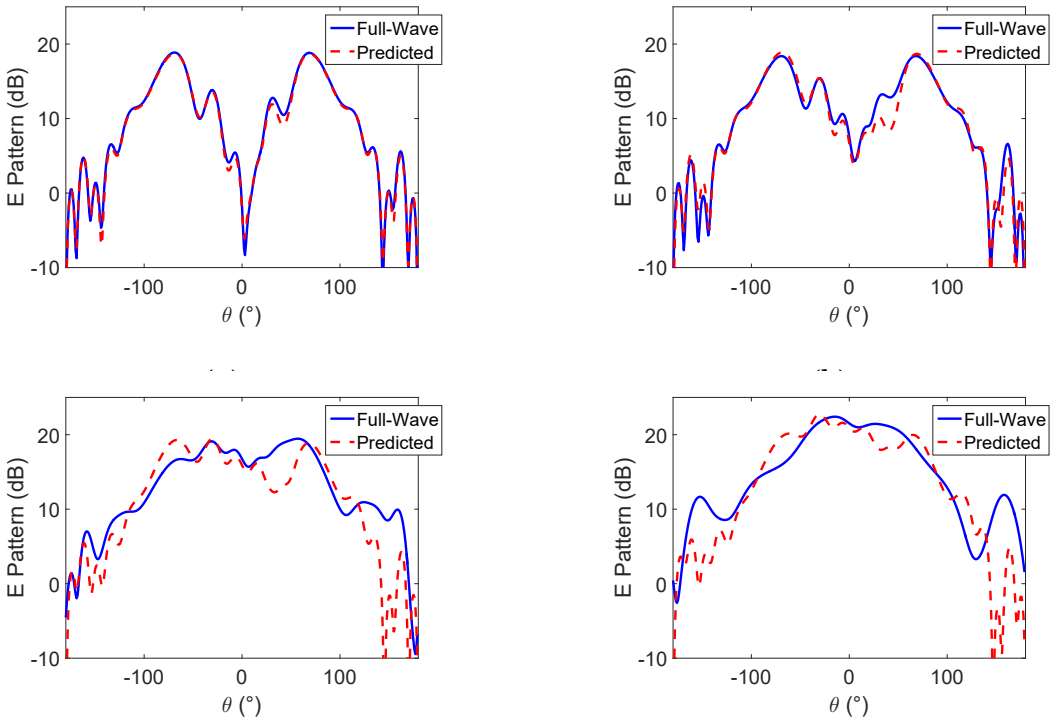

(c) (d)

Figure 5.4: The predicted and full-wave simulated ϕ-component electrical patterns in the main observation cut of a center element with rotation angles of (a) 3.33°, (b) 10°, (c) 30°, and (d) 60°, respectively.

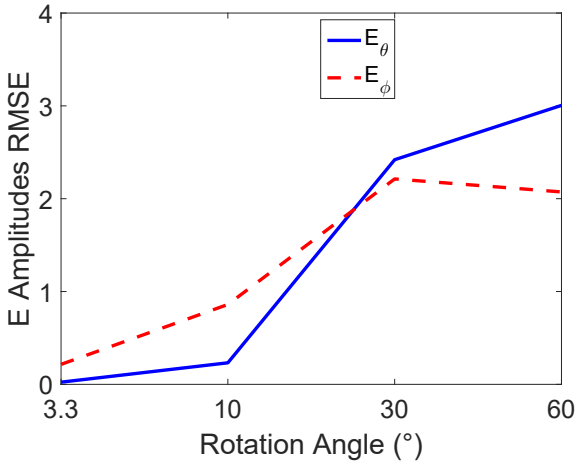

Figure 5.5: The root mean squared errors (RMSEs) of the predicted and simulated E_θ and E_ϕ with different rotation angles.

$$\vec{\phi}'_n = [\ -\sin\phi'_{n,m}, \cos\phi'_{n,m}, 0\ ]\mathbf{M}_t[\ \vec{x}, \vec{y}, \vec{z}\ ]^T \tag{5.7}$$

where ϑ_n denotes the elevation angles of the n^{th} element in the GCS as shown in Fig. 5.1, and the superscript $[\cdot]^T$ denotes the matrix transpose.

Secondly, to express the scalar pattern $E_{\theta'_n}(\theta'_{n,m}, \phi'_{n,m} - \xi_n; 0)$ and $E_{\phi'_n}(\theta'_{n,m}, \phi'_{n,m} - \xi_n; 0)$ of the VAEP as functions of θ and ϕ in the GCS through a rotational and a translational transformation, a method illustrated in Fig. 5.6 can be used. For the rotational transformation, given that the scalar pattern of the VAEP and its spatial angles $\theta'_{n,m}$ and $\phi'_{n,m}$ of the LCS are known, it is possible to obtain the scalar pattern of the VAEP in the GCS by associating ($\theta'_{n,m}$, $\phi'_{n,m}$) with (θ, ϕ) through a proper method. One approach is to express an arbitrary propagation unit vector $\vec{u}$ simultaneously in the LCS and GCS, and then use this unit vector as a medium to establish the relationship between ($\theta'_{n,m}$, $\phi'_{n,m}$) and (θ, ϕ). To achieve this, $\vec{u}$ can be expressed in the LCS as follows:

$$\vec{u} = \sin\theta'_{n,m}\cos\phi'_{n,m}\vec{x}'_n + \sin\theta'_{n,m}\sin\phi'_{n,m}\vec{y}'_n + \cos\theta'_{n,m}\vec{z}'_n \tag{5.8}$$

It can also be expressed in the GCS as:

$$\vec{u} = u_x\vec{x} + u_y\vec{y} + u_z\vec{z} \tag{5.9}$$

where u_x, u_y and u_z can be obtained as:

$$\begin{bmatrix} u_x \\ u_y \\ u_z \end{bmatrix} = \mathbf{M}_t^T \begin{bmatrix} \sin\theta'_{n,m}\cos\phi'_{n,m} \\ \sin\theta'_{n,m}\sin\phi'_{n,m} \\ \cos\theta'_{n,m} \end{bmatrix} \tag{5.10}$$

Then, $\theta_{n,m}$ and $\phi_{n,m}$ can be associated with $\theta'_{n,m}$ and $\phi'_{n,m}$ by:

$$\begin{cases} \theta_{n,m} = \arccos u_z, \quad \theta_{n,m} \in [0, \pi] \\ \phi_{n,m} = \arctan\left(\dfrac{u_y}{u_x}\right), \quad \phi_{n,m} \in [0, 2\pi]. \end{cases} \tag{5.11}$$

Once the relationship between $\theta_{n,m}$ and $\phi_{n,m}$ of the GCS and $\theta'_{n,m}$ and $\phi'_{n,m}$ of the LCS are obtained, one can naturally obtain the rotated VAEP in the GCS:

$$\vec{E}_n(\theta_{n,m}, \phi_{n,m}; \xi_n) \approx E_{n,\theta}(\theta_{n,m}, \phi_{n,m}; \xi_n)e^{j\beta\vec{r}_n\cdot\vec{u}}\vec{\theta}'_n + E_{n,\phi}(\theta_{n,m}, \phi_{n,m}; \xi_n)e^{j\beta\vec{r}_n\cdot\vec{u}}\vec{\phi}'_n \tag{5.12}$$

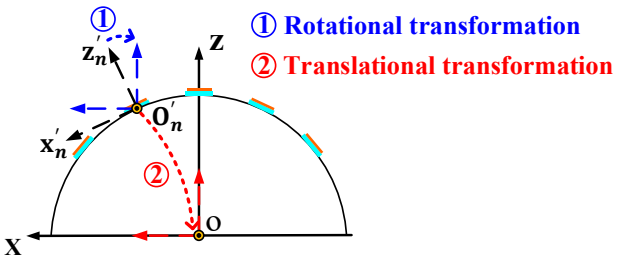

Figure 5.6: Illustration of the transformation from the LCS to the GCS.

where $j=\sqrt{-1}$ is the imaginary unit, $\beta=2\pi/\lambda$, $\vec{r}_n$ and $\vec{u}$ are the n^{th} element location and the propagation unit vector, respectively, both expressed in the GCS. $\vec{\theta}'_n$ and $\vec{\phi}'_n$ are expressed in GCS obtained with (5.6) and (5.7). $E_{n,\theta}(\theta_{n,m},\phi_{n,m};\xi_n)$ and $E_{n,\phi}(\theta_{n,m},\phi_{n,m};\xi_n)$ are representations of $E_{\theta'_n}(\theta'_{n,m},\phi'_{n,m}-\xi_n;0)$ and $E_{\phi'_n}(\theta'_{n,m},\phi'_{n,m}-\xi_n;0)$ in the GCS, respectively. $e^{j\beta\vec{r}_n\cdot\vec{u}}$ is a phase term applied to achieve the aforementioned translational transformation from O'_n to O as shown in Fig. 5.6.

5.2.2 The Spatial Angle Sampling Grid Unification to Obtain the Array Pattern

To facilitate the formulation of vectorial array pattern expressions, the co-polarized (CoP) and cross-polarized (XP) definitions (4.11) and (4.12) are employed to calculate the CoP and XP patterns, respectively. The CoP/XP pattern of the n^{th} rotated element can be obtained through vector projection as:

$$E_{n,co}(\theta_{n,m},\phi_{n,m};\xi_n)\approx E_{n,\theta}(\theta_{n,m},\phi_{n,m};\xi_n)e^{j\beta\vec{r}_n\cdot\vec{u}}\vec{\theta}'_n\cdot\vec{p}_{co}+E_{n,\phi}(\theta_{n,m},\phi_{n,m};\xi_n)e^{j\beta\vec{r}_n\cdot\vec{u}}\vec{\phi}'_n\cdot\vec{p}_{co} \tag{5.13}$$

$$E_{n,X}(\theta_{n,m},\phi_{n,m};\xi_n)\approx E_{n,\theta}(\theta_{n,m},\phi_{n,m};\xi_n)e^{j\beta\vec{r}_n\cdot\vec{u}}\vec{\theta}'_n\cdot\vec{p}_{X}+E_{n,\phi}(\theta_{n,m},\phi_{n,m};\xi_n)e^{j\beta\vec{r}_n\cdot\vec{u}}\vec{\phi}'_n\cdot\vec{p}_{X} \tag{5.14}$$

From (5.10) and (5.11), it is seen that the spatial angles ($\theta_{n,m}$, $\phi_{n,m}$) are non-linearly related to ($\theta'_{n,m}$, $\phi'_{n,m}$). Since the VAEPs in the LCSs are obtained from full-wave simulation using discrete and uniform spatial angle samplings of $\theta'_{n,m}$ and $\phi'_{n,m}$, the calculated

$\theta_{n,m}$ and $\phi_{n,m}$ are nonuniformly distributed, and they differ for different elements. Therefore, to calculate the array pattern, it is necessary to perform proper interpolation that allows all the rotated VAEPs to share an identical spatial angle sampling grid of θ_m and ϕ_m. A scattered interpolation approach based on the Delaunay triangulation is utilized here. The scattered VAEPs data is used as vertexes to generate triangular surfaces based on the Delaunay triangulation criteria [109]. These surfaces can be used to evaluate VAEP values at any query angle θ_m and ϕ_m lying in the convex hull of the known scattered data set of $\theta_{n,m}$ and $\phi_{n,m}$. As a result, the CoP and XP of the rotated VAEP at a unified spatial angle sampling grid in the GCS can be obtained as:

$$E_{n,co}(\theta_{n,m},\phi_{n,m};\xi_n) \overset{f_{Int}}{\Longrightarrow} E^{Int}_{n,co}(\theta_m,\phi_m;\xi_n) \tag{5.15}$$

$$E_{n,X}(\theta_{n,m},\phi_{n,m};\xi_n) \overset{f_{Int}}{\Longrightarrow} E^{Int}_{n,X}(\theta_m,\phi_m;\xi_n) \tag{5.16}$$

where f_{Int} denotes the scattered interpolation function. For convenience, the Matlab integrated Delaunay-triangulation-based scattered interpolation function is employed here.

Finally, the CoP and XP patterns of the cylindrical conformal array with rotated antenna elements are obtained as:

$$F_{co}(\theta_m,\phi_m) = \sum_{n=1}^{N} E^{Int}_{n,co}(\theta_m,\phi_m;\xi_n)e^{j\varphi_n} \tag{5.17}$$

$$F_X(\theta_m,\phi_m) = \sum_{n=1}^{N} E^{Int}_{n,X}(\theta_m,\phi_m;\xi_n)e^{j\varphi_n} \tag{5.18}$$

where φ_n is excitation phase of the n^{th} element. Note that, though (5.17) and (5.18) are derived considering a cylindrical conformal array with one row of elements, it is also applicable to cylindrical arrays with multiple rows of elements.

5.2.3 Shaped-Beam Cylindrical Array Synthesis with the Refined Rotation/Phase Optimization

To obtain ξ_n and φ_n for $n = 1,2,...,N$ that can yield desired shaped pattern with the lowest possible sidelobe level (SLL) and XP level (XPL) for cylindrical conformal array, a cost function is constructed as:

$$f_c = \frac{W_1}{B}\sum_{b=1}^{B}\left[|F_{co}(\theta_b,\phi_b)|^2 - P_t(\theta_b,\phi_b)\right]^2 + \frac{W_2}{C}\sum_{c=1}^{C}\left[\frac{1}{4}(X_c+|X_c|)\right]^2 + \frac{W_3}{D}\sum_{d=1}^{D}\left[\frac{1}{4}(Y_d+|Y_d|)\right]^2 \tag{5.19}$$

where W_1, W_2 and W_3 are weighting coefficients. $P_t(\theta_b,\phi_b)$ is the desired main lobe, where (θ_b,ϕ_b) for $b = 1,2,...,B$ are sampling angles in the CoP main lobe region. $X_c = |F_{co}(\theta_c,\phi_c)|^2 - \Gamma_{SLL}$, where (θ_c,ϕ_c) for $c = 1,2,...,C$ are sampling angles in the CoP sidelobe region, and Γ_{SLL} is the desired SLL. $Y_d = |F_X(\theta_d,\phi_d)|^2 - \Gamma_{XPL}$, where (θ_d,ϕ_d) for $d = 1,2,...,D$ are sampling angles in the region where the XPL is required to be constrained, and Γ_{XPL} is the desired XPL. Explanations for the cost function (5.19) are omitted here since the design principle is similar to that of the cost function (3.7) in Chapter 3. With (5.19), the constriction factor particle swarm optimization (PSO) is employed for the optimization.

Since the effects of antenna deformation and mutual coupling variations are neglected in (5.2), the shaped-beam pattern synthesized using (5.17) and (5.18) through joint rotation and phase optimization would differ greatly from the actual patterns. To improve the accuracy, a refined strategy is adopted. In the refinement, the previous cylindrical array with non-rotated elements is modified and then simulated to acquire updated VAEPs. Then, with the updated VAEPs, joint rotation and phase optimization is performed again, but within a smaller rotation angle range. Let $\xi_n^{(k)}$ and $\varphi_n^{(k)}$ be the rotation angle and excitation phase of the n^{th} element at the k^{th} step, where $k = 0,1,2,\ldots,K$ ($k = 0$ represents the initial step). At the k^{th} step of refinement, the CoP and XP patterns

can be obtained:

$$F_{co}^{(k)}(\theta_m,\phi_m)=\sum_{n=1}^{N}E_{n,co}^{Int}(\theta_m,\phi_m;\sum_{l=0}^{k}\xi_n^{(l)})e^{j\varphi_n^{(k)}} \tag{5.20}$$

$$F_{X}^{(k)}(\theta_m,\phi_m)=\sum_{n=1}^{N}E_{n,X}^{Int}(\theta_m,\phi_m;\sum_{l=0}^{k}\xi_n^{(l)})e^{j\varphi_n^{(k)}} \tag{5.21}$$

where $E_{n,co}^{Int}(\theta_m,\phi_m;\sum_{l=0}^{k}\xi_n^{(l)})$ and $E_{n,X}^{Int}(\theta_m,\phi_m;\sum_{l=0}^{k}\xi_n^{(l)})$ are the rotated CoP and XP VAEPs of the n^{th} element in the GCS, that are obtained with its rotated VAEP $E_{n,co}(\theta'_{n,m},\phi'_{n,m};\sum_{l=0}^{k}\xi_n^{(l)})$ and $E_{n,X}(\theta'_{n,m},\phi'_{n,m};\sum_{l=0}^{k}\xi_n^{(l)})$ in LCS through proper transformations of the scalar patterns and polarization unit vectors, polarization vector projection, and scattered interpolation. $E_{n,co}(\theta'_{n,m},\phi'_{n,m};\sum_{l=0}^{k}\xi_n^{(l)})$ and $E_{n,X}(\theta'_{n,m},\phi'_{n,m};\sum_{l=0}^{k}\xi_n^{(l)})$ can be obtained as:

$$\begin{aligned}E_{n,co}(\theta'_{n,m},\phi'_{n,m};\sum_{l=0}^{k}\xi_n^{(l)})\approx{}& E_{\theta'_n}(\theta'_{n,m},\phi'_{n,m}-\xi_n^{(k)};\sum_{l=0}^{k-1}\xi_n^{(l)})\vec{\theta}'_n\cdot\vec{p}_{co}+\\ & E_{\phi'_n}(\theta'_{n,m},\phi'_{n,m}-\xi_n^{(k)};\sum_{l=0}^{k-1}\xi_n^{(l)})\vec{\phi}'_n\cdot\vec{p}_{co}\end{aligned} \tag{5.22}$$

$$\begin{aligned}E_{n,X}(\theta'_{n,m},\phi'_{n,m};\sum_{l=0}^{k}\xi_n^{(l)})\approx{}& E_{\theta'_n}(\theta'_{n,m},\phi'_{n,m}-\xi_n^{(k)};\sum_{l=0}^{k-1}\xi_n^{(l)})\vec{\theta}'_n\cdot\vec{p}_{X}+\\ & E_{\phi'_n}(\theta'_{n,m},\phi'_{n,m}-\xi_n^{(k)};\sum_{l=0}^{k-1}\xi_n^{(l)})\vec{\phi}'_n\cdot\vec{p}_{X}\end{aligned} \tag{5.23}$$

Similarly, in the refining steps, the rotation angles $\xi_n^{(k)}$ are set to become smaller and smaller as k increases. As $\xi_n^{(k)}$ becomes small enough, the synthesized pattern would be almost identical to the full-wave simulated one since the antenna curvature and mutual coupling would not change much. After K refining steps, the total rotation angles and final excitation phases would be $\xi_n=\sum_{k=0}^{K}\xi_n^{(k)}$ and $\varphi_n=\varphi_n^{(K)}$, respectively. The detailed procedure of the developed shaped-beam cylindrical conformal array synthesis with PSO-based refined rotation/phase optimization method is presented in **Algorithm 4**.

Algorithm 4 Procedure of the vectorial shaped pattern synthesis considering mutual coupling for cylindrical conformal array with the PSO-based joint rotation/phase optimization method.

1: Set the cylindrical conformal array configurations including the cylinder radius r_0, element number N, element intervals ϑ_n and d_y, antenna structure, desired main lobe $P_t(\theta_b, \phi_b)$, as well as the desired SLL Γ_{SLL} and XPL Γ_{XPL};
2: Input the PSO parameters including the maximum iteration I_m, population size N_p, and weighting factors W_1, W_2, and W_3;
3: Model the cylindrical conformal array with non-rotated elements, and then simulate to acquire all the embedded VAEPs in the LCSs.
4: Set $k = 0$;
5: Randomly generate N_p particles consists of the rotation angles $\xi_n^{(k)} \in s^k[1+\delta(k)][-\pi/2, \pi/2]$ ($s \in (0,1)$, $\xi_n^{(k)}$ decreases as k increases) and excitation phases $\varphi_n^{(k)} \in [0, 2\pi]$ for $n = 1, 2, \cdots, N$.
6: With the simulated VAEPs, predict the VAEPs of the elements rotated by $\xi_n^{(k)}$ with (5.2), and express them in the GCS through transformations of both the scalar patterns and polarization unit vectors, and then interpolate to calculate the array pattern.
7: Optimize $\xi_n^{(k)}$ and $\varphi_n^{(k)}$ by using the PSO with the guidance of the cost function (5.19) to synthesize desired shaped pattern with reduced SLL and constrained XPL.
8: Update the array in HFSS: flatten the antennas from its previous curvature, rotate with the optimized angles $\xi_n^{(k)}$, and re-conform to the cylinder; set the excitation phases as $\varphi_n^{(k)}$. Simulate the updated array to acquire the real array patterns.
9: Check if the error meet a preset tolerance: if so, output $\xi_n = \sum_0^k \xi_n^{(k)}$ and $\varphi_n = \varphi_n^{(k)}$ and exit; otherwise, acquire all the VAEPs of the updated array, set $k = k + 1$ and loop to Step 5.

5.3 Synthesis Results

In this section, three shaped-beam cylindrical conformal array synthesis examples are presented to evaluate the developed method. In the examples, the rotation angle range at the k^{th} step is chosen as $\xi_n^{(k)} \in s^k[1+\delta(-k)][-\pi/2, \pi/2]$, where $\delta(k) = 1$ for $k = 0$ and $\delta(k) = 0$ for $k = 1, 2, ..., K$. s ($0 < s < 1$) is a scale factor. If a larger value of s is used, more refining steps are required to converge, while a smaller s can lead to faster convergence but may limit the obtained pattern performance. Therefore, $s = 1/3$ is used to balance pattern performance and time cost. In this case, only $K = 3$ refining steps are required to obtain an accurate result. All the examples were tested on a workstation with an Intel Xeon 6258R CPU at 2.70 GHz.

5.3.1 Flat-Top Pattern Synthesis for a Cylindrical Array of 24 U-slot Loaded Patch Antennas

The first example illustrates the application of a refined joint rotation/phase optimization method to synthesize a flat-top shaped pattern for a 24-element cylindrical conformal array. The radius of the cylinder is set to $r_0 = 255.5$ mm and the U-slot loaded patch antenna shown in (4.5) is chosen as the element. The 24 U-slot loaded patch antennas are evenly distributed with an inter-element spacing of 0.59λ in the circumferential direction (the angular interval is 4°). Assuming $\vec{p}_d = \vec{y}$, the CoP and XP directions on the principal observation plane (xoz plane) are respectively identical to $\vec{\phi}$ and $\vec{\theta}$ according to the definitions in (4.11) and (4.12). The flat-top shaped beam region is set as $\theta \in [-20°, 15°]$, while the SLL region is $\theta \in [-90°, -26°] \cup [21°, 90°]$. The target SLL and XPL are set as $\Gamma_{SLL} = \Gamma_{XPL} = -16.5$ dB. The parameter settings in the PSO are given as follows: $N_p = 96$ for the population size, $I_m = 2000$ for the maximum number of iterations, and $W_1 = 5$, $W_2 = W_3 = 1$ for the weighting factors.

Initially ($k = 0$), the cylindrical array with non-rotated antenna elements is modeled and simulated in HFSS to obtain the VAEPs. Subsequently, the rotation angles $\xi_n \in [-\pi, \pi]$ and phases $\varphi_n \in [0, 2\pi]$ for $n = 1, 2, ..., N$ are optimized to synthesize the desired flat-top pattern. The synthesized array patterns are presented in Fig. 5.7(a), which indicate that the achieved SLL, XPL, and main lobe ripple are −16.06 dB, −16.10 dB, and ±0.64 dB, respectively. Nevertheless, the synthesized patterns may differ significantly from the actual ones as the antenna deformation and mutual coupling change caused by the rotation are disregarded. To demonstrate this, the initial cylindrical array is modified and then simulated again. During the modification, the curved antenna elements are flattened, rotated with the optimized angles, and then re-conformed to the curved surface. The real patterns obtained with full-wave simulation are also depicted in Fig. 5.7(a). As observed, the pattern performance in terms of the main lobe ripple, SLL, and especially

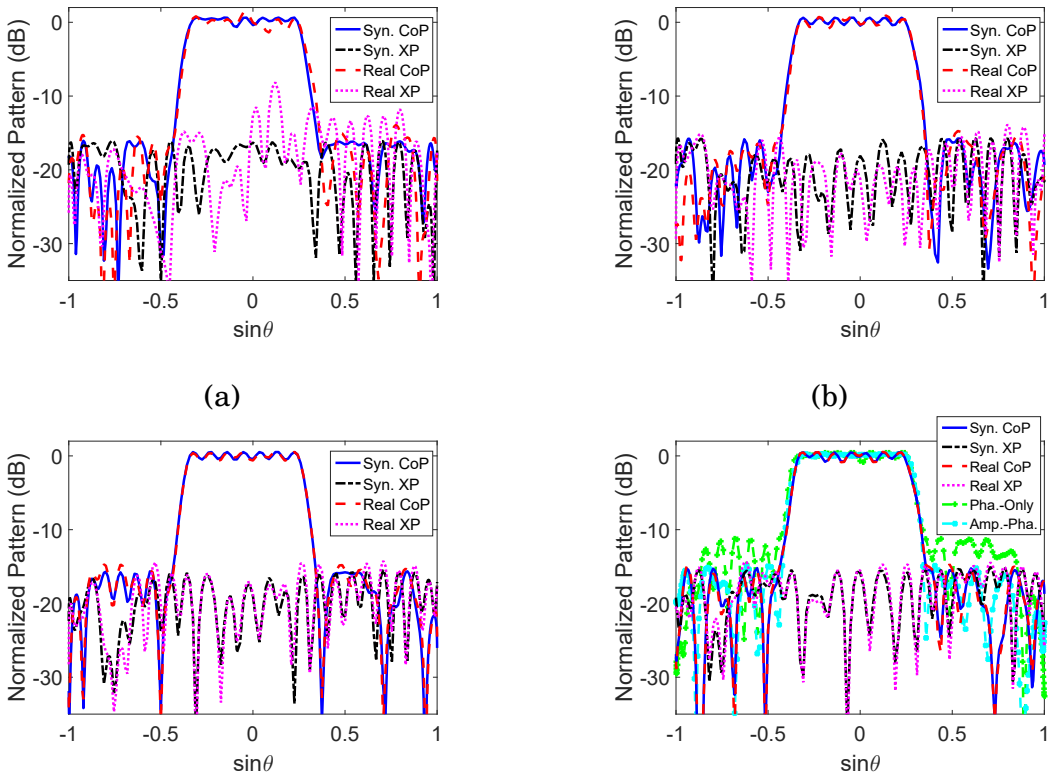

Figure 5.7: The synthesized and full-wave simulated flat-top shaped patterns for the cylindrical array with 24 rotated U-slot loaded patch antennas in the initial (a), 1^{st} (b), 2^{nd} (c), and 3^{rd} (d) refining steps. (d) also shows the patterns obtained by the phase-only and amplitude/phase optimization method.

the XPL (only -8.14 dB) deteriorates considerably compared to the synthesized patterns.

To improve the performance of the real pattern, three refining steps are conducted, where the rotation angles in the 1^{st}, 2^{nd}, and 3^{rd} refining steps are $\pi/6$, $\pi/18$, and $\pi/54$, respectively. The obtained flat-top patterns in the three refining steps are shown in Fig. 5.7(b), (c), and (d), respectively. It can be observed that the discrepancies become smaller as k increases. At the 3^{rd} refining step, the synthesized CoP and XP patterns closely match the real ones. The SLL, XPL, and main lobe ripple of the real pattern are -14.69 dB, -14.37 dB, and ± 0.69 dB, respectively. In comparison to the real pattern obtained in the initial step, the SLL and XPL have been improved by 0.8 dB and 6.23 dB, respectively.

The synthesized results and the comparison with the simulated patterns validate the effectiveness of the developed approach. Table 5.1 shows the SLLs, XPLs, and main lobe ripples of the synthesized and real patterns for different ks. It is important to note that the synthesized SLLs and XPLs tend to slightly deteriorate as k increases. This happens because the VAEPs updated from the full-wave simulated element-rotated arrays in the refining steps consider the complicated mutual coupling change among the rotated elements. Therefore, when synthesizing the shaped-beam pattern with these updated VAEPs in a decreased rotation angle range, the obtained SLL and XPL become slightly worse than those synthesized at the previous step. Nevertheless, the real SLL and XPL gradually improve as k increases, which is the objective of the refined strategy. Fig. 5.8 shows the final status of the obtained cylindrical conformal array with rotated U-slot antennas, and Table 5.2 lists the finally optimized rotation angles and excitation phases. Furthermore, Fig. 5.9 displays the active $|S_{11}|$s of different elements in the array at different k. It is worth noting that the active $|S_{11}|$s of all the elements remain below -15 dB, indicating good matching of the element-rotated cylindrical array.

In this example, it takes around 2.96 minutes for one-time PSO-based rotation/phase optimization and 31 minutes for one-time HFSS simulation of the element-rotated cylindrical conformal array. Therefore, the total time cost for the optimizations and full-wave simulations by the developed method is approximately 2.26 hours. Moreover, based on the Matlab recording profile and the HFSS solution data profile, the memory occupied by the PSO-based optimization and full-wave simulation are 9.4 MB and 20.1 GB, respectively.

As a comparison, the phase-only and amplitude/phase optimization methods are employed to synthesize the 24 U-slot loaded patch cylindrical array to produce the same flat-top pattern by using the PSO. The full-wave simulated non-rotated VAEPs are used as the element patterns. The parameters of the PSO are initialized as those in the joint

Table 5.1: THE SYNTHESIZED AND SIMULATED MAXIMUM SLLS, XPLS, AND MAIN LOBE RIPPLES FOR DIFFERENT kS IN EXAMPLE 1.

k^{th}	Synthesized (dB)			Real (dB)		
	SLL	XPL	Ripple	SLL	XPL	Ripple
0	−16.06	−16.10	±0.64	−13.89	−8.14	±1.40
1	−15.77	−15.68	±0.62	−14.93	−13.31	±1.00
2	−15.64	−15.44	±0.52	−14.70	−14.23	±0.66
3	−15.24	−15.03	±0.61	−14.69	−14.37	±0.69

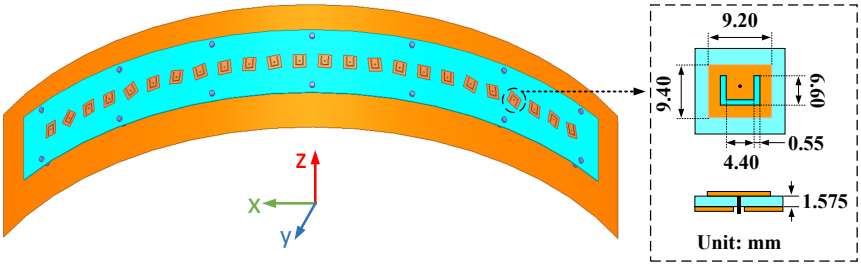

Figure 5.8: The obtained element-rotated cylindrical conformal array with closed view of the adopted U-slot loaded patch antenna in Example 1.

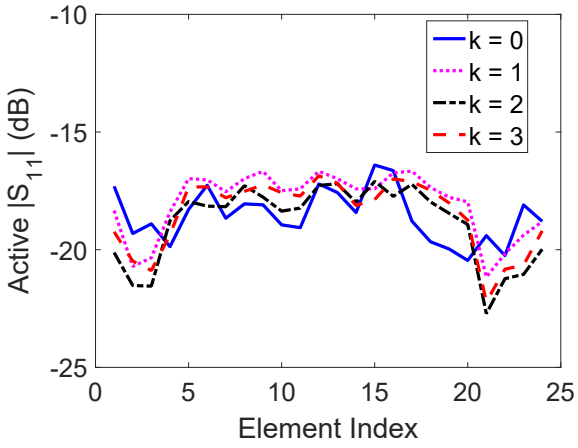

Figure 5.9: The active $|S_{11}|$s of the 24 rotated U-slot loaded patch antennas in the cylindrical array for different ks.

rotation/phase optimization, except that the number of particles is set to $N_p = 48$ for the phase-only method. Fig. 5.7(d) shows the synthesized patterns. As can be seen, the SLL and main lobe ripple obtained by the phase-only method are −11.04 dB and ±0.64 dB, respectively. Although an equivalent main lobe ripple is obtained, the SLL optimized by the phase-only method is much higher than that achieved by the developed method.

The amplitude/phase method is able to obtain a slightly smaller main lobe ripple and an equivalent SLL compared to the developed method. However, amplitude weighting requires many unequal power dividers, which considerably increases the complexity of the feeding network. Furthermore, the optimized excitations are used to excite the array elements in the full-wave simulation. It is shown that the average realized gains achieved by the phase-only, amplitude/phase, and rotation/phase methods are 8.85 dB, 8.70 dB, and 8.84 dB, respectively. Since the array apertures are identical for the three methods, this indicates that the efficiency of the developed element-rotated cylindrical array is equivalent to that of the phase-only or amplitude/phase weighted array with non-rotated elements.

5.3.2 Cosecant-Squared Pattern Synthesis for a 32-Dipole Cylindrical Array

Another example of synthesizing a cosecant-squared pattern for a dipole cylindrical conformal array is presented in this section. A dipole with a length of 48 mm and a diameter of 1 mm working at 3 GHz is chosen as the element. Thirty-two dipoles are uniformly distributed around a cylinder with a radius of $r_0 = 900.4$ mm at an angular interval of 3.5° (the arc distance is 0.55λ). The desired polarization is still set as $\vec{p}_d = \vec{y}$. The cosecant-squared shaped beam region is set as $\theta \in [-20°, 10°]$, while the SLL region is $\theta \in [-90°, -25°] \cup [15°, 90°]$. The desired SLL and XPL are set as $\Gamma_{SLL} = \Gamma_{XPL} = -17$ dB. The population size of the PSO is set to $N_p = 96$, while all other parameters are the same as those used in the first example.

In the initial step ($k = 0$), the full-wave simulated VAEPs of non-rotated elements in the array environment are used for the desired cosecant-squared pattern synthesis. Fig. 5.10(a) displays the synthesized and full-wave simulated patterns, showing that the SLL and XPL values for the synthesized pattern are −16.57 dB and −16.63 dB, respectively.

Table 5.2: THE FINALLY OPTIMIZED ROTATION ANGLES AND EXCITATION PHASES IN EXAMPLE 1 AND EXAMPLE 2.

	Example 1		Example 2	
n	Rotation (°)	Phase (°)	Rotation (°)	Phase (°)
1	-183.2	51.0	23.4	309.0
2	-38.9	133.1	-79.0	259.8
3	-174.8	221.9	70.2	143.7
4	4.4	311.6	174.7	219.2
5	25.2	269.7	165.3	146.1
6	3.7	213.8	-167.1	90.4
7	-8.7	219.2	-172.0	26.0
8	11.9	184.0	-0.4	159.1
9	4.3	166.5	-3.1	115.6
10	-3.9	154.4	-5.0	98.6
11	8.2	134.5	-5.2	99.0
12	0.8	111.2	-1.5	107.3
13	-3.1	123.4	2.4	116.6
14	-1.1	152.6	2.4	121.4
15	6.6	207.1	2.6	153.6
16	-5.8	255.0	-2.8	183.5
17	-1.8	294.1	-12.9	199.9
18	0.1	327.2	26.8	203.1
19	-16.5	28.9	-24.5	268.4
20	7.4	65.8	-162.8	151.6
21	155.4	331.0	-4.8	43.6
22	-7.3	232.5	-8.1	123.7
23	167.0	160.2	1.3	207.5
24	13.2	111.6	-20.8	280.7
25			-125.9	157.4
26			50.3	76.6
27			27.5	144.7
28			21.1	268.1
29			131.4	171.0
30			-91.5	220.8
31			-148.3	73.3
32			36.9	71.9

In contrast, the full-wave simulated pattern yields SLL and XPL values of -14.31 dB and -15.29 dB, respectively. The overall performance of the real patterns is worse than that of the synthesized ones. To improve the pattern performance, three refining steps are employed. The available element rotation angles and phases are set to the same as those in the first example. The synthesized patterns along with the HFSS simulated ones obtained in the refining steps are shown in Fig. 5.10(b), (c), and (d), respectively. As can be seen, with the increase of k, the real patterns are gradually approaching the synthesized ones. At the 3^{rd} refining step, the real CoP and XP patterns are nearly

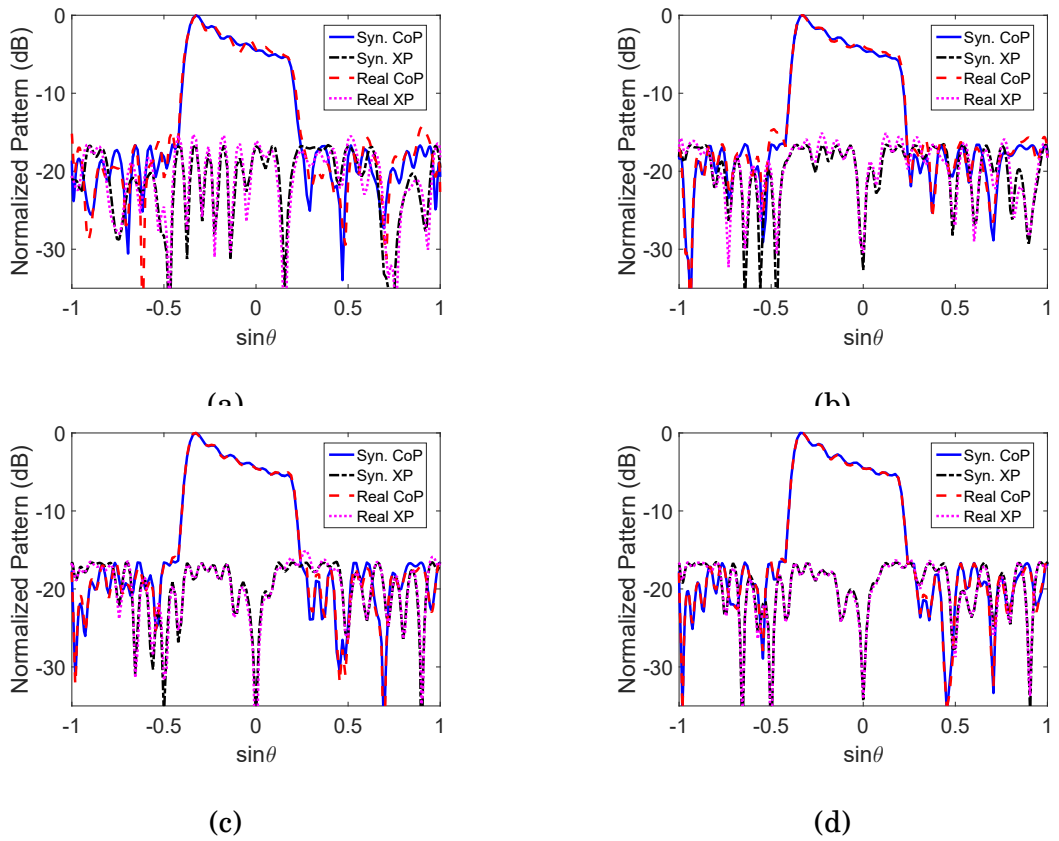

Figure 5.10: The synthesized cosecant-squared shaped patterns as well as the corresponding HFSS simulated real ones for the cylindrical array of 32 rotated dipoles at (a) the initial, (b) 1^{st}, (c) 2^{nd}, and (d) 3^{rd} refining steps.

the same as the synthesized results. The final real SLL is -16.21 dB, while the XPL is -16.22 dB. They are very close to the synthesized -16.41 dB and -16.46 dB, respectively. Table 5.3 gives the synthesized and real SLLs and XPLs for different ks. The finally optimized antenna rotations as well as excitation phases are listed in Table 5.2.

In this example, it takes about 3.92 minutes for one-time PSO-based optimization and 25 minutes for one-time HFSS simulation of the element-rotated cylindrical conformal array. Thus, the total time cost of the developed method is about 1.93 hours. Besides, the memory occupied by the PSO-based optimization and full-wave simulation is 11.2 MB and 13.8 GB, respectively.

Table 5.3: THE MAXIMUM SYNTHESIZED AND REAL SLLS AND XPLS FOR DIFFERENT kS IN EXAMPLE 2.

k^{th}	Synthesized Results (dB)		Simulated Results (dB)	
	SLL	XPL	SLL	XPL
0	−16.57	−16.63	−14.31	−15.29
1	−16.44	−16.50	−14.60	−15.07
2	−16.43	−16.50	−15.99	−15.09
3	−16.41	−16.46	−16.21	−16.22

5.3.3 Triangular Flat-Top Pattern Synthesis for a 12×12 Circular Patch Antenna Cylindrical Array

Finally, the developed method is utilized to synthesize a more complicated pattern with a triangular flat-top shaped beam for a cylindrical array of 12×12 elements. A circular microstrip patch antenna with a radius of 3.72 mm working at 10 GHz is utilized as the array element. The FR4 substrate is used, and the dielectric constant is $\epsilon_r = 4.4$ with a thickness of 1.50 mm. Suppose the elements are distributed around a cylindrical surface with a radius of 101 mm. The element spacing is 0.5λ in both circumferential directions (the angular interval is 8.5°) and generatrix direction. $\vec{p}_d = \vec{y}$ is set for the desired polarization. Then, the CoP $\vec{p}_{co}$ and the XP $\vec{p}_X$ can be calculated according to the definitions (4.11) and (4.12), respectively. Suppose the shaped beam region is chosen as $\{(u,v); |0.08 \le u \le 0.6 \& -0.1 \le v \le 0.4 \& u+v \le 0.5\}$, where $u = \sin\theta\cos\phi$ and $v = \sin\theta\sin\phi$. $\Gamma_{SLL} = \Gamma_{XPL} = -11$ dB are set for the desired SLL and XPL. In the PSO, parameters used are the same as those in the first example, except that the population size is $N_p = 288$.

The synthesized patterns as well as the full-wave simulated real ones obtained in the initial and the 3^{rd} refining step are given in Fig. 5.11. As can be seen, in the initial step ($k = 0$), the real pattern performance is much worse than that of the synthesized pattern due to the neglect of the mutual coupling variation and antenna deformation. The SLLs and XPLs of the real CoP and XP patterns are only −7.5 dB and −5.8 dB, respectively, which are much higher than −10.91 dB and −10.78 dB of the synthesized patterns.

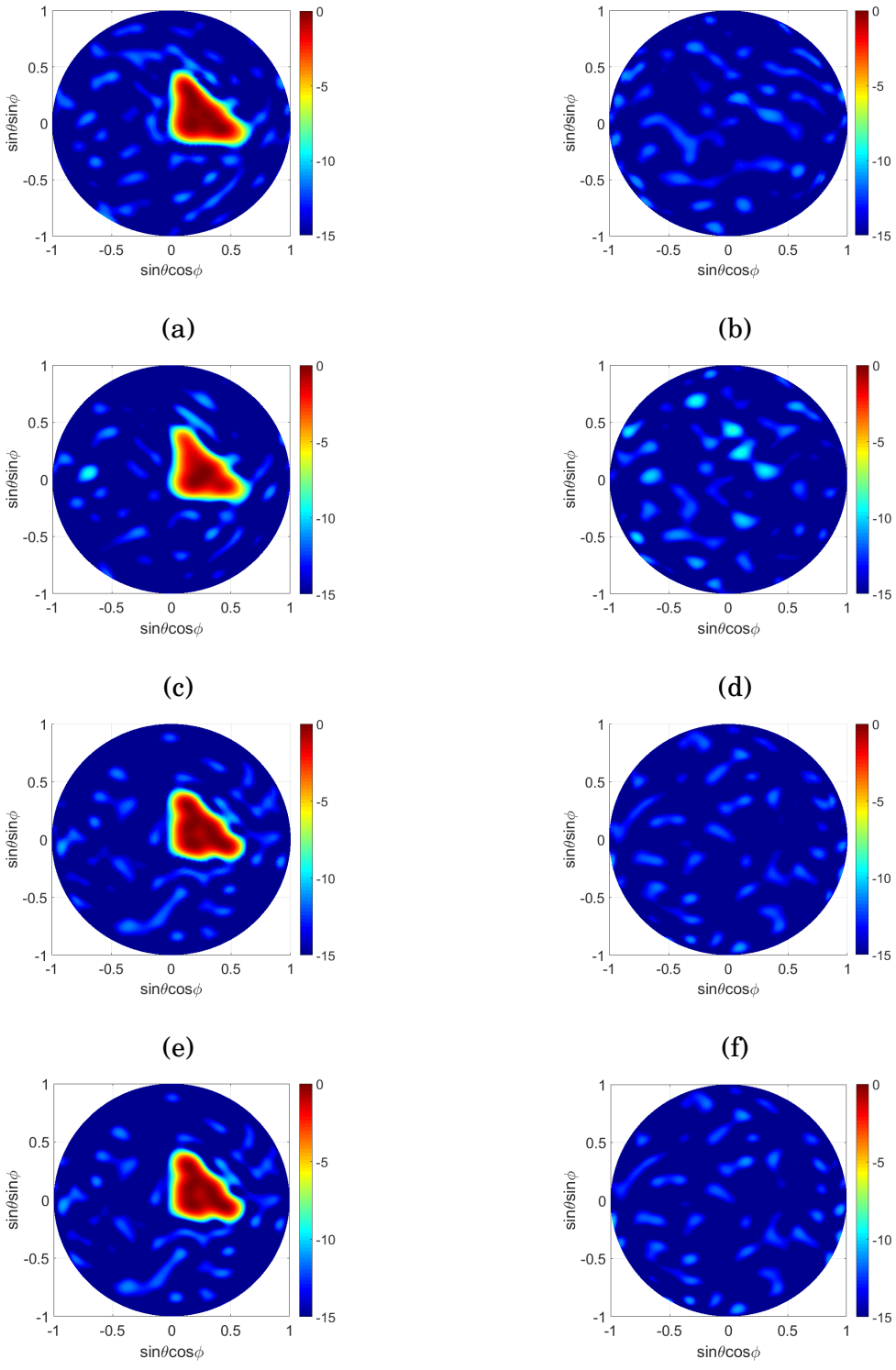

Figure 5.11: Top views of the synthesized and HFSS simulated real triangular flat-top shaped patterns. (a), (b) show the synthesized, and (c), (d) show the real CoP and XP patterns at the initial step; (e), (f) show the synthesized, and (g), (h) show the real CoP and XP patterns at 3^{rd} refining step.

Table 5.4: THE MAXIMUM SLLS AND XPLS OF THE SYNTHESIZED AND REAL PATTERNS FOR DIFFERENT kS IN EXAMPLE 3.

k^{th}	Synthesized Results (dB)		Simulated Results (dB)	
	SLL	XPL	SLL	XPL
0	−10.91	−10.78	−7.50	−5.80
1	−10.74	−10.92	−9.10	−8.83
2	−10.73	−10.62	−10.32	−9.70
3	−10.64	−10.63	−10.58	−10.23

Nevertheless, after employing three successive refining steps, the real patterns highly resemble the synthesis ones. The real SLL and XPL are −10.58 dB and −10.23 dB in the 3^{rd} refining step, which are 3.08 dB and 4.43 dB better than the corresponding values obtained in the initial step. The obtained results for this 12×12-element cylindrical conformal array have further demonstrated the effectiveness of the developed element rotation based method. The synthesized and real SLLs and XPLs at the four steps are given in Table 5.4.

The obtained element-rotated cylindrical conformal array is shown in Fig. 5.12. It is noteworthy that the antennas are rotated with respect to their feeding pins. As a result, this rotation causes phase center shift of each antenna, as the phase center is located at the center of the circular patch. However, the phase center change is relatively small as the distance between the feeding pin and the circular patch center is only 0.09λ at the center frequency of $f = 10$ GHz. Although the change in phase center introduces certain errors to the element pattern approximation, the proposed refined method can effectively reduce the errors by successively decreasing the rotation angles with several refining steps. In the last refining step, the maximum phase center shift is only 0.0052λ for a maximum rotation angle of 3.3°. This minimal phase center shift has negligible impact on the element pattern, ensuring that the approximation remains highly accurate.

In this example, it takes about 4.85 hours for one-time PSO-based rotation and phase optimization and 6.73 hours for one-time HFSS simulation of the element rotated array. Thus, the total time cost of the developed method is about 46.32 hours. Besides, the

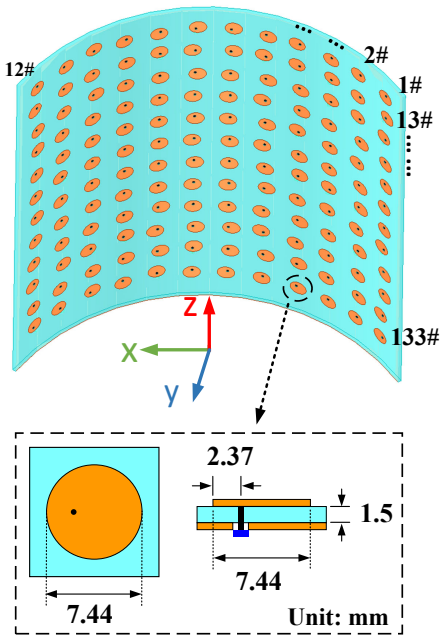

Figure 5.12: The obtained element-rotated cylindrical array with a closed view of the adopted circular patch antenna.

memory occupied by the PSO-based optimization and full-wave simulation are 146.8 MB and 135 GB, respectively.

5.4 Fabrication and Measurement

The obtained cylindrical conformal array with 24 rotated U-slot loaded patch antennas is fabricated. A 24-way power division network is designed to provide the optimized excitation phases with equal amplitudes. Similar to the fabricated linear array in Chapter 4, a Wilkinson power divider is designed here to provide equal excitation amplitudes but unequal excitation phases for the shaped pattern. The designed Wilkinson power divider includes one input port for connection to the feeding cables and 24 output ports for connection to the rotated antennas. These connections are made through 24 metal vias, which are insulated from the RF ground. To enhance isolation, 50 Ω resistors are incorporated between each pair of branched transmission lines. The excitation phases

required to achieve the desired flat-top shaped pattern are accomplished by including phase shifting lines of different lengths in the designed Wilkinson power divider.

The Wilkinson power divider and the rotated antennas are fabricated on two separate flat substrates. Both substrates have the same thickness of 0.508 mm and dielectric constant of $\epsilon_r = 2.2$, but different sizes. The power division network and the ground plane are fabricated on the two sides of one substrate with a size of 519 mm × 146 mm. The other substrate has a size of 469 mm × 58 mm with the rotated antenna elements fabricated on one side and nothing on the opposite side. These two substrates are thin and can be easily bent and fixed to a cylinder-shaped support structure (3D-printed using photosensitive resin material, $\epsilon_r = 3.5$) using dielectric screws. Finally, 24 feeding probes are used to connect the output ports of the power division network and the corresponding rotated elements. The fabricated and assembled cylindrical conformal array and its picture under test are shown in Fig. 5.13.

The prototype is measured using the NSI far-field measurement system, and the measured array patterns, as well as the HFSS simulated ones, are shown in Fig. 5.14. It should be noted that the simulated patterns in Fig. 5.14 are obtained by simulating the element-rotated antenna array fed by a Wilkinson power division network, and therefore, they differ slightly from the simulated patterns in Fig. 5.7(d), which are obtained by feeding every element with a coaxial port in the HFSS. The measured SLL is −13.43 dB, whilst the XPL is −13.11 dB. These values are around 0.93 dB and 0.45 dB worse than the simulation ones. The measured CoP main lobe ripple is about ±1.3 dB, which is slightly larger than the ±0.85 dB obtained in the full-wave simulation. Despite the slight degradation in performance due to fabrication and assembly errors, the measured patterns show good agreement with the simulated ones.

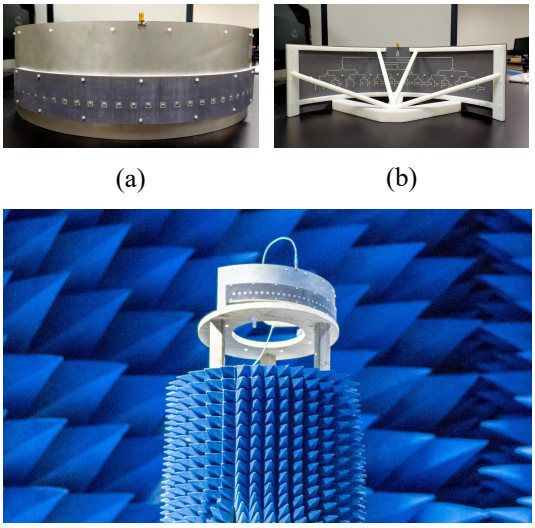

(a) (b)

(c)

Figure 5.13: Photos of the fabricated cylindrical array of rotated U-slot antennas as well as the photo of this array under test.

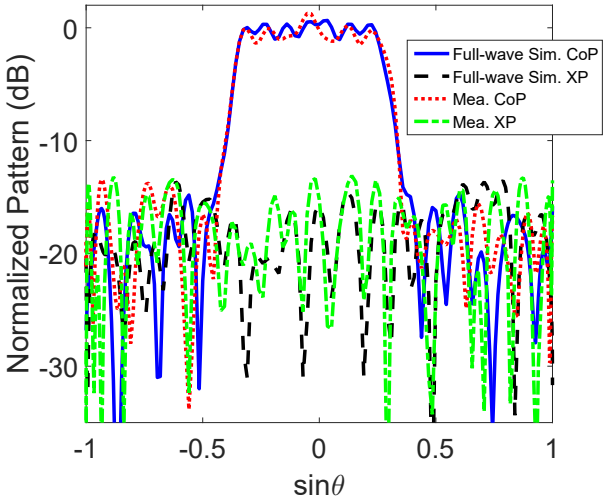

Figure 5.14: The full-wave simulated and measured CoP and XP patterns for the cylindrical array of 24 rotated U-slot antennas integrated with a equal-power feeding network.

5.5 Summary

In summary, this chapter presents a novel method for shaped-beam conformal array synthesis using the element rotation technique. The challenges in this type of array

synthesis are addressed, including the effect of element rotation on mutual coupling and antenna deformation, as well as the need for complicated transformations and interpolations. The effectiveness of the developed method is demonstrated through three representative examples, which also show its superiority over phase-only and amplitude/phase methods. Finally, measurements of the fabricated prototype validate the synthesized results. Overall, this method presents a valuable contribution to the field of conformal array synthesis.

For the first time in the literature, this work has both theoretically and experimentally validated that element rotation can serve as an equivalent amplitude weighting for improving the shaped-beam conformal array synthesis performance. With the developed method, complicated shaped patterns can be obtained by just optimizing the element rotations and phases, and no amplitude weighting is required, thus saving many unequal power dividers in the feeding network.

CHAPTER 6

EFFICIENT AND ACCURATE PHASE-ONLY MULTI-BEAM SYNTHESIS USING THE PARTITIONED ITERATIVE FFT

6.1 Introduction

As a key technology for the fifth-generation (5G) and sixth-generation (6G) wireless communication networks, multi-beam antennas with flexibly steerable beams have drawn increased attention these years. In Chapter 2, the state-of-the-art studies regarding the dual- and multi-beam pattern synthesis methods have been reviewed. It was shown that the existing dual- and multi-beam pattern synthesis methods prefer employing excitation amplitude and phase modulation to achieve favorable results. Despite their outstanding performance, nonuniform excitation amplitudes will inevitably result in complicated feeding networks and low aperture efficiency. Although a few phase-only methods were developed to avoid nonuniform excitation amplitudes, they were either time-consuming or unable to achieve good enough pattern performance regarding the peak directions, peak powers, as well as sidelobe levels (SLLs). An accurate and efficient

method is highly desired.

In this chapter, a partitioned iterative Fourier transform (PIFT) technique is developed to efficiently synthesize dual- and multi-beam patterns by optimizing the excitation phases only. To achieve accurate beam directions, a partitioned beam calibration strategy learned from the Schelkunoff unit circle is incorporated in the PIFT to successively calibrate the multiple beams. This partitioned calibration strategy can partition the multi-beam pattern into single-beam patterns, which can then be calibrated separately by applying additional peak-deviation-related phase terms to their excitations. Such a partition and calibration method can accurately shift the beams to their anticipated directions without affecting each other. Besides, main lobes of the multi-beam pattern are iteratively corrected to achieve desired peak powers, and the sidelobes are also iteratively modified to achieve relatively low SLL. Moreover, element patterns as well as quantized excitation phases can be considered in the PIFT method with proper extension. Several numerical examples of synthesizing dual- and multi-beam patterns are presented. Full-wave simulation and comparisons with other phase-only methods are presented to comprehensively evaluate the developed PIFT method.

This chapter is organized as follows. Formulation and algorithm are discussed in Section 6.2. Section 6.3 presents some numerical results. Section 6.4 draws the summary.

6.2 Formulations and Optimization Algorithm

6.2.1 Analytical Excitations to Generate Multi-Beam Patterns

Suppose there is a linear array with N isotropic elements located on z-axis with uniform intervals of d. The array pattern is obtained with (2.1) and simplified as:

$$F(\mathbf{w};\theta) = \sum_{n=0}^{N-1} w_n e^{j\beta r_n \cos\theta} \tag{6.1}$$

where $j = \sqrt{-1}$, $\beta = 2\pi/\lambda$, λ is wavelength. $r_n = nd$ is the n^{th} element position. $\mathbf{w} = [w_0, w_1, ..., w_{N-1}]^T$ is the excitation vector, where $[\cdot]^T$ denotes transpose of a matrix.

Suppose an L-beam pattern with L main lobe peaks whose directions are at θ_l ($l = 1, 2, ..., L$) is desired. To obtain it, one can directly calculate the excitations with an analytical expression. As is known, a multi-beam pattern can be obtained by summing multiple single-beam patterns as:

$$F(\mathbf{w};\theta) = \sum_{l=1}^{L} F_l(\mathbf{w}_l;\theta) = \sum_{l=1}^{L}\sum_{n=0}^{N-1} w_n^{(l)} e^{j\beta r_n \cos\theta} = \sum_{n=0}^{N-1}\Big(\sum_{l=1}^{L} w_n^{(l)}\Big) e^{j\beta r_n \cos\theta} \tag{6.2}$$

where $w_n^{(l)} = e^{-j\beta r_n \cos\theta_l}$. As can be learned from (6.2), a multi-beam pattern excitation vector can be obtained by summing multiple single-beam pattern excitation vectors as:

$$\mathbf{w} = \sum_{l=1}^{L} \mathbf{w}_l = \Big[\sum_{l=1}^{L} w_1^{(l)}, \sum_{l=1}^{L} w_2^{(l)}, ..., \sum_{l=1}^{L} w_{N-1}^{(l)}\Big]^T \tag{6.3}$$

However, though a multi-beam pattern can be yielded, the excitations obtained with (6.3) have nonuniform amplitudes, and the amplitude dynamic range ratio could be considerably large. As an example, a dual-beam pattern whose peaks are at $\theta_1 = 30°$ and $\theta_2 = 80°$ is designed with (6.3) for a 20-element $\lambda/2$-spaced linear array. The pattern is shown in Fig. 6.1(a) and the corresponding excitation amplitudes are shown in Fig. 6.1(b). One can see that the excitation amplitudes fluctuate severely. Such fluctuated amplitudes will not only lead to a complicated feeding network but also result in a low aperture efficiency. Instead, it would be much more desirable to achieve multi-beam patterns with uniform excitation amplitudes.

A straightforward method to obtain a uniform-amplitude excitation vector that can yield a multi-beam pattern is directly extracting a phase vector from (6.3) as:

$$\mathbf{w}_p = e^{j*\arg\left[\sum_{l=1}^{L} \mathbf{w}_l\right]} \tag{6.4}$$

where arg[·] denotes argument of a complex number, the subscript p denotes phase vector. However, (6.4) generally cannot yield good results since the phase extracting can cause

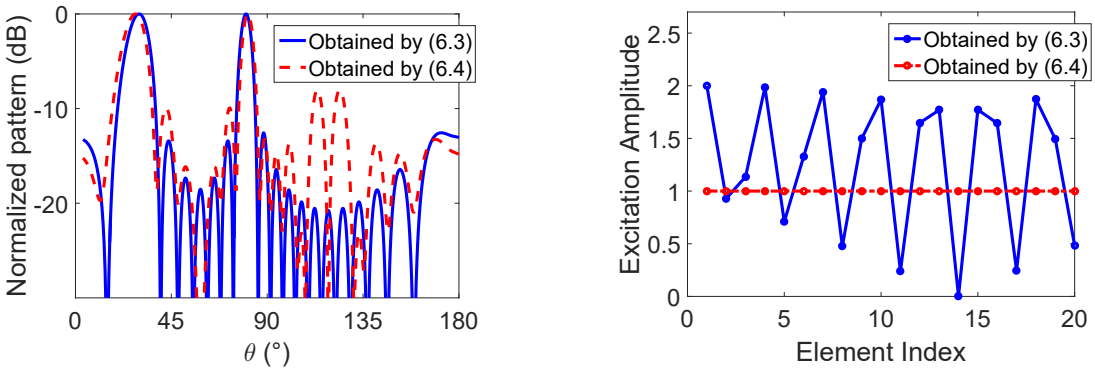

(a) (b)

Figure 6.1: Dual-beam patterns designed with nonuniform-amplitude excitation vector (6.3) and uniform-amplitude excitation vector (6.4), and their excitation amplitudes for a linear array of 20 elements. (a) the dual-beam patterns and (b) the excitation amplitudes.

severe peak power decrease, beam direction deviation, and SLL increase. As an example, the 20-element linear array is considered to design a dual-beam pattern with (6.4). The obtained pattern is shown in Fig. 6.1(a). The excitation amplitudes are uniform, as shown in Fig. 6.1(b). One can see that the dual peaks deviate from the desired angles, and the SLL is up to −8.01 dB. Thus, an optimization method that can efficiently optimize the excitation phases to obtain multi-beam patterns with accurate beams and reduced SLLs is much preferable.

6.2.2 Multi-Beam Pattern Synthesis with Accurate Beam Control Using the Partitioned Iterative Fourier Transform

As is known, the array factor (6.1) has a similar expression as the Fourier transform. By sampling $\cos\theta$ as $\cos\theta = q\Delta = q\lambda/(Qd)$, where $q = -Q/2, -Q/2+1, \ldots, Q/2-1$, Q being the number of sampling points, (6.1) can be rewritten as:

$$F(\mathbf{w}; q\Delta) = \sum_{n=0}^{N-1} w_n e^{jn2\pi q/Q} \tag{6.5}$$

As is seen, (6.5) forms a Fourier transform relationship between $\{F(\mathbf{w}; q\Delta)\}$ and $\mathbf{w}$. This relationship has been exploited to develop an iterative Fourier transform (IFT) array

synthesis method [110], where the fast Fourier transform (FFT) and inverse FFT (IFFT) are iteratively applied to synthesize desired patterns. The IFT has proven to be one of the most efficient iterative methods and has been widely employed in array synthesis [16, 111–113].

Naturally, the IFT can serve as a potential candidate to efficiently synthesize multi-beam patterns by optimizing the excitation phases only. However, when one applies the conventional IFT-based phase-only method to synthesize a multi-beam pattern, the main lobe peaks might deviate from the desired angles since it lacks accurate control of the multiple peak directions. One cannot just simply shift the beams to the right directions by applying an additional phase term to the original excitation since it will shift all the beams to the same direction with identical distances (as observed in u-space, $u = \cos\theta$), which is not desired in most cases. Furthermore, the conventional IFT does not have a precise strategy to control the peak powers of all the multiple beams.

A PIFT technique is developed here to synthesize multi-beam patterns with accurate beam control. The PIFT incorporates a partitioned calibration strategy in each iteration of the IFT to successively calibrate the multiple beams. The partitioned calibration strategy, which is developed according to the Schelkunoff's unit circle, can partition the multi-beam pattern into single-beam patterns and calibrate their peaks separately by applying additional peak-deviation-related phase terms to their excitations. According to the Schelkunoff's unit circle method [4], (6.5) can be rewritten as:

$$F(\mathbf{w}; q\Delta) = \sum_{n=0}^{N-1} w_n z^n \tag{6.6}$$

where $z = e^{j2\pi q/Q}$. Since (6.6) is of order $(N-1)$, it has $(N-1)$ roots and can be rewritten as:

$$F(\mathbf{w}; q\Delta) = w_{N-1}(z - z_1)(z - z_2)...(z - z_{N-1}) \tag{6.7}$$

where z_n $(n = 1, 2, ..., N-1)$ are complex roots or zeros of (6.6). (6.7) indicates that the amplitude of the array factor, as observed from any point z on the unit circle in the

complex plane, is the product of the lengths of the straight segments joining that point to the n^{th} ($n = 1,2,...,N-1$) zeros [3]. For a multi-beam pattern, when the zeros nearby beam l are moved, which is equivalent to changing beam l, other beams at the far side will not be affected much. That is because, as observed from point z at far beams, movement of the zero z_n nearby beam l will not change $(z - z_n)$ much, so that (6.7) would not change much. Based on this principle, it is feasible to partition a multi-beam pattern into multiple single-beam patterns and calibrate them individually. In this way, when modifying the excitation phases of one partitioned single-beam pattern for beam direction calibration, only the zeros as well as the main lobe of this pattern will be shifted, whereas other beams will be hardly affected. After calibration of all the single-beam patterns, a calibrated multi-beam pattern can be obtained through direct summation of the updated single-beam pattern excitations.

Thus, an array pattern $F(\theta)$ with L deviated beams pointing to θ'_l ($l = 1,2,...,L$) can be partitioned into L single-beam patterns $F'_l(\theta)$ ($l = 1,2,...,L$) at first. Then, their excitation vectors $\mathbf{w}'_l$ can be obtained by applying FFT, and the peak directions can be calibrated as [114]:

$$\mathbf{w}_l = \mathbf{w}'_l \odot e^{-j\beta\mathbf{r}(\cos\theta_l - \cos\theta'_l)} \tag{6.8}$$

where $\odot$ is the Hadamard product of two matrices with the same dimension, $\mathbf{r} = [r_1, r_2, ..., r_{N-1}]^T$ denotes the element location vector. At last, the multi-beam pattern with calibrated beams can be obtained by applying IFFT to the summation of all the calibrated single-beam excitations $e^{j*\arg[\sum_{l=1}^{L}\mathbf{w}_l]}$. An example is given to demonstrate the developed PIFT-based calibration method. Suppose there is a dual-beam pattern $F(\theta)$ with deviated peak directions $\theta'_1 = 60°$ and $\theta'_2 = 90°$, which can be designed by (6.3), as shown in Fig. 6.2(a). The corresponding excitation phases are shown in Fig. 6.2(b). Assume the desired beam directions are $\theta_1 = 50°$ and $\theta_2 = 100°$. $F(\theta)$ can be directly partitioned into two single-beam patterns $F'_1(\theta)$ and $F'_2(\theta)$ from the middle of the dual

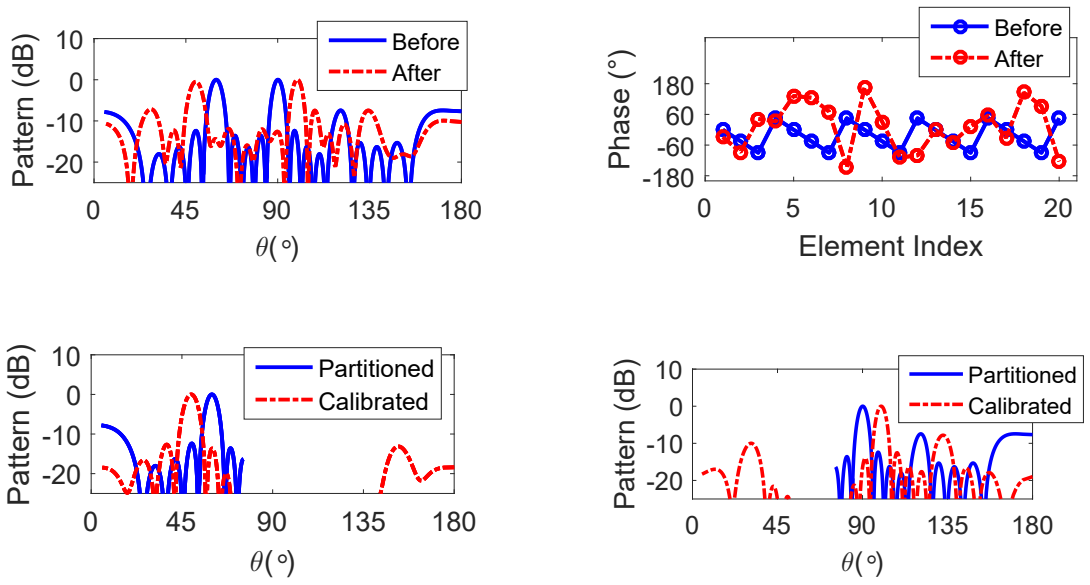

(c) (d)

Figure 6.2: Dual-beam pattern calibration with the developed PIFT-based calibration strategy: (a) dual-beam patterns and (b) excitation phases before and after calibration; (c) and (d) partitioned and calibrated single-beam patterns.

beams, as is seen Fig. 6.2(c) and (d). The excitation vectors can be obtained by applying FFT to $F_1'(\theta)$ and $F_2'(\theta)$, and then, they can be calibrated using (6.8). The calibrated patterns are shown in Fig. 6.2(c) and (d). At last, by applying IFFT to the summation of the two calibrated single-beam excitations, the calibrated dual-beam pattern can be obtained, as shown in Fig. 6.2(a). As can be seen, the beams are precisely adjusted from the original directions to the anticipated directions, which has validated the PIFT-based calibration strategy.

Except for the beam calibration, the multi-beam pattern is also iteratively modified to correct the peak powers and reduce the SLL in the PIFT-based phase-only method. The peak power calibration and SLL reduction are described in detail below.

(i) ***Peak Power Calibration***: Suppose the main lobe regions where the peaks θ_l ($l = 1,2,...,L$) locate are denoted by Θ_l^{ML}. To precisely control the main lobe peak powers,

the main lobes are corrected to have the desired powers as:

$$F'(\theta) = \frac{\Gamma_P^{(l)} F(\theta)}{|F(\theta_l)|}, \text{for } \theta \in \Theta_l^{ML},\ l = 1,2,...,L. \tag{6.9}$$

where $\Gamma_P^{(l)}$ is the desired peak power of the n^{th} beam.

(ii) ***Sidelobe Reduction****:* Suppose the sidelobe region and the desired SLL are denoted by Θ_{SL} and Γ_{SLL}, respectively, the sidelobes can be modified as:

$$F'(\theta) = \begin{cases} \left(\frac{2\Gamma_{SLL}}{|F(\theta)|} - 1\right) F(\theta), & \text{if } |F(\theta)| > \Gamma_{SLL} \\ F(\theta), & \text{if } |F(\theta)| \le \Gamma_{SLL} \end{cases} \tag{6.10}$$

where $\theta \in \Theta_{SL}$. In the above, the more the SLL exceeds Γ_{SLL}, the more it is reduced.

6.2.3 The Proposed Phase-only Multi-Beam Pattern Synthesis Procedure

Like the traditional IFT, the performance of the PIFT is actually dependent, to some extent, on the initial solution. Naturally, if multiple times of PIFT-based phase-only optimizations can be conducted with different initial excitations, the performance of the finally optimized multi-beam pattern can be improved. Here, to generate multiple initial solutions, a random phase parameter ϕ_l is introduced to equation (6.4) to yield a more generalized version as:

$$\mathbf{w}_p = e^{j * \arg[\mathbf{w}_1 + \sum_{l=2}^{L} \mathbf{w}_l e^{j\phi_l}]} \tag{6.11}$$

where $\phi_l \in [0, 2\pi]$ $(l = 2,3,...,L)$.

The detailed procedure of synthesizing multi-beam patterns with the developed PIFT-based phase-only method is summarized in **Algorithm 5**. In **Algorithm 5**, the excitation phase vector obtained at each iteration is saved, and the final solution is the one with the lowest SLL under the circumstance of satisfying given main lobe constraints. Main lobe examination is necessary since even though they are iteratively calibrated and corrected, they still have a chance to deteriorate due to the direct phase extraction in the PIFT.

The PIFT-based phase-only method is also applicable to the multi-beam planar array synthesis with proper modification. For a $M \times N$-element planar array with uniform distances of d, its pattern can be readily obtained [110]. By sampling $u = \sin\theta\cos\phi$ and $v = \sin\theta\cos\phi$ as $u = p\Delta_p = p\lambda/(Pd)$, $v = q\Delta_q = q\lambda/(Qd)$, where P and Q are the sampling point number, the array pattern can be rewritten as:

$$F(\mathbf{w}; p\Delta_p, q\Delta_q) = \sum_{m=0}^{M-1}\sum_{n=0}^{N-1} w_{mn} e^{j2\pi(mp/P+nq/Q)} \tag{6.12}$$

With (6.12), a 2D-PIFT can be developed to synthesize multi-beam patterns with accurate beam control for planar arrays. The synthesis process is similar to **Algorithm 5**, and the only difference is the beam calibration. For the planar array, the beam calibration (6.8) becomes:

$$\mathbf{w}_l = \mathbf{w}'_l \odot e^{-j\beta[\mathbf{r}_x(u_l-u'_l)+\mathbf{r}_y(v_l-v'_l)]} \tag{6.13}$$

where (u_l, v_l) and (u'_l, v'_l) are the desired and actual beam directions of the l^{th} beam, $\mathbf{r}_x$ and $\mathbf{r}_y$ are position vectors of the elements.

The PIFT method can consider actual element patterns. For simplicity, the element pattern obtained by full-wave simulating the antenna in an array environment is used for all elements. Though error will be introduced to the synthesized results, the error is actually limited, especially for large arrays where the edge effect has a slight influence. When considering the element pattern, there is slight difference in the synthesis procedure **Algorithm 5**: each time after applying IFFT to the excitation vector, the element pattern is multiplied to calculate the array pattern; when calculating the excitation vector, the array pattern is divided by the element pattern and then applying the FFT.

Besides, the PIFT method is also capable of optimizing discrete excitation phases. The quantization strategy developed in [115] is iteratively integrated into the PIFT method to obtain a quantized PIFT (Q-PIFT) method. In the Q-PIFT, the n^{th} excitation phase is quantized as:

$$\varphi'_n = R[(\varphi_n + \delta_n)/\Delta_\varphi]\Delta_\varphi - R[\delta_n/\Delta_\varphi]\Delta_\varphi \tag{6.14}$$

Algorithm 5 The developed PIFT-based phase-only multi-beam pattern synthesis procedure.

1: Input the element number N, desired peak directions θ_l and their peak powers $\Gamma_P^{(l)}$ ($l = 1,2,...,L-1$), desired SLL Γ_{SLL}, the number of sampling points Q, the number of initial excitations K and the number of iterations I_m.
2: Initialize K excitation phase vectors $\mathbf{w}_k^{(0)}$ ($k = 1,2,...,K$) with (6.11) by choosing different values of ϕ_l.
3: Set $k = 1$.
4: Set $i = 1$, $\mathbf{w}^{(i)} = \mathbf{w}_k^{(0)}$.
5: Apply IFFT to $\mathbf{w}^{(i)}$ to obtain a multi-beam pattern $F^{(i)}(\theta)$, and partition it into L single-beam patterns $F_l'(\theta)$ ($l = 1,2,...,L$).
6: Apply FFT to each single-beam pattern $F_l'(\theta)$ to obtain the corresponding excitation vectors $\mathbf{w}_l'$.
7: Modify $\mathbf{w}_l'$ with (6.8) to obtain $\mathbf{w}_l$ for beam calibration.
8: Update $\mathbf{w}^{(i)} = \sum_{l=1}^{L} \mathbf{w}_l$, and apply IFFT to obtain an updated multi-beam pattern $F^{(i)}(\theta)$ with calibrated beams.
9: Peak power calibration and sidelobe reduction: if $F^{(i)}(\theta_l)$ do not equal $\Gamma_P^{(l)}$, calibrate the peak power with (6.9); if the SLL exceeds Γ_{SLL}, reduce the SLL with (6.10).
10: Apply FFT to the modified $F^{(i)}(\theta)$ to obtain an updated excitation vector $\mathbf{w}^{(i)}$.
11: Extract the phase vector $\mathbf{w}_p^{(i)} = e^{j*\arg[\mathbf{w}^{(i)}]}$;
12: Save $\mathbf{w}_p^{(i)}$, set $i = i+1$, $\mathbf{w}^{(i)} = \mathbf{w}_p^{(i-1)}$, and loop to Step 5 until $i = I_m$.
13: Set $k = k+1$ and loop to Step 4 until $k = K$.
14: Output the best excitation phase vector, which yields a multi-beam pattern with the lowest SLL meanwhile meets the main lobe requirements.

where $R[\cdot]$ is the nearest integer function, $\varphi_n = \arg[w_n]$, δ_n is the random phase offset, and Δ_φ is the quantization bit of the discrete phase shifter [115]. The synthesis procedure of the Q-PIFT is similar to **Algorithm 5** except that two quantization operations based on the above equation are added after Step 2 and 11.

6.3 Synthesis results

In this section, dual- and multi-beam pattern synthesis examples are presented for demonstration of the developed PIFT-based phase-only method. Comparisons with other improved methods are also included. All the examples are conducted on a workstation with an Intel Xeon 6248 CPU at 2.50 GHz.

6.3.1 Phase-Only Dual-Beam Pattern Synthesis for Linear Arrays

The PIFT-based phase-only method is employed to synthesize dual-beam patterns for linear arrays at first. Before that, the initial excitation number K and iteration number I_m of the PIFT are studied with a 192-element array for the synthesis of an equal-power dual-beam pattern with beam directions of $\theta_1 = 60°$ and $\theta_2 = 130°$. The evaluation criterion of the pattern is the peak SLL under the condition of satisfying the main lobe constraints (with accurate beam direction and the peak power deviation < 0.1 dB). In the study, the desired SLL is set as $\Gamma_{SLL} = -18$ dB, whilst Q is set as $Q = 2048$. K is set as 1, 10, 20, and 30, whilst I_m varies from 50 to 250 at 50 interval. For different K and I_m, 10 times of the PIFT are conducted to obtain an average SLL. The obtained SLLs for different K and I_m are shown in Fig. 6.3. As can be seen, the SLLs generally decrease with the increase of K and I_m. Nevertheless, when I_m increases from 150 to 250, the SLL decrease is very limited (smaller than 0.1 dB). Similarly, when K increases from 20 to 30, the SLL decrease is smaller than 0.1 dB. Thus, $K = 20$ and $I_m = 150$ are reasonable choices, and further increase of K and I_m is not necessary.

Then, the developed PIFT is utilized to synthesize equal-power dual-beam pattern linear arrays with 24, 48, 96, and 192 elements, respectively. For the four arrays, the dual beam peak directions are set as $\theta_1 = 60°$ and $\theta_2 = 130°$. As a comparison, the conventional IFT and two other phase-only methods in the literature, namely the single co-ordinate method (SCM) developed in [116] and the sequential quadratic programming (SQP) in [74], are also utilized for the same dual-beam pattern synthesis. Note that since the SLL performance was originally not considered in [74], here the SLL constraint is included in the SQP for comparison purpose. Both the SCM and the SQP are initialized with their best parameters, and they are used to obtain their best achievable SLL performance under the circumstance of not affecting the main beams.

The pattern performances and time costs achieved by the four methods are listed in

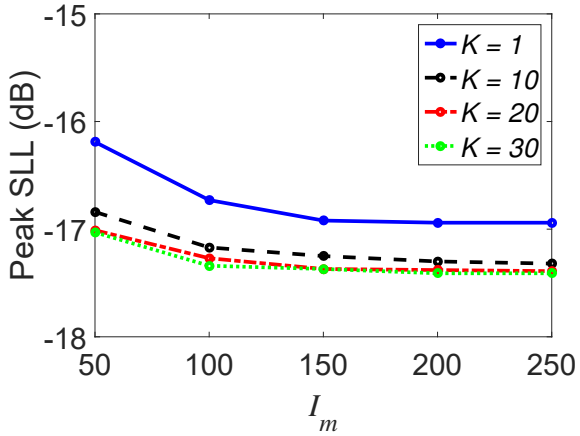

Figure 6.3: The peak SLLs obtained in the study of K and I_m for a 48-element linear array.

Table 6.1. One can see that the conventional IFT is the fastest method, and the SCM is slightly slower. However, despite their high efficiency, they both have poor performance in SLL reduction and beam direction control. The beam direction deviations obtained by these two methods are up to 0.9° and 0.6°, respectively. The SQP, on the other hand, can achieve the lowest SLLs among the four methods. The SLL is about −18.54 dB when $N = 192$. It is 3.96 dB lower than that obtained by the SCM. However, it generally cannot achieve very accurate control of the beam directions and peak powers. Moreover, it is the most time-consuming method. The time cost is 469.28 seconds when $N = 192$, which is more than 1000 times slower than the SCM.

For the developed PIFT-based method, the obtained dual beams are all exactly directed in the anticipated directions. Compared to the IFT, the beam direction improvement achieved by the PIFT is 0.4° for the 192-element array. Though 0.4° looks small, it actually corresponds to 50% of the half-power beamwidth (HPBW). It means that the conventional IFT actually leads to a gain decrease of around 3 dB. By contrast, the improvement achieved by the PIFT is prominent. Besides, the obtained peak power deviations are smaller than 0.03 dB. Furthermore, the obtained SLLs are −12.50 dB and −14.14 dB when $N = 24$ and $N = 48$, which are comparable to those obtained by

Table 6.1: The SLLs, Actual Beams Directions, Peak Power Deviations, and Time Costs Achieved in the Phase-Only Dual-Beam Pattern Synthesis for Different Linear Arrays Using the IFT, the SCM, the SQP, and the developed PIFT-Based Method

	SLL (dB)				Actual Beam Directions (°)				Power Deviation (dB)				Time Cost (Seconds)			
N	IFT	SCM	SQP	PIFT	IFT	SCM	SQP	PIFT	IFT	SCM	SQP	PIFT	IFT	SCM	SQP	PIFT
24	−11.62	−9.98	−12.52	−12.50	60.6/130.3	60.3/129.1	60.2/130.3	60/130	0.53	0.10	0.12	0.03	0.03	0.04	25.69	1.32
48	−13.56	−10.83	−14.29	−14.14	60.5/129.5	60.6/129.4	60.2/129.6	60/130	0.58	0.05	0.13	0.01	0.04	0.08	105.21	1.65
96	−15.05	−13.76	−16.91	−16.02	60.3/130.6	60.3/129.5	60/130	60/130	0.62	0.01	0.14	0.03	0.05	0.17	251.30	2.11
192	−16.41	−15.59	−18.54	−17.22	59.8/130.4	60.5/129.4	60/130	60/130	0.47	0.09	0.01	0.01	0.08	0.43	469.28	2.62

the SQP, though the values are a little worse when N increases to 96 and 192. But the developed method is much faster than the SQP, and only 2.62 seconds are required for the 192-element array.

In addition, for a more comprehensive comparison, Table 6.2 provides the computational complexity and memory usage of the four methods in the synthesis of the 24-element linear array. As can be seen, among the four methods, the SQP and the proposed PIFT methods feature higher computational complexity than the IFT and SCM methods. On the other hand, the IFT outperforms the rest three methods in terms of memory usage during the optimization. The proposed PIFT method occupied slightly larger memory than the IFT and SCM methods. In summary, the PIFT method emerges as the preferred choice among the four methods. It demonstrates efficient performance in achieving dual-beam patterns with the most accurate beam direction and power control, and relatively low SLL. Although it requires relatively larger memory usage compared to other methods, the overall benefits and improved performance make it the preferred method for dual-beam pattern synthesis. The 48-element array patterns obtained by the four methods are provided in Fig. 6.4, and the corresponding excitation phases are provided in Table 6.3.

To further evaluate the developed PIFT method, another example considering beam scanning is presented here. A 48-element $\lambda/2$-spaced linear array is considered. Suppose one beam is fixed at $\theta_1 = 40^\circ$, while the other beam scans from $\theta_2 = 55^\circ$ to $\theta_2 = 150^\circ$ at an interval angle of 5°. The synthesized dual-beam patterns are shown in Fig. 6.5. It can be seen that, for all the scanning angles, the main beams are very accurately directed at the corresponding anticipated angles, with the peak power deviations smaller than 0.1 dB. The SLLs are ranging from -13.70 dB to -14.39 dB. The obtained results show the good capability and stability of the developed PIFT method in accurate beam control.

Table 6.2: PERFORMANCE COMPARISON BETWEEN THE PIFT METHOD AND THE REFERENCE METHODS FOR THE 24-ELEMENT LINEAR ARRAY EXAMPLE.

Method	IFT	SCM	SQP	PIFT
Computational Complexity	$O(I_m P \log P)$	$O(N^2)$	$O(N^{3.5}\log(\frac{1}{\eta}))$	$O(KI_m P \log P)$
Memory (MB)	1.1	2.3	56	6.3

η denotes a prefixed accuracy in the SQP method [117].

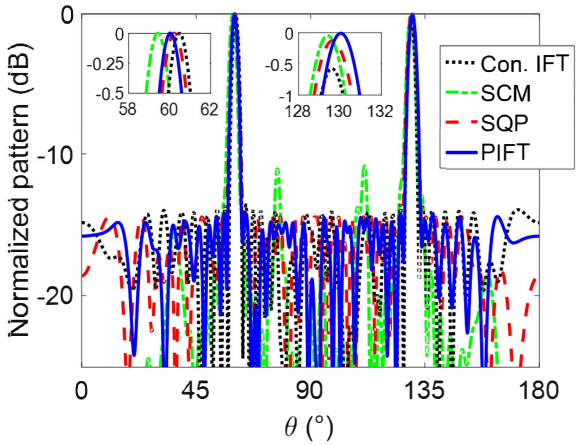

Figure 6.4: Dual-beam patterns obtained by conventional IFT, the SCM, the SQP, and the PIFT for a 48-element linear array.

6.3.2 Phase-Only Multi-Beam Pattern Synthesis for Planar Arrays

In this section, the PIFT is utilized to synthesize multi-beam patterns for planar arrays. A 15×15-element $\lambda/2$-spaced planar array is considered, and a microstrip antenna consisting of three staggered patches working at 5.2 GHz [118] is adopted as the element. For simplicity, element patterns of the array elements are assumed to be identical, and an embedded element pattern obtained by full-wave simulating this antenna in the array environment is utilized. Suppose an equal-power triple-beam pattern with the main beams directing at $(\theta, \phi) = (30°, 0°)$, $(30°, 90°)$, and $(30°, 180°)$ is desired. Firstly, a hybrid algorithm based on the genetic algorithm and modified IFT (HGAMIFT) technique [119] is employed to synthesize this pattern. Since the HGAMIFT method was

Table 6.3: THE EXCITATION PHASES OBTAINED BY THE PROPOSED METHOD FOR A 48-ELEMENT LINEAR ARRAY WITH A DUAL-BEAM PATTERN DIRECTING 60° AND 130° AS SHOWN IN FIG. 6.4.

n	1	2	3	4	5	6	7	8
Phases (°)	-2.9	155.9	169.7	139.3	6.0	-104.4	-112.3	80.8
n	9	10	11	12	13	14	15	16
Phases (°)	-6.7	-79.6	87.9	129.8	-47.0	-47.6	148.0	132.4
n	17	18	19	20	21	22	23	24
Phases (°)	8.6	-176.1	-144.4	45.8	66.8	-104.6	-94.9	91.7
n	25	26	27	28	29	30	31	32
Phases (°)	-106.6	-69.7	138.8	148.3	-22.6	-27.0	179.5	-7.9
n	33	34	35	36	37	38	39	40
Phases (°)	26.2	-108.7	-106.4	55.7	-28.9	-91.2	3.3	154.8
n	41	42	43	44	45	46	47	48
Phases (°)	-67.4	-8.1	161.3	-117.8	12.9	-156.8	-153.6	51.0

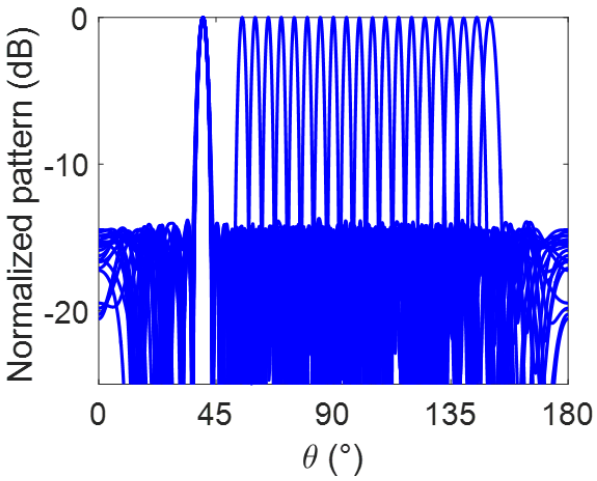

Figure 6.5: The synthesized dual-beam patterns with one beam directing in 40°, whilst the other beam scanning from 55° to 150° at an interval of 5°.

originally developed to synthesize thinned arrays, here it is adapted by abandoning the perturbation mechanism (used to decide the on-off status of the elements) to obtain an HGAIFT method for phase-only multi-beam pattern synthesis. Note that the HGAIFT inherits the dynamic control of the crossover and mutation rate of the GA and the control factor to determine the proportion of individuals from GA and modified IFT so that its search ability has not worsened. The synthesized triple-beam pattern is shown in Fig.

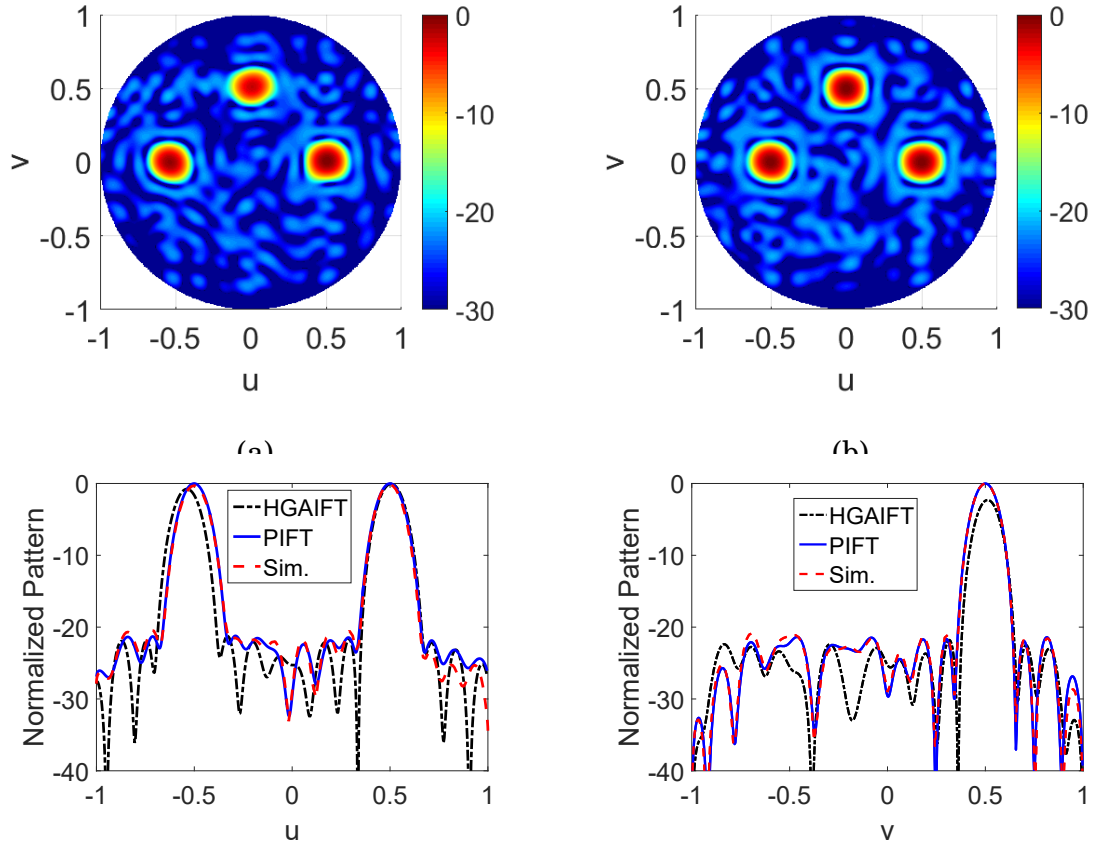

Figure 6.6: The synthesized and full-wave simulated triple-beam patterns for a 15×15-element planar array. (a) and (b) the 3D patterns synthesized by the HGAIFT and PIFT; (c) and (d) the $v = 0$ and $u = 0$ cut patterns obtained by the two methods and full-wave simulation using the HFSS.

6.6(a), and the $v = 0$ ($\phi = 0°$) and $u = 0$ ($\phi = 90°$) cut patterns are shown in Fig. 6.6(c) and 6.6(d), respectively. As can be seen, owing to the lack of accurate beam control, the beam direction is up to 2.6° (31% of the HPBW) deviated, and the peak power decrease is up to 2.27 dB. Besides, the SLL is about −20.81 dB.

Then, the developed PIFT method is employed to synthesize this triple-beam pattern with the same array. In the PIFT, the parameters are set as follows: $\Gamma_{SLL} = -22$ dB, $\Gamma_P^{(1)} = \Gamma_P^{(2)} = \Gamma_P^{(3)} = 0$ dB, $P = Q = 1024$, $K = 20$, $I_m = 200$. The synthesized triple-beam pattern is shown in Fig. 6.6(b), 6.6(c), and 6.6(d). As can be seen, the main lobe peaks

are exactly directed in the desired directions; meanwhile, the peak power deviations are smaller than 0.01 dB. The obtained SLL is −20.86 dB, which is comparable to that obtained by the HGAIFT. In addition, the planar array is full-wave simulated by using the high-frequency simulation software (HFSS). The array model is shown in Fig. 6.7(a). The PIFT-optimized excitation phases are utilized to excite the array. The full-wave simulated pattern at $v = 0$ ($\phi = 0°$) and $u = 0$ ($\phi = 90°$) cuts are given in Fig. 6.6(c) and 6.6(d). It can be seen that the simulated pattern also has very accurate beam directions, and it matches very well with the synthesized one despite a small peak power deviation (0.23 dB) and SLL increase (0.95 dB). The simulated realized gains of the three beams are 18.81 dBi, 18.67 dBi, and 18.52 dBi, respectively. The full-wave simulated results have validated the PIFT method in the accurate multi-beam pattern synthesis for practical antenna arrays.

As another example, a large planar array with 50×50 elements is considered to synthesize an unequal-power quad-beam pattern here. Suppose the desired beam directions are (θ, ϕ) = (0°, 0°), (15°, 0°), (35°, 0°), and (60°, 0°) with peak powers of 0 dB, −2 dB, −3 dB, and −4 dB, respectively. In the PIFT-based synthesis, we set $\Gamma_{SLL} = -29$ dB, and other parameters are used the same as before. The synthesized pattern at v = 0 ($\phi = 0°$) cut is shown in Fig. 6.8(a). As can be seen, the four beams are directed exactly in the desired directions with only 0.02 dB peak power deviation. The obtained SLL is −28.40 dB. The PIFT method only costs 3.56 minutes for this example, which has demonstrated its remarkable speed. The excitation phases obtained by the PIFT are shown in Fig. 6.8(b).

In addition, the Q-PIFT is utilized to synthesize this quad-beam pattern with discrete excitation phases here. Before that, direct quantization is applied as a comparison. Suppose a 4-bit phase shifter is targeted. The pattern obtained by directly quantifying the PIFT-optimized excitation phases is given in Fig. 6.8(a). It is observed that the

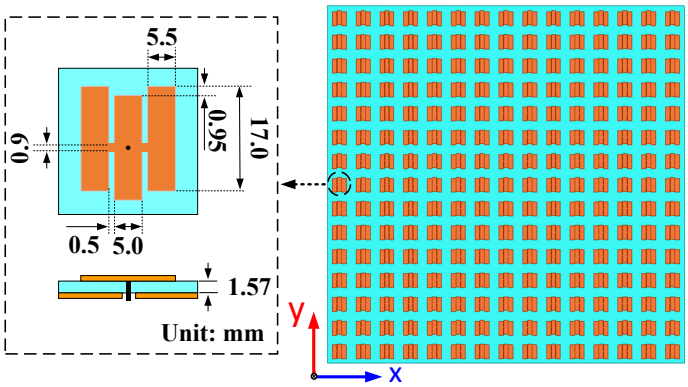

Figure 6.7: The 15 × 15-element planar array with a closed view of the adopted three-staggered-patch antenna.

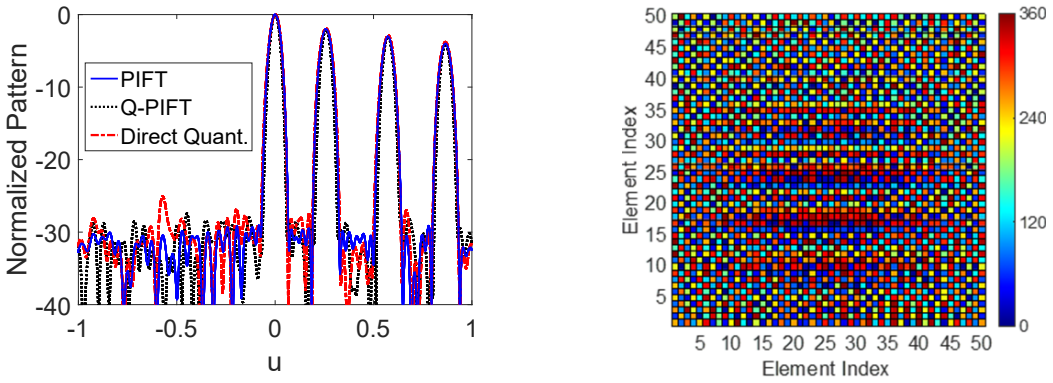

(a) (b)

Figure 6.8: The quad-beam patterns and the excitation phases for a 50 × 50-element planar array. (a) shows the pattern obtained by the PIFT, the 4-bit Q-PIFT, and the 4-bit direct quantization; (b) the excitation phases obtained by the PIFT.

pattern has a peak direction deviation of 0.1° with a peak power deviation of 0.22 dB. Furthermore, the SLL is about −22.95 dB. It is 4.45 dB worse than that obtained by the PIFT with continuous excitation phases. Then the Q-PIFT is utilized to synthesize this pattern. The discrete excitation phase interval Δ_φ is set as 22.5°. The obtained pattern is also shown in Fig. 6.8(a). It is observed that very accurate beam directions are achieved with peak power deviations smaller than 0.08 dB. Besides, the SLL is −26.64 dB. This value is 3.69 dB lower than that obtained by using direct quantization. By contrast, the superiority of the Q-PIFT has been demonstrated.

6.4 Summary

A novel phase-only dual- and multi-beam pattern synthesis method based on the PIFT was developed. The PIFT incorporates a partitioned calibration strategy into each iteration to achieve accurate beam directions by partitioning and calibrating the multiple beams individually without affecting each other. The main lobes and sidelobes are also iteratively corrected and modified to obtain desired peak powers and reduced SLLs. Numerical examples of synthesizing dual- and multi-beam patterns, including comparisons with other phase-only methods, are presented. Synthesized results show that multi-beam patterns with precisely controlled beam directions and peak powers, as well as reduced SLLs, can be obtained within only 3.56 minutes for large planar arrays with up to 2500 elements. Full-wave simulation results have validated that the PIFT can achieve precise beam direction control even when practical antennas are considered.

In addition, it has been validated that discrete excitation phases can also be optimized with the developed Q-PIFT to achieve accurate multi-beam patterns. The developed PIFT-based phase-only multi-beam pattern synthesis method can find significant applications in many wireless communications, especially when very accurate beam direction is required like in long-range communication. Compared to the amplitude optimization methods, the developed method that uses uniform amplitudes can lead to a much-simplified feeding network.

CHAPTER 7

MULTIBEAM ANTENNA ARRAY SYNTHESIS EMPLOYING THE GENERALIZED JOINED COUPLER MATRIX

7.1 Introduction

In Chapter 6, radiation patterns with accurate dual or multiple focused beams were efficiently synthesized with the partitioned iterative Fourier transform (PIFT) method for phased arrays. Another way of generating multibeams that features lower power consumption and low cost is using the analogue beamforming network. In [94], a systematic method of designing generalized joined coupler (GJC) matrix for multibeams was developed. Then a robust optimization method was developed in [95] to achieve low sidelobe levels (SLLs) and nulls for the multibeams using the GJC matrix.

In fact, owing to the intrinsic structure of the GJC matrix, the lower beams will split as a difference pattern when multiple beams are in the same direction. To avoid this problem, an effective strategy is to divide the whole scanning region into multiple sectors, and different beams are assigned to scan in their own allocated sectors, as the authors

did in [94, 95]. However, this strategy cannot achieve arbitrary beam scanning since beam overlapping must always be avoided. What is more, arbitrary beam scanning with beam overlapping is inevitable in some communications and radar applications where beam overlap is necessary. In this case, the beam splitting is unacceptable and should be resolved.

In this chapter, the beam splitting problem is thoroughly discussed. An effective strategy of using reconfigurable directional couplers is adopted to address this issue and to achieve continuous multibeam steering. To this end, a flexible synchronized optimization strategy that can consider multiple different cases is developed. The beam splitting issue can be well solved by using the developed optimization method with reconfigurable directional couplers. Moreover, multibeams with consistent and relatively low SLLs during scanning can be achieved by considering all the different multibeam scanning cases in a single optimization. Numerical results are provided to demonstrate the effectiveness of the developed method. A comparison with the classical method of designing the Blass matrix is also presented to comprehensively evaluate the developed GJC matrix design method.

This chapter is organized as follows. Formulation and algorithm are discussed in Section 7.2. Section 7.3 presents some numerical results. Section 7.4 draws the summary.

7.2 Formulations and Optimization Algorithm

7.2.1 Signal Flow in the GJC Matrix

The function of analogue beamforming networks, including the GJC matrix, is to output desired excitation vectors $\mathbf{w} = [w_1, w_2, ..., w_N]^T$ (T denotes matrix transpose) to feed an antenna array with N elements so as to achieve multibeams with desired directions. Generally, the input port number M decides the number of beams, whilst the output port

number N corresponds to the antenna element number. For the GJC matrix, the design target is to find the coupler value directing signal flow as well as the phase shifter value deciding beam directions in each node to yield the required excitations $\mathbf{w}$ at the output ports. In [94], the general signal transformation of a GJC matrix has been detailedly deduced. For a general GJC matrix shown in Fig. 7.1, suppose the signal transfer for the directional coupler is expressed by the scattering matrix, known as $\boldsymbol{S}$ matrix, as:

$$\mathbf{S} = \begin{bmatrix} 0 & j\sin\vartheta & \cos\vartheta & 0 \\ j\sin\vartheta & 0 & 0 & \cos\vartheta \\ \cos\vartheta & 0 & 0 & j\sin\vartheta \\ 0 & \cos\vartheta & j\sin\vartheta & 0 \end{bmatrix} \tag{7.1}$$

where $j = \sqrt{-1}$. Let φ_{mn} denotes the phase shifter value in the m^{th} row and n^{th} column. Then, according to [94], the output excitation vector $\mathbf{Y} = [y_1, y_2, ..., y_N]^T$ corresponding to the input vector $\mathbf{X} = [x_1, x_2, ..., x_M]^T$ can be obtained as:

$$\mathbf{Y} = \Omega_{M\times N}\mathbf{X}. \tag{7.2}$$

where $\Omega_{M\times N}$ is the signal transformation matrix of a $M \times N$ GJC matrix that can be obtained as:

$$\boldsymbol{\Omega}_{N\times M} = \begin{bmatrix} \left[\alpha^{(1)}_{M\times 1}\right]^T \\ \left[\alpha^{(2)}_{M\times 1}\right]^T \boldsymbol{A}^{(1)}_{M\times M} \\ \vdots \\ \left[\alpha^{(n)}_{M\times 1}\right]^T \boldsymbol{A}^{(n-1)}_{M\times M} \cdots \boldsymbol{A}^{(1)_{M\times M}} \\ \vdots \\ \left[\alpha^{(N)}_{M\times 1}\right]^T \boldsymbol{A}^{(N-1)}_{M\times M} \cdots \boldsymbol{A}^{(1)_{M\times M}} \end{bmatrix}_{N\times M} \tag{7.3}$$

In the above, the matrix $\boldsymbol{\alpha}^{(n)}_{M\times 1}$ can be obtained as:

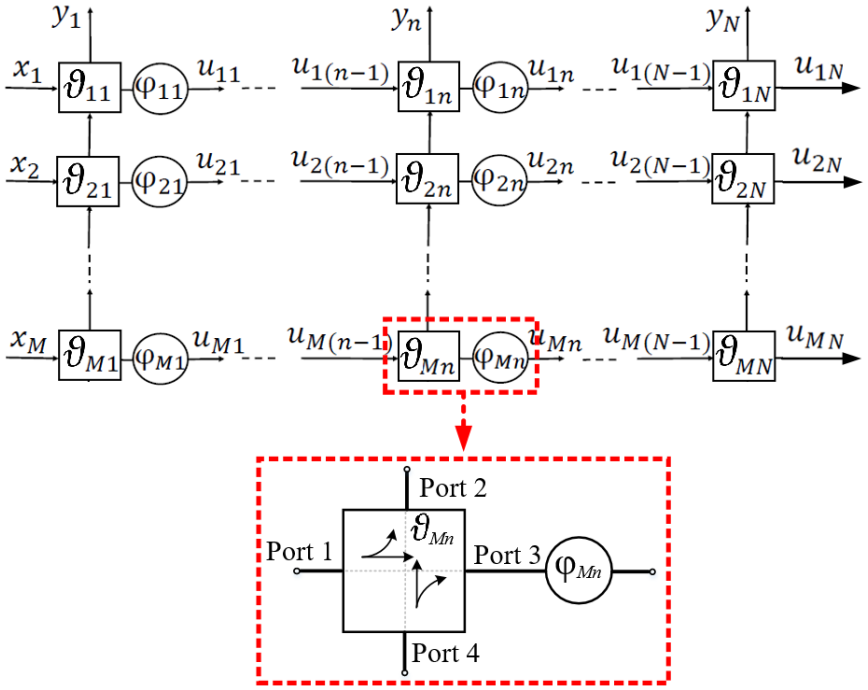

Figure 7.1: The structure of a $M \times N$ GJC matrix with an inset view of the node comprising of a directional coupler and a phase shifter.

$$\boldsymbol{\alpha}_{M\times 1}^{(n)} = \begin{bmatrix} j\sin\vartheta_{1n} \\ j\sin\vartheta_{2n}\cos\vartheta_{1n} \\ j\sin\vartheta_{3n}\cos\vartheta_{2n}\cos\vartheta_{1n} \\ \vdots \\ j\sin\vartheta_{Mn}\cos\vartheta_{(M-1)n}\cdots\cos\vartheta_{1n} \end{bmatrix}_{M\times 1} . \tag{7.4}$$

The matrix $\boldsymbol{A}_{M\times M}^{(n)}$ is given as:

$$\boldsymbol{A}_{M\times M}^{(n)} = \begin{bmatrix} \cos\vartheta_{1n}e^{-j\varphi_{1n}} & j^2\sin\vartheta_{1n}\sin\vartheta_{2n}e^{-j\varphi_{1n}} & \cdots & j^2\sin\vartheta_1 n\cos\vartheta_{2n}\ldots\cos\vartheta_{(M-1)n}\sin\vartheta_{Mn}e^{-j\varphi_{1n}} \\ 0 & \cos\vartheta_{2n}e^{-j\varphi_{2n}} & \cdots & j^2\sin\vartheta_{2n}\cos\vartheta_{3n}\ldots\cos\vartheta_{(M-1)n}\sin\vartheta_{Mn}e^{-j\varphi_{2n}} \\ 0 & 0 & \cdots & j^2\sin\vartheta_{3n}\cos\vartheta_{4n}\ldots\cos\vartheta_{(M-1)n}\sin\vartheta_{Mn}e^{-j\varphi_{3n}} \\ \vdots & \vdots & \ddots & \vdots \\ 0 & 0 & \cdots & \cos\vartheta_{Mn}e^{-j\varphi_{Mn}} \end{bmatrix} . \tag{7.5}$$

With the signal transform equation (7.2), the coupling values ϑ_{mn} and phase shifter values φ_{mn} for $m = 1,2,...,M$ and $n = 1,2,...,N$ can be designed to have desired output excitations for multibeam synthesis.

7.2.2 The Beam Splitting Issue for Overlapping Multibeams

The beam splitting issue when two or multiple beams are directed in the same direction for the GJC matrix is revealed in the following. As shown in Fig. 7.2, assume two beams generated by the first two rows of a Nolen-like GJC matrix have the same directions. In this case, all the phase shifter values in the first two rows are identical. Let Δ_φ denote the phase shifter values in the first two rows. According to equation (7.1), the coupling value and through value for the mn^{th} coupler is $j\sin\vartheta$ and $\cos\vartheta$, respectively. In other words, the coupling value and through value have a phase difference of 90°. This will not affect the first beam generated by feeding the first input port x_1. However, when the second input port x_2 is excited to generate the second beam, the main lobe splits as a difference pattern. The reason is as follows. When x_2 is excited, there are n signal flow paths in total towards the n^{th} element. Signals flow through the first $(n-1)$ paths have the phases of $(n-1)\Delta_\varphi - \pi/2$, as denoted with blue lines in Fig. 7.2, meanwhile the signal flows through the n^{th} path has a phase of $(n-1)\Delta_\varphi + \pi/2$, as denoted with a red line in Fig. 7.2. It means that the signals flowing through the first $(n-1)$ paths are anti-phase with respect to that flows through the n^{th} path.

When x_2 is excited, the yielded excitation at the n^{th} output port can be given as:

$$w_{2,n} = \sum_{i=1}^{n-1} a_i e^{j\left[(n-1)\Delta_\varphi - \pi/2\right]} + a_n e^{j\left[(n-1)\Delta_\varphi + \pi/2\right]} = \Big(\sum_{i=1}^{n-1} a_i - a_n\Big) e^{j\left[(n-1)\Delta_\varphi - \pi/2\right]} \tag{7.6}$$

where a_i $(i = 1, 2, ..., n)$ denotes the amplitude of the energy flowing through the i^{th} path. According to (7.6), if $\sum_{i=1}^{n-1} a_i$ is larger than a_n, the n^{th} element excitation phase would be $(n-1)\Delta_\varphi - \pi/2$; otherwise, the excitation phase would be $(n-1)\Delta_\varphi + \pi/2$. For normal excitation distributions like uniform or tapered distributions such as the Taylor or Chebyshev distribution, the coupling and through values are usually such that approximately half of the outputs (usually the left half of output ports) have $\sum_{i=1}^{n-1} a_i$ smaller than a_n, whilst the rest have $\sum_{i=1}^{n-1} a_i$ larger than a_n. In other words, around half of the outputs have excitation phases of $(n-1)\Delta_\varphi - \pi/2$ whilst the rest have excitation phases of $(n-1)\Delta_\varphi + \pi/2$.

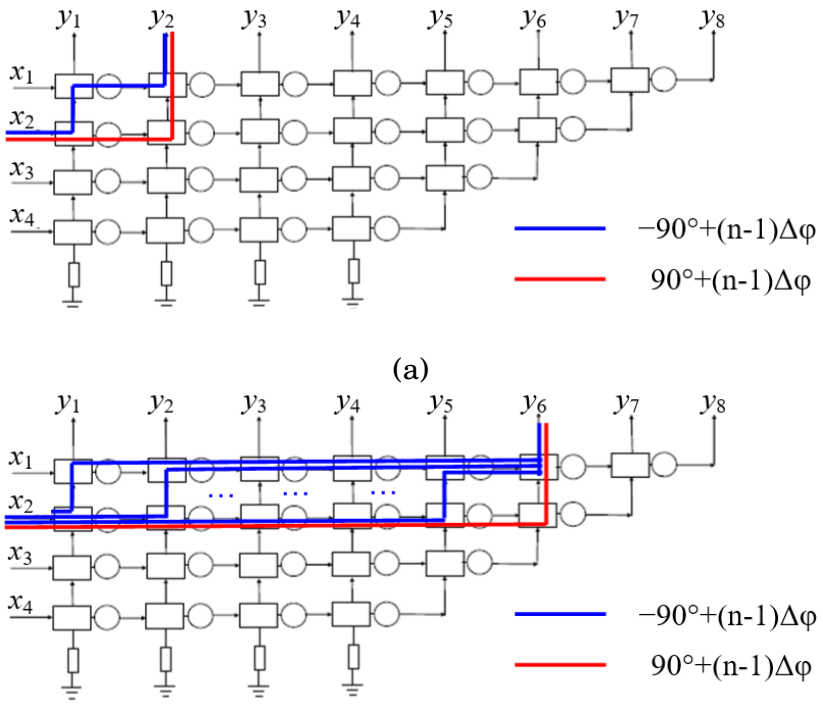

(a)

(b)

Figure 7.2: Signal flow in the first two rows when their beams have the same directions. Blue line denotes signal flow with a phase of $(n-1)\Delta_\varphi - \pi/2$, meanwhile red line denotes signal flow with a phase of $(n-1)\Delta_\varphi + \pi/2$, where Δ_φ denotes the phase shifter value in the first two rows.

It means that there is a 180° phase difference among some of the elements with respect to others, thereby resulting in a difference pattern.

To demonstrate this, two examples with uniform and Taylor distributions are provided here. Fig. 7.3(a) shows the multibeam patterns (the beam directions are {0°, −30°, 30°}) generated by a 3×12 Blass-like GJC matrix. The three beams are obtained by optimizing the coupler values to generate uniform output amplitudes with the method in [94]. After that, the second beam with an angular direction of −30° is steered to 0° (the same as the first beam) by altering the phase shifter values. As shown in Fig. 7.3(b), when the first two beams are overlapping, the second beam splits as a difference pattern. Table 7.1 gives the excitation amplitudes and phases of the multibeams when they are at {−30°, 0°, 30°} and {0°, 0°, 30°}, respectively. As can be seen, when the second beam is steered

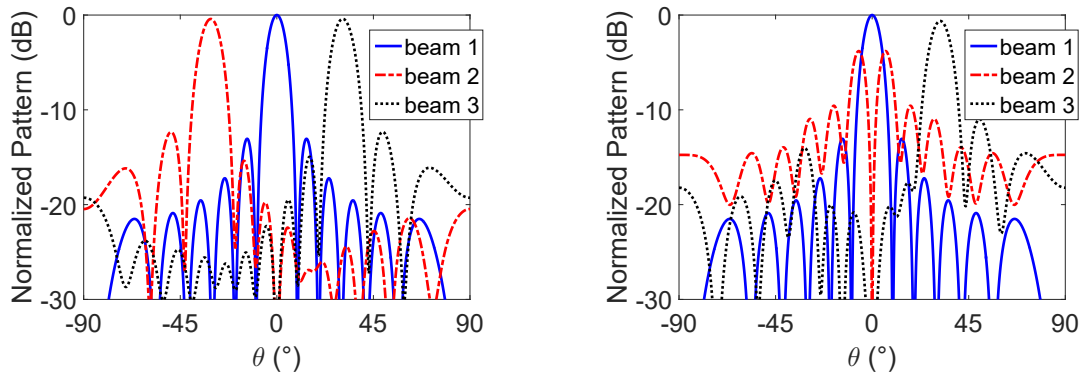

(a) (b)

Figure 7.3: Beam deterioration when the second beam generated by a 3×12 Blass-like GJC matrix overlaps the first beam. (a) shows the multibeams obtained by optimizing the ϑ_{mn} with beam directions of $-30°$, $0°$, and $30°$. (b) shows the second beam scanning from $0°$ to $-30°$.

Table 7.1: THE OUTPUT AMPLITUDES AND PHASES OBTAINED IN THE SYNTHESIS OF THE 3×12 BLASS-LIKE GJC MATRIX.

n	Initial Multibeam Directions {0°, −30°, 30°}						Multibeam Steering to {0°, 0°, 30°}					
	Amplitudes			Phases (°)			Amplitudes			Phases (°)		
	beam1	beam2	beam3	beam1	beam2	beam3	beam1	beam2	beam3	beam1	beam2	beam3
1	0.29	0.29	0.29	90	90	90	0.29	0.29	0.29	90	90	90
2	0.29	0.29	0.29	90	-174.8	-5.2	0.29	0.26	0.26	90	90	-12.0
3	0.29	0.29	0.29	90	-84.3	-95.7	0.29	0.21	0.31	90	90	-99.5
4	0.29	0.29	0.29	90	0.6	179.5	0.29	0.18	0.28	90	90	178.1
5	0.29	0.29	0.29	90	90.7	89.3	0.29	0.17	0.30	90	90	88.2
6	0.29	0.29	0.29	90	-172.4	-7.6	0.29	0.13	0.26	90	90	-17.6
7	0.29	0.29	0.28	90	-81.4	-98.9	0.29	0.04	0.32	90	90	-102.9
8	0.29	0.29	0.28	90	2.3	177.9	0.29	0.01	0.25	90	-90	172.1
9	0.29	0.29	0.29	90	93.6	87.2	0.29	0.04	0.32	90	-90	83.2
10	0.29	0.29	0.31	90	-163.7	-16.1	0.29	0.15	0.27	90	-90	-42.6
11	0.29	0.29	0.28	90	-67.3	-116.5	0.29	0.35	0.29	90	-90	-118.0
12	0.29	0.15	0.15	90	43.1	146.6	0.29	0.72	0.24	90	-90	80.7

to 0°, a total number of 5 elements are anti-phase with respect to the rest elements.

Another example is generating Taylor distribution with −20 dB SLLs for a 2×12 Blass-like GJC matrix. Similarly, the coupler values are optimized utilizing the method in [94] to generate the required Taylor distribution. Fig. 7.4(a) shows the optimized patterns with beam directions of {0°, −30°}. However, when the two beams are overlapping at 0°, beam splitting occurs to the second beam, as can be seen in Fig. 7.4(b). As given

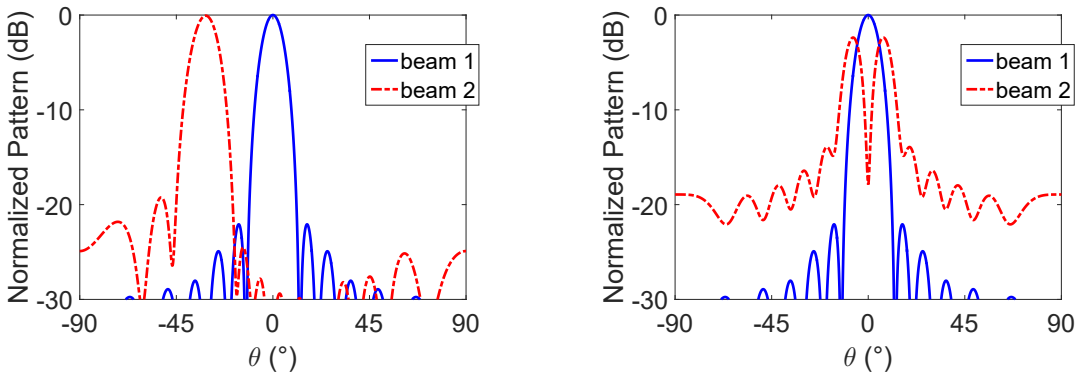

(a) (b)

Figure 7.4: Beam deterioration when the second beam generated by a 2×12 Blass-like GJC matrix overlaps the first beam. (a) shows the multibeams obtained by optimizing the ϑ_{mn} with beam directions of 0°, and −30°. (b) shows beam 2 scanning from 0° to −30°.

in Table 7.2, when the two beams are both at 0°, some of the excitation phases for the second beam have 180° phase difference with respect to others. These two examples have validated the aforementioned statement regarding the beam splitting.

Here only the overlapping of two beams is presented. It should be noted that when M beams are overlapping, a total number of $M-1$ beams generated by the lower rows will split. This greatly restricts the application of the GJC matrix in many wireless communication and radar systems where beam overlapping is necessary. This issue must be carefully addressed to enhance the attractiveness of the GJC matrix.

To address this issue, reconfigurable directional couplers [120] can be used to have switchable coupler values for cases with or without beam overlapping. When there is no beam overlapping, the coupler values can be optimized naturally. When there is beam overlapping, in terms of the Blass-like GJC matrix, the coupling values can be optimized as such that $\sum_{i=1}^{n-1} a_i$ is always smaller than a_n. In this case, there would not be anti-phases since $\sum_{i=1}^{n-1} a_i - a_n$ is always positive. The consequence is that there will be an amount of energy flowing to the matching load at the end of each row. On the other hand, for the Nolen-like GJC matrix, this method is no longer feasible since there is

Table 7.2: THE OUTPUT AMPLITUDES AND PHASES OBTAINED IN THE SYNTHESIS OF THE 2×12 BLASS-LIKE GJC MATRIX.

n	Initial Multibeam {0°, −30°}				Multibeam Steering to {0°, 0°}			
	Amplitudes		Phases (°)		Amplitudes		Phases (°)	
	beam1	beam2	beam1	beam2	beam1	beam2	beam1	beam2
1	0.14	0.14	90	90	0.14	0.14	90	90
2	0.20	0.20	90	-178.9	0.20	0.20	90	90
3	0.26	0.26	90	-87.6	0.26	0.24	90	90
4	0.31	0.31	90	3.3	0.31	0.26	90	90
5	0.36	0.36	90	94.6	0.36	0.24	90	90
6	0.38	0.37	90	-172.5	0.38	0.17	90	90
7	0.38	0.38	90	-79.5	0.38	0.06	90	90
8	0.36	0.36	90	13.3	0.36	0.10	90	-90
9	0.31	0.31	90	105.3	0.31	0.24	90	-90
10	0.26	0.26	90	-160.1	0.26	0.37	90	-90
11	0.20	0.21	90	-60.6	0.20	0.46	90	-90
12	0.14	0.14	90	59.1	0.14	0.56	90	-90

no matching load at the end of each row. Another effective strategy is to optimize the coupling values such that the signals that flow to the outputs having anti-phases have very small powers. In this case, although they are anti-phase, their amplitudes are so small that they would not affect the pattern much. However, the potential problem is that the array gain would decrease to a certain extent. The beam splitting issue will be addressed and demonstrated with examples in the Section 7.3.

7.2.3 A Synchronized Optimization Strategy

For an N-element linear array, according to equation (2.1), the array radiation pattern considering active element pattern is given as:

$$F_m(\mathbf{w}_m;\theta) = \sum_{n=0}^{N-1} w_{mn} E_n(\theta) e^{j\beta r_n \cos\theta} \tag{7.7}$$

where $\theta \in [-90°, 90°]$ is the angle of observation, $\mathbf{w}_m = [w_{m1}, w_{m2}, ..., w_{mN}]^T$ is the output excitation vector of the GJC matrix for the m^{th} beam, $E_n(\theta)$ and r_n is the n^{th} antenna element radiation pattern and position. $\beta = 2\pi/\lambda$ is the propagation constant.

The target of designing a GJC matrix is to find the directional coupler values ϑ_{mn} as well as phase shifter values φ_{mn} resulting in an output excitation vector $\mathbf{w}$ such that the

multibeam patterns have desired beam directions and relatively low SLLs. Basically, the phase shifter values can be directly calculated according to the beam directions as:

$$\varphi_{mn} = \beta r_n \sin\theta_m \tag{7.8}$$

where θ_m is the peak direction of the m^{th} beam. On the other hand, obtaining the coupler values ϑ_{mn} to yield excitation vectors $\mathbf{w}_m$ using equation (7.2) for generating desired multibeams is a highly non-linear problem. A proper cost function can be constructed and a stochastic algorithm can be utilized to minimize the cost function value to obtain desired multibeams. The cost function similar to the one in [121] is given as:

$$f_{\text{cost}} = \sum_{m=1}^{C\times M}\left[W_1\left(\frac{1}{2}\left(X_p^{(m)} + \left|X_p^{(m)}\right|\right)\right)^2 + W_2\left(\frac{1}{2}\left(Y^{(m)} + \left|Y^{(m)}\right|\right)\right)^2 + \sum_{b=1}^{B}\frac{W^{(m)}}{B}\left(\frac{1}{2}\left(Z_b^{(m)} + \left|Z_b^{(m)}\right|\right)\right)^2\right] \tag{7.9}$$

where

$$X_p^{(m)} = F^{(m)}(\theta_p^{(m)}) - 0, \tag{7.10}$$

$$Y^{(m)} = 1 - \eta_t^{(m)}, \tag{7.11}$$

$$Z_b^{(m)} = F^{(m)}(\theta_b^{(m)}) - \Gamma_{SLL}. \tag{7.12}$$

$F^{(m)}$ is the m^{th} beam pattern normalized to the maximum gain of the multibeams, $\theta_p^{(m)}$ is the peak direction angle of $F^{(m)}$. $\theta_b^{(m)}(b = 1,2,...,B)$ are the sampling angles in the m^{th} beam pattern sidelobe region. $\eta_t^{(m)}$ is the transmission efficiency of the mth beam. W_1, W_2, and $W^{(m)}$ $(m = 1,2,...,M,M+1,...,C\times M)$ are the weighting coefficients. C is the total number of cases. By considering C different cases, each with M beams with different directions, different beam overlapping conditions can be considered simultaneously. What is more, by adopting the constraint (7.10) in the cost function, the peak gains of the multibeams can be optimized to have equal power to resolve the beam splitting issue. In addition, multibeams with stable and global low SLLs during scanning can also be achieved by considering different beam scanning angles for the multibeams simultaneously. Note that constraint (7.11) is for the optimization of the Blass-like GJC

matrix, and there is no need for the Nolen-like GJC matrix since the transmission efficiency is always 1. The principle of designing the cost function (7.9) is similar to that for the cost function (3.7) in Chapter 3. Further explanations are thus omitted here.

Minimizing the cost function (7.9) to find the optimal coupling values ϑ_{mn} for $m = 1,2,...,M$ and $n = 1,2,...,N$ is a highly non-linear problem. In general, global stochastic algorithms would be adequate for the optimization. The particle swarm optimization (PSO) algorithm used in the previous chapters is employed for the optimization here.

7.3 Synthesis results

In this section, the beam overlapping issue is first resolved by adopting reconfigurable directional couplers to achieve continuously multibeam scanning. In addition, examples of optimizing the GJC matrices to achieve multibeams with stable SLLs are presented.

7.3.1 Optimization of the GJC Matrix to Address the Beam Splitting for Continuous Multibeam Scanning

As aforementioned, a serious problem that must be carefully addressed for the GJC matrix is that the lower beams will split as difference patterns when two or more beams are scanned to the same directions. To avoid this problem, a straightforward and effective method is to divide the beam scanning range into several sectors according to the beam number, as the authors did in [94, 95]. In that case, different beams will work in their own scanning range and, thus, identical beam direction angles and, hence, beam splitting can be avoided. However, in some communications and radar applications, arbitrarily scannable multibeams with beam overlapping are necessary. Therefore, addressing the beam splitting issue of the GJC matrix is necessary.

In the following, this problem is solved by using the developed synchronized optimiza-

tion strategy with reconfigurable directional couplers. Basically, there are two different multibeam scanning cases: multibeams without beam overlapping and multibeams with beam overlapping. For these two cases, two sets of directional coupler values can be optimized individually, and reconfigurable directional couplers can be employed to reconfigure their coupler values between these two sets of optimized values. On the other hand, the phase shifter values can be either calculated with (7.8) or optimized along with the coupler values. For the optimization, when there is no beam overlapping, the coupler values can be readily optimized, and there will not be any issue. In the following, multibeams with beam overlapping are optimized to address the beam splitting issue.

As the first example, suppose three beams are required in a practical radar application for simultaneous communication and sensing. The first two beams are employed for communication, and their scanning ranges are fixed at [−50°, −5°] and [5°, 50°], respectively. The third beam is utilized for sensing that must scan to an arbitrary angle in [−50°, 50°]. A 3×12 Blass-like GJC matrix consisting of reconfigurable directional couplers is used. Two sets of coupler values are optimized with the phase shifter values calculated using (7.8). For the optimization of multibeams with beam overlapping, the two beams for communication are firstly fixed at specific directions, for example, −30° and 30°. Then the direction of the third beam is either at −30° or 30°, which overlaps with the first or the second beam, respectively. In other words, two cases with beam directions of {−30°, 30°, −30°} (the third beam overlaps the first one) and {−30°, 30°, 30°} (the third beam overlaps the second one) are considered simultaneously in the optimization. Then all the coupler values in the three rows are optimized simultaneously using the developed method to achieve beams without splitting as well as relatively low SLLs. In the PSO-based optimization, the desired SLLs are set as $\Gamma_{SLL} = -20$ dB, the population size is $Np = 36$, the maximum number of iterations is $I_m = 800$, the weighting factors of the cost function are $W_1 = W_2 = W^{(m)} = 1$.

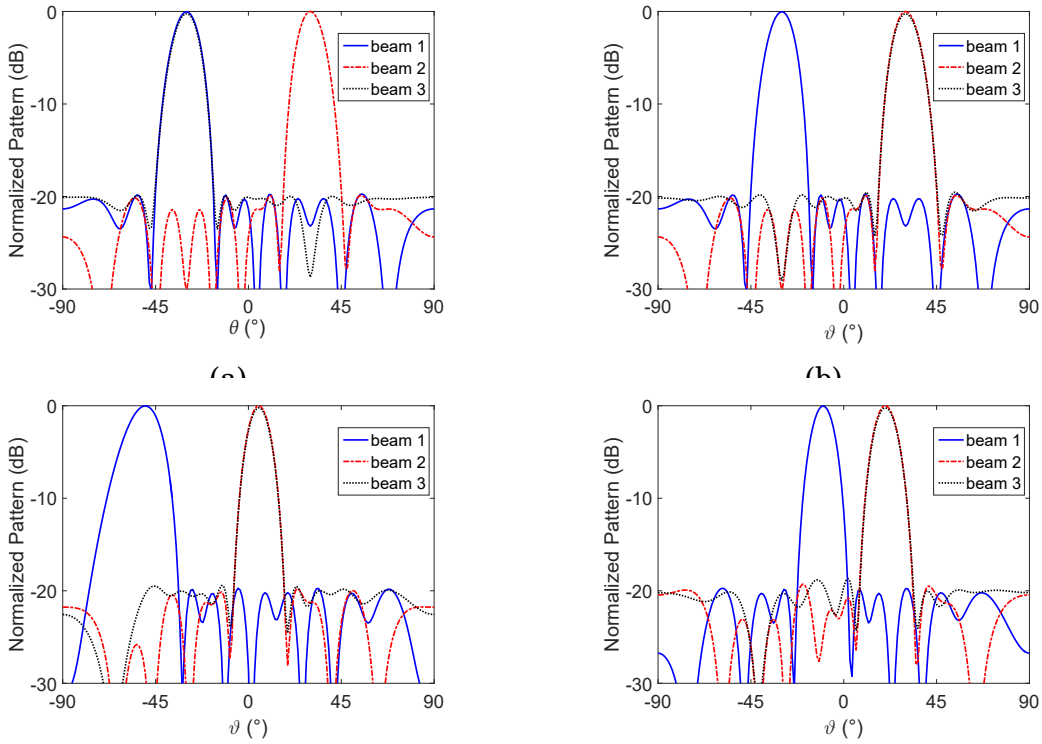

Figure 7.5: The synthesized multibeam patterns with beam overlapping by using a 3×12 Blass-like GJC matrix. The multibeam angles are (a) {−30°, 30°, −30°}, (b) {−30°, 30°, 30°}, (c) {−50°, 5°, 5°}, and (d) {−10°, 20°, 20°}, respectively. The overall transmission efficiency is about 54.8%.

Table 7.3: THE OUTPUT AMPLITUDES AND PHASES OBTAINED IN THE SYNTHESIS OF A 3×12 NOLEN-LIKE GJC MATRIX WITH THE MAIN BEAMS AT {30°, 0°, 0°}.

n	Amplitudes			Phases (°)		
	beam 1	beam 2	beam 3	beam1	beam 2	beam 3
1	0.00	0.02	0.27	90	90	90
2	0.02	0.03	0.25	0	90	90
3	0.17	0.14	0.20	-90	90	90.2
4	0.11	0.12	0.31	-180	91.3	90.7
5	0.23	0.22	0.26	90	90.8	91.6
6	0.28	0.29	0.29	0	91.6	91.7
7	0.31	0.28	0.21	-90	95.2	95.1
8	0.25	0.27	0.21	-180	94.4	93.8
9	0.29	0.29	0.13	90	90.8	91.6
10	0.23	0.24	0.08	0	92.5	90.2
11	0.23	0.23	0.03	-90	95.0	98.5
12	0.19	0.21	0.01	-180	93.2	114.1

The optimized results are shown in Fig. 7.5(a) and (b). It is observed that there is not any beam splitting observed when the third beam scan to the first or the second beam directions. In addition, the beams can be steered to any directions in the scanning region by just altering the phase shifter values according to (7.8), and there is no beam splitting. For simplicity, only two cases with beam directions of {−50°, 5°, 5°} and {−10°, 20°, 20°} are shown in Fig. 7.5(c) and (d). The excitation amplitudes and phases with multibeam directions of {30°, 0°, 0°} are shown in Table 7.3. As can be seen, for beam 2 and beam 3, there is not any anti-phase after the optimization. It is noted that some of the excitation phases are slightly different from 90° (ideal phase for the beam at 0°) due to the multi-path effect of the GJC matrix. As mentioned before, for the Blass-like GJC matrix, the consequence is that there will be an amount of energy flowing to the matching load at the end of each row. In this example, the overall transmission efficiency of the Blass-like GJC matrix is about 54.8%.

To further show the effectiveness of the developed method, another example is presented here. Suppose three beams are required and they need to scan to an arbitrary angle within [−50°, 50°]. It means that all three beams or two of them may overlap. To resolve the beam splitting, the developed synchronized optimization strategy employing reconfigurable direction couplers is adopted. In the PSO-based optimization, all the parameters are set the same as previous example. The optimized results with beam overlapping are shown in Fig. 7.6. As can be seen, no matter the overlapping of three or any two beams of them, there is not any beam splitting. What is more, the SLLs are always below −20 dB. In this case, however, the resulting overall transmission efficiency is only 29.4 %.

For the Nolen-like GJC matrix, it is more difficult to resolve the beam splitting issue since there is no any matching load to absorb the energy. In that case, anti-phases are inevitable. A potential solution is to minimize the powers that flow into the anti-phase

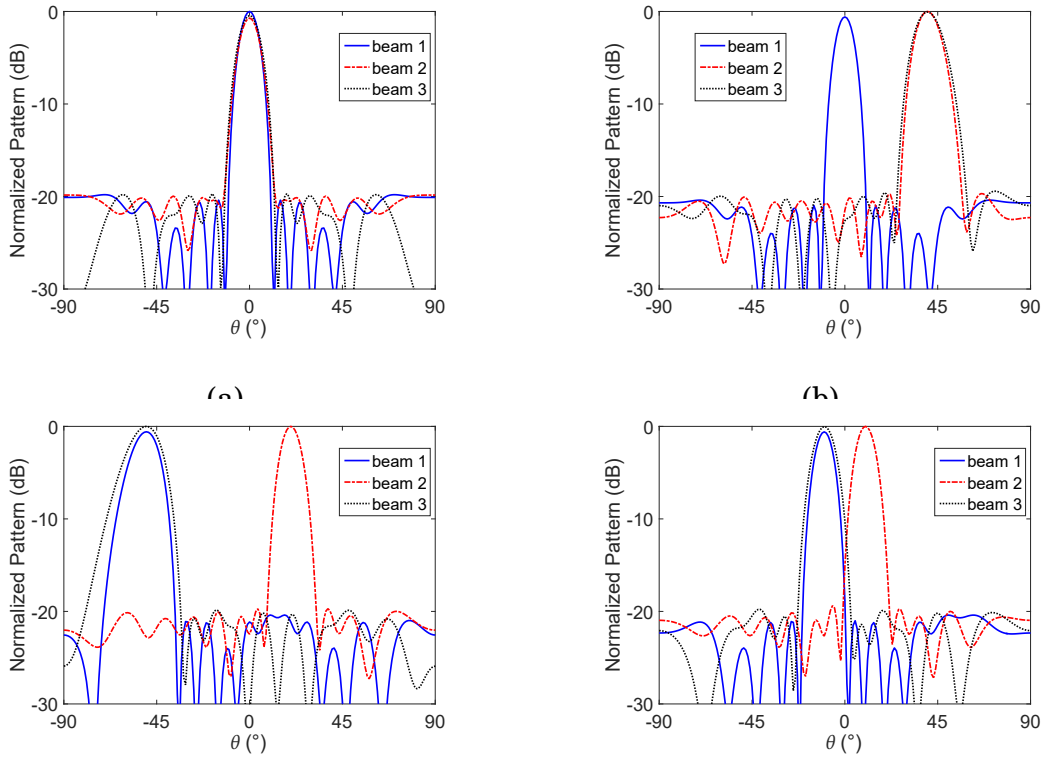

Figure 7.6: Multibeam scanning patterns with beam overlapping by using a 3×12 Blass-like GJC matrix. The multibeam angles are (a) {0°, 0°, 0°}, (b) {0°, 40°, 40°}, (c) {−50°, 20°, −50°}, and (d) {−10°, 10°, −10°}, respectively. The transmission efficiency is about 29.4%.

ports. Here, the developed optimization method is utilized to optimize both the coupler values and the phase shifter values with a 3×12 Nolen-like GJC matrix to address this issue. The desired SLLs are set as $\Gamma_{SLL} = -15$ dB. The parameters for the PSO is used the same as before except that the population size is $Np = 60$. It should be noted that different from the Blass-like GJC matrix which only two sets of coupler values are required, the Nolen-like GJC matrix requires three sets of coupler values and phase shifter values when there are three beams due to its complexity. One set of coupler values and phase shifter values for three beams overlapping, one set for any two of the three beams overlapping, and one set for the case without beam overlapping.

The optimized multibeams are shown in Fig. 7.7. As is shown that the beam splitting

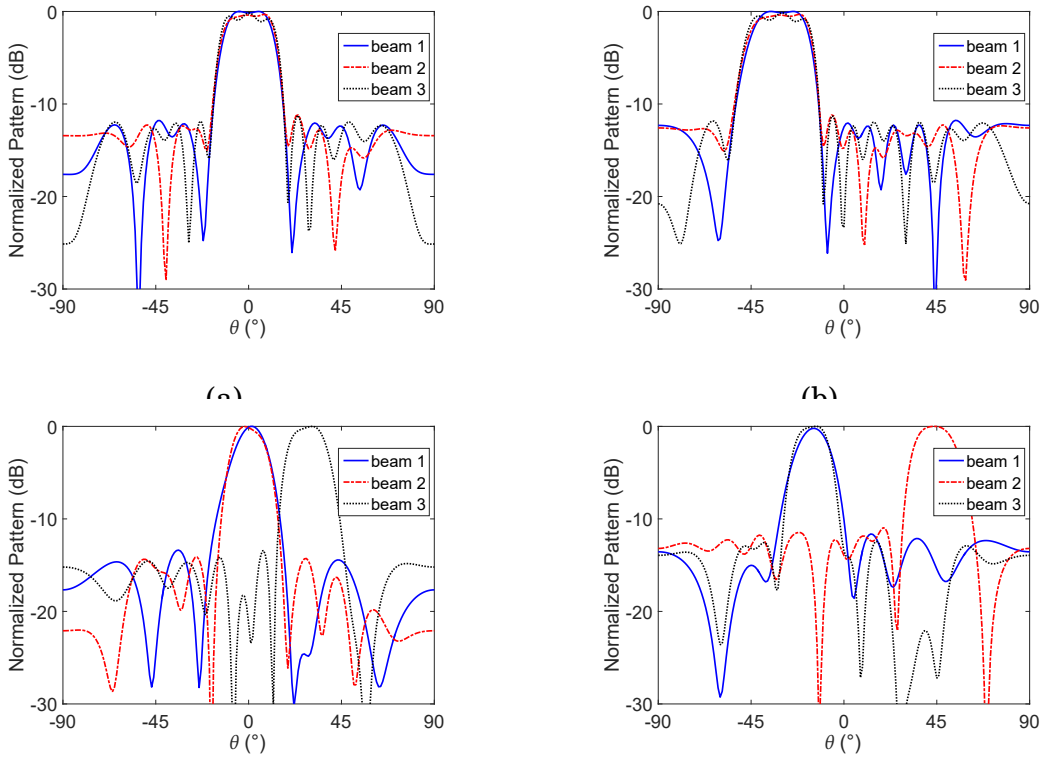

Figure 7.7: The synthesized mutlibeam patterns with beam overlapping for a 3×12 Nolen-like GJC matrix by optimizing the ϑ_{mn} and ϕ_{mn} simultaneously. (a), (b), (c), and (d) show the patterns with beam directions of {0°, 0°, 0°}, {−30°, −30°, −30°}, {0°, 0°, 30°}, {−15°, 45°, −15°}, respectively.

issue is well solved. For the cases with two or three beams overlapping, there is no beam splitting observed. The optimized excitation amplitudes and phases for the three beams with directions of [0°, 0°, 0°] are shown in Table 7.4. It is noted that the anti-phase elements are generally optimized to have small amplitudes.

7.3.2 Beam Scanning with Stable SLLs using Calculated Progressive Phases

In this example, the developed method is utilized to achieve beam scanning with stable SLLs. In the referenced methods [94, 95], only multibeams with fixed angles were

Table 7.4: THE OUTPUT AMPLITUDES AND PHASES OBTAINED IN THE SYNTHESIS OF THE 3×12 NOLEN-LIKE GJC MATRIX WITH THE MAIN BEAMS SCANNED TO {0°, 0°, 0°}.

n	Amplitudes			Phases (°)		
	beam 1	beam 2	beam 3	beam1	beam 2	beam 3
1	0.18	0.56	0.16	90	90	90
2	0.01	0.48	0.06	87.5	96.5	79.9
3	0.04	0.53	0.05	-9.4	87.6	-75.5
4	0.34	0.28	0.17	-99.5	92.5	-101.0
5	0.36	0.23	0.06	-96.7	93.9	-87.8
6	0.44	0.12	0.04	-103.5	82.0	-145.0
7	0.50	0.10	0.04	-96.3	-91.2	74.8
8	0.50	0.12	0.16	-92.8	-79.9	71.1
9	0.08	0.04	0.46	-115.5	-60.5	81.9
10	0.01	0.07	0.51	94.7	-105.4	79.8
11	0.12	0.03	0.40	-101.6	147.8	81.7
12	0.11	0.08	0.53	82.4	92.10	82.1

optimized at a time, and with the optimized coupler values, multibeams at other scanning angles were obtained by changing the phase shifter values only. The problem is that, since only one set of beam angles is considered in the optimization, the SLLs and gains may deteriorate after scanning owing to the multi-path effect of the GJC matrix. This problem can be solved by using the developed synchronized optimization strategy by considering multiple beam scanning cases. By setting C cases with differently scanned multibeams, it is possible to achieve global low and stable SLLs such that the SLLs will not deteriorate during scanning.

A 3×17 Nolen-like GJC matrix is considered here to achieve three scannable beams in the ranges of [−40°, −20°], [−10°, 10°], and [20°, 40°]. Each beam scans at an interval of 10°. For example, the first beam can scan to −40°, −30°, and −20°. In this case, C is set as $3^3 = 27$ since there are 27 different scanning angle combinations. The desired SLLs are set as $\Gamma_{SLL} = -20$ dB for all the possible scanning angles of the multibeams. The parameters for the PSO is used the same as before except that the population size is $Np = 48$. The optimized results are shown in Fig. 7.8. It can be seen that, for multibeams with any possible scanning angles, the SLLs always remain below −20 dB. Moreover, all the beams have consistent gains, which has demonstrated the favorable performance of

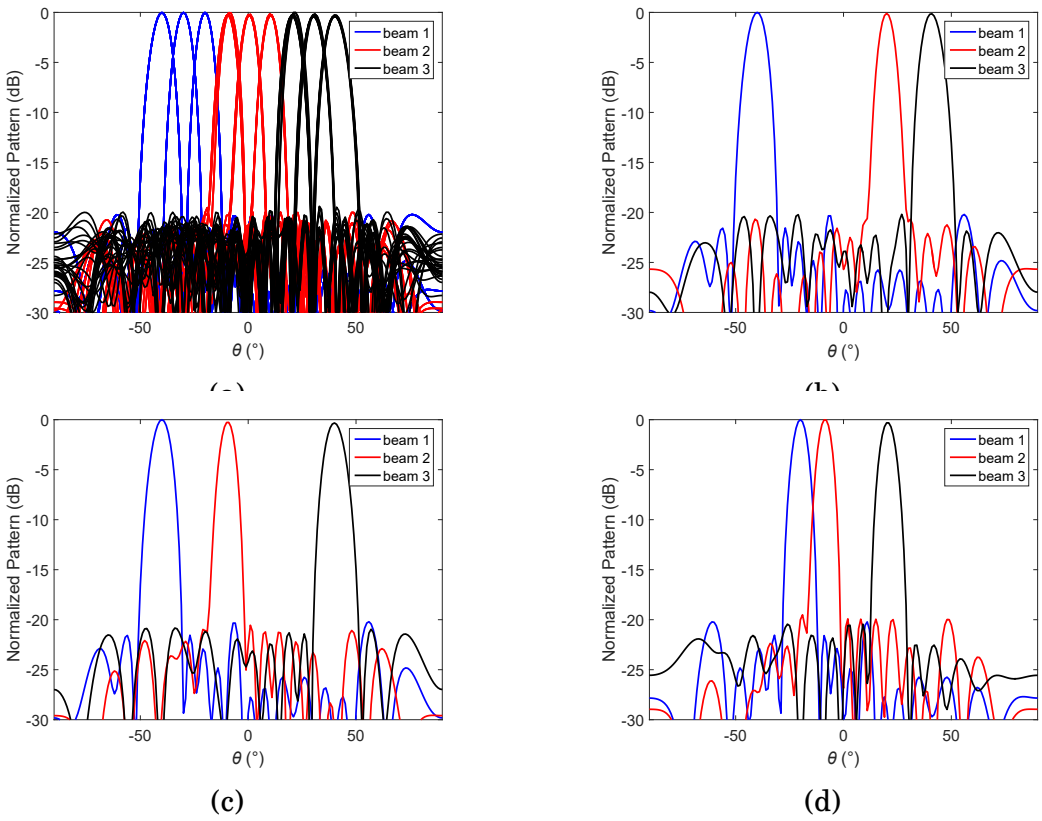

Figure 7.8: Beam scanning with stable SLLs with calculated progressive phases. (a) mutlibeams with different scanning angles. (b), (c), and (d) show mutlibeams with scanning angles of {−40°, 20°, 40°}, {−40°, −10°, 40°}, and {−20°, −10°, 20°}, respectively.

the developed method.

7.3.3 Comparison with a Classical Blass Matrix Design Method

To further evaluate the developed method, a comparison with a classical Blass matrix optimization method by Mosca is provided with a 5×20 Blass-like GJC matrix. In [122], the multivariable nonlinear problem of designing a Blass matrix was reduced to a one-variable linear programming problem by assuming the power at each row only dissipated by the matching load at the end of that row. Then the loss of each row was minimized by easily solving the linear programming problem with the help of the Gram-Schmidt orthogonalization. However, the multi-path effect was not considered, and the efficiency

of each row was only as high as 90%. Here, this method is first utilized to optimize a 5×20 Blass matrix to design multibeams directing at {−40°, −20°, 0°, 20°, 40°}. The target output amplitude distribution is the Taylor distribution, and the SLLs are −25 dB. The results obtained by the reference method in [122] are shown in Fig. 7.9. As is seen, −25 dB SLLs are obtained. The transmission efficiencies of the five beams are 89.8%, 89.9%, 89.0%, 87.8%, and 84.9%, respectively.

Then, the developed method is employed to design the same multibeams employing a 5×20 Blass-like GJC matrix. The beam directions and the desired SLLs are set the same as before. The population size of the PSO si set as $Np = 54$, and all the parameters are set the same as the previous example. The optimized multibeam patterns are shown in Fig. 7.10. As is shown, −25 dB SLLs are obtained for all five beams. The optimized excitation amplitudes are listed in Table 7.5. Table 7.6 provides a comparison between the proposed method and the reference method in [122] in terms of computational efficiency, time consumption, memory usage, and transmission efficiency. The results show that the proposed method achieves better transmission efficiency compared to the Blass matrix optimization method by Mosca. The overall transmission efficiency is about 98.9%, indicating nearly lossless transmission. However, it should be noted that the proposed method employing the stochastic algorithm PSO requires more time and memory during the optimization process. This suggests that further improvements are necessary to enhance the efficiency of the proposed method.

In conclusion, while the proposed method outperforms the reference method in terms of transmission efficiency, there is room for improvement in terms of computational efficiency, time consumption, and memory occupation. Future research and optimization efforts can address these areas to enhance the proposed method.

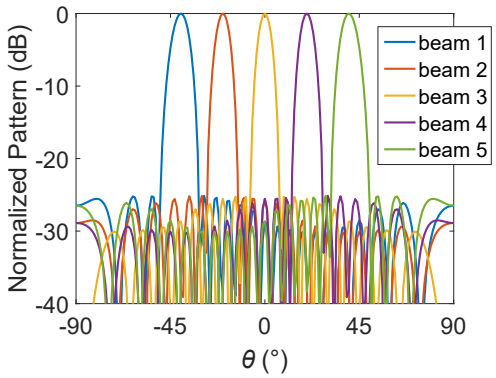

Figure 7.9: The mutlibeam patterns for a 5×20 Blass matrix obtained by the method in [122]. The beam directions are {−40°, −20°, 0°, 20°, 40°}, and efficiencies of the 5 beams are 89.8%, 89.9%, 89.0%, 87.8%, and 84.9%, respectively.

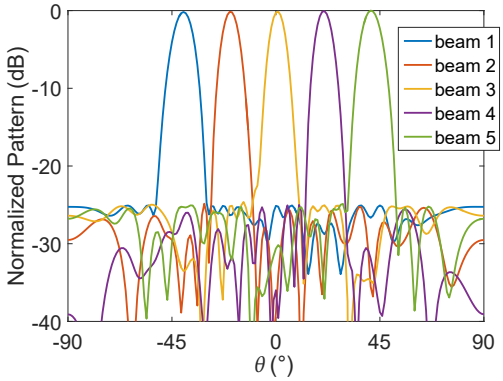

Figure 7.10: The synthesized mutlibeam patterns for a 5×20 Blass-like GJC matrix by optimizing the ϑ_{mn}. The beam directions are {−40°, −20°, 0°, 20°, 40°}.

7.4 Summary

In this chapter, a novel synchronized optimization strategy employing reconfigurable directional couplers is developed for the design of the GJC matrix to produce continuously scannable multibeams with relatively low SLLs. The beam splitting issue when beams overlap was thoroughly discussed and well addressed for both Blass- and Nolen-like GJC matrices. Besides, multibeams with different scanning angles can be considered simultaneously by using the developed optimization strategy to achieve global low and stable SLLs. Moreover, a comparison between the GJC matrix and the classical Blass

Table 7.5: THE OUTPUT AMPLITUDES OBTAINED IN THE SYNTHESIS OF THE 5×20 BLASS-LIKE GJC MATRIX.

n	beam 1	beam 2	beam 3	beam 4	beam 5
1	0.17	0.13	0.17	0.11	0.11
2	0.16	0.14	0.15	0.12	0.17
3	0.22	0.14	0.29	0.16	0.21
4	0.31	0.21	0.19	0.16	0.18
5	0.18	0.25	0.26	0.26	0.24
6	0.26	0.27	0.32	0.27	0.27
7	0.32	0.35	0.30	0.30	0.31
8	0.34	0.27	0.34	0.28	0.31
9	0.30	0.34	0.32	0.34	0.27
10	0.28	0.32	0.29	0.33	0.31
11	0.27	0.34	0.29	0.32	0.31
12	0.29	0.28	0.24	0.27	0.29
13	0.21	0.20	0.20	0.25	0.22
14	0.19	0.23	0.18	0.23	0.26
15	0.13	0.16	0.15	0.20	0.15
16	0.15	0.14	0.12	0.16	0.17
17	0.08	0.11	0.08	0.12	0.12
18	0.06	0.10	0.06	0.09	0.08
19	0.04	0.04	0.05	0.07	0.09
20	0.04	0.04	0.04	0.04	0.06

Table 7.6: PERFORMANCE COMPARISON BETWEEN THE PROPOSED METHOD AND THE REFERENCE METHOD IN [121] FOR THE SYNTHESIS OF A 5×20 BLASS MATRIX.

Method	Computational Complexity	Time Cost (Seconds)	Memory (MB)	Transmission Efficiency
Method in [122]	$O(MN)$	0.1	0.2	88.3%
Proposed Method	$O(I_m N_p M^2 N^2)$	64.8	9.9	98.9%

matrix design method was presented to demonstrate the superiority of the GJC matrix.

The developed synchronized optimization method employing a reconfigurable strategy has solved the beam splitting problem of the GJC matrix, which completes the study of the GJC matrix and makes it more attractive in modern fifth-generation (5G) and beyond 5G (B5G) wireless communications like the joint communication and sensing (JCAS) where beam overlapping is essential.

CHAPTER 8

CONCLUSION AND FUTURE WORK

8.1 Conclusion

In this dissertation, several novel techniques were developed to achieve desired pattern synthesis with simplified and cost-effective feeding networks. Those techniques can be categorized into two parts: the first part is replacing excitation amplitude modulation with element rotation to simplify the structure of the feeding network; the second part is multibeam synthesis.

Since pattern synthesis including shaped pattern and sum-and-difference pattern synthesis to achieve decent performance are complicated, the majority of existing methods optimized excitation amplitudes and phases for obtaining good control on both the main lobe shape and sidelobe level (SLL). As a consequence, the obtained array usually requires a complicated feeding network to implement nonuniform excitation amplitudes. Multiple unequal power dividers must be designed with much attention, and that will also result in an increase in the weight as well as the cost of the antenna array system.

Polarization of the antenna can be considered as an optimization variable that can be used in pattern synthesis. In this dissertation, the polarization rotations or the antenna rotations were modulated to synthesize sum-and-difference patterns and shaped-beam patterns. Sum-and-difference patterns were first synthesized through optimization of the antenna rotation angles and positions to achieve low SLLs and steep difference pattern slopes for linear dipole arrays. After that, shaped power patterns were synthesized by optimizing element rotations and excitation phases considering mutual coupling and arbitrary antenna structures for the linear and planar array. Further extension of this method was achieved then to deal with shaped pattern synthesis for cylindrical conformal arrays considering mutual coupling. Favorable main lobe shapes and relatively low SLLs were obtained. Comparisons showed that the element rotation-based method can achieve equivalent performance in terms of SLL and main lobe shape as the amplitude optimization methods as some excitation amplitude optimization methods.

The second part is multibeam synthesis. Firstly, a phase-only multibeam pattern synthesis method based on the partitioned iterative Fourier transform (PIFT) was developed for phased array. The PIFT incorporates a partitioned calibration strategy into each iteration to achieve accurate beam directions by partitioning and calibrating the multiple beams individually without affecting each other. The main lobes and the sidelobes are also iteratively corrected and modified to obtain desired peak powers and reduced SLLs. Numerical examples including comparisons with other phase-only methods were presented to show the effectiveness of the developed method. Synthesized results showed that multibeam patterns with precisely controlled beam directions and peak powers, as well as reduced SLLs, can be obtained within only 3.56 minutes for large planar arrays with up to 2500 elements. Full-wave simulation results have validated that the PIFT can achieve precise beam direction control even when practical antennas are considered.

At last, an effective strategy of using reconfigurable directional couplers is adopted to address the beam splitting issue of the generalized joined coupler (GJC) matrix and to achieve arbitrarily and individually scannable multibeams. To this end, a flexible synchronized optimization strategy that can consider multiple different cases was developed. Synthesized results have demonstrated that, by using the developed optimization strategy, beam splitting issue when beam overlapping can be well solved. Besides, multiple different cases with differently scanned multibeams can be optimized at a time to achieve global optimum and stable SLLs as well as consistent gains for all the beams. Comparison with a classical Blass matrix design method has further validated the effectiveness of the developed method.

Since modern wireless communication systems are evolving to be high-integration and low-cost ones, it is believed that the developed techniques that can lead to simplified and cost-effective feeding systems can be very attractive in many applications in current and future terrestrial and non-terrestrial wireless communication networks.

8.2 Future Work

There are some interesting works deserving further investigation in the future:

1. Wide-angle beam scanning employing the GJC matrix. Wide-angle beam scanning can find significant applications in the fifth-generation (5G) and future wireless communications such as sensing, satellite communication, smart vehicles, and air-based platforms, including unmanned aerial vehicle (UAVs) and aircraft. The gain at large scanning angles usually drops significantly due to the gain drop of the element pattern. By properly designing the GJC matrix, the gain decrease can be compensated at large scanning angles to achieve beam scanning with consistent gain. It would be very useful if a large range beam scanning can be achieved.

2. 2D wide-angle beam scanning conformal array synthesis employing the GJC matrix.

In some wireless communication systems, such as the UAVs, antenna arrays are required to be integrated into a curved shape to maintain the aerodynamic or hydrodynamic requirements. In this case, linear or planar arrays are no longer applicable. Conformal arrays that are able to achieve wide 2D wide-angle beam scanning are highly desired in these applications. By connecting series-fed 1D antenna arrays to each output port of the GJC matrix, it is possible to achieve 2D wide-angle beam scanning. By employing a cylindrical conformal array, it is also possible to achieve full 360° azimuth beam scanning and also wide-angle beam scanning in the elevation plane.

BIBLIOGRAPHY

[1] J. Kraus and R. Marhefka, *Antennas for All Applications*. McGraw-Hill, 2002.

[2] C. Balanis, *Antenna Theory: Analysis and Design*. John Wiley & Sons, 2016.

[3] R. J. Mailloux, *Phased Array Antenna Handbook*. Artech House, 2017.

[4] S. A. Schelkunoff, "A mathematical theory of linear arrays," *The Bell System Technical Journal*, vol. 22, no. 1, pp. 80–107, 1943.

[5] T. Taylor, "Design of line-source antennas for narrow beamwidth and low side lobes," *Transactions of the IRE Professional Group on Antennas and Propagation*, vol. 3, no. 1, pp. 16–28, 1955.

[6] B. Fuchs, A. Skrivervik, and J. R. Mosig, "Shaped beam synthesis of arrays via sequential convex optimizations," *IEEE Antennas and Wireless Propagation Letters*, vol. 12, pp. 1049–1052, 2013.

[7] P. Woodward, "A method of calculating the field over a plane aperture required to produce a given polar diagram," *Journal of the Institution of Electrical Engineers-Part IIIA: Radiolocation*, vol. 93, no. 10, pp. 1554–1558, 1946.

[8] M. M. Khodier and C. G. Christodoulou, "Linear array geometry synthesis with minimum sidelobe level and null control using particle swarm optimization," *IEEE Transactions on Antennas and propagation*, vol. 53, no. 8, pp. 2674–2679, 2005.

[9] P. Y. Zhou and M. A. Ingram, "Pattern synthesis for arbitrary arrays using an adaptive array method," *IEEE Transactions on Antennas and Propagation*, vol. 47, no. 5, pp. 862–869, 1999.

[10] Y. Han, C. Wan, W. Sheng, B. Tian, and H. Yang, "Array synthesis using weighted alternating projection and proximal splitting," *IEEE Antennas and Wireless Propagation Letters*, vol. 14, pp. 1006–1009, 2015.

[11] J.-Y. Li, Y.-X. Qi, and S.-G. Zhou, "Shaped beam synthesis based on superposition principle and Taylor method," *IEEE Transactions on Antennas and Propagation*, vol. 65, no. 11, pp. 6157–6160, 2017.

[12] P. Woodward and J. Lawson, "The theoretical precision with which an arbitrary radiation-pattern may be obtained from a source of finite size," *Journal of the Institution of Electrical Engineers-Part III: Radio and Communication Engineering*, vol. 95, no. 37, pp. 363–370, 1948.

[13] J. L. A. Quijano and G. Vecchi, "Alternating adaptive projections in antenna synthesis," *IEEE transactions on antennas and propagation*, vol. 58, no. 3, pp. 727–737, 2009.

[14] A. Haddadi, A. Ghorbani, and J. Rashed-Mohassel, "Cosecant-squared pattern synthesis using a weighted alternating reverse projection method," *IET microwaves, antennas & propagation*, vol. 5, no. 15, pp. 1789–1795, 2011.

[15] W. T. Li, Y. Q. Hei, J. Yang, and X. W. Shi, "Synthesis of multiple-pattern planar arrays with a hybrid generalised iterative fast Fourier transform algorithm," *IET Microwaves, Antennas & Propagation*, vol. 10, no. 1, pp. 16–24, 2016.

[16] Y. Liu, X. Huang, K. Da Xu, Z. Song, S. Yang, and Q. H. Liu, "Pattern synthesis of unequally spaced linear arrays including mutual coupling using iterative FFT

via virtual active element pattern expansion," *IEEE Transactions on Antennas and Propagation*, vol. 65, no. 8, pp. 3950–3958, 2017.

[17] J. I. Echeveste, M. A. G. de Aza, and J. Zapata, "Shaped beam synthesis of real antenna arrays via finite-element method, floquet modal analysis, and convex programming," *IEEE Transactions on Antennas and Propagation*, vol. 64, no. 4, pp. 1279–1286, 2016.

[18] B. Fuchs, "Application of convex relaxation to array synthesis problems," *IEEE Transactions on Antennas and Propagation*, vol. 62, no. 2, pp. 634–640, 2013.

[19] M. Li, Y. Liu, S.-L. Chen, P.-Y. Qin, and Y. J. Guo, "Low sidelobe synthesis of dipole arrays by element orientation selection using binary codec genetic algorithm," in *2017 11th European Conference on Antennas and Propagation (EUCAP)*, pp. 2838–2840, IEEE, 2017.

[20] M. Li, Y. Liu, and Y. J. Guo, "Shaped power pattern synthesis of a linear dipole array by element rotation and phase optimization using dynamic differential evolution," *IEEE Antennas and Wireless Propagation Letters*, vol. 17, no. 4, pp. 697–701, 2018.

[21] J. I. Echeveste, J. Rubio, M. Á. G. de Aza, and C. Craeye, "Pattern synthesis of coupled antenna arrays via element rotation," *IEEE Antennas and Wireless Propagation Letters*, vol. 16, pp. 1707–1710, 2017.

[22] A. B. Smolders and U. Johannsen, "Axial ratio enhancement for circularly-polarized millimeter-wave phased-arrays using a sequential rotation technique," *IEEE Transactions on Antennas and Propagation*, vol. 59, no. 9, pp. 3465–3469, 2011.

[23] A. Smolders and H. Visser, "Low side-lobe circularly-polarized phased arrays using a random sequential rotation technique," *IEEE Transactions on Antennas and Propagation*, vol. 62, no. 12, pp. 6476–6481, 2014.

[24] R. L. Haupt and D. W. Aten, "Low sidelobe arrays via dipole rotation," *IEEE Transactions on Antennas and Propagation*, vol. 57, no. 5, pp. 1575–1579, 2009.

[25] Y. Guo and R. Ziolkowski, *Advanced Antenna Array Engineering for 6G and Beyond Wireless Communications*. John Wiley & Sons, 2021.

[26] W. Hong, Z. H. Jiang, C. Yu, J. Zhou, P. Chen, Z. Yu, H. Zhang, B. Yang, X. Pang, M. Jiang, *et al.*, "Multibeam antenna technologies for 5G wireless communications," *IEEE Transactions on Antennas and Propagation*, vol. 65, no. 12, pp. 6231–6249, 2017.

[27] M. I. Skolnik, *Radar Handbook*. McGraw-Hill Education, 2008.

[28] C. L. Dolph, "A current distribution for broadside arrays which optimizes the relationship between beam width and side-lobe level," *Proceedings of the IRE*, vol. 34, no. 6, pp. 335–348, 1946.

[29] E. T. Bayliss, "Design of monopulse antenna difference patterns with low sidelobes," *Bell System Technical Journal*, vol. 47, no. 5, pp. 623–650, 1968.

[30] G. Bellizzi and O. M. Bucci, "On the optimal synthesis of sum or difference patterns of centrosymmetric arrays under arbitrary sidelobe constraints," *IEEE Transactions on Antennas and Propagation*, vol. 66, no. 9, pp. 4620–4626, 2018.

[31] D. McNamara, "Synthesis of sum and difference patterns for two-section monopulse arrays," in *IEE Proceedings H (Microwaves, Antennas and Propagation)*, vol. 135, pp. 371–374, IET, 1988.

[32] S. Kwak, J. Chun, D. Park, Y. K. Ko, and B. L. Cho, "Asymmetric sum and difference beam pattern synthesis with a common weight vector," *IEEE Antennas and Wireless Propagation Letters*, vol. 15, pp. 1622–1625, 2016.

[33] A. F. Morabito and P. Rocca, "Reducing the number of elements in phase-only reconfigurable arrays generating sum and difference patterns," *IEEE Antennas and Wireless Propagation Letters*, vol. 14, pp. 1338–1341, 2015.

[34] A. F. Morabito and P. Rocca, "Optimal synthesis of sum and difference patterns with arbitrary sidelobes subject to common excitations constraints," *IEEE Antennas and Wireless Propagation Letters*, vol. 9, pp. 623–626, 2010.

[35] L. Manica, P. Rocca, and A. Massa, "On the synthesis of sub-arrayed planar array antennas for tracking radar applications," *IEEE Antennas and Wireless Propagation Letters*, vol. 7, pp. 599–602, 2008.

[36] P. Rocca, L. Manica, R. Azaro, and A. Massa, "A hybrid approach to the synthesis of subarrayed monopulse linear arrays," *IEEE transactions on antennas and propagation*, vol. 57, no. 1, pp. 280–283, 2009.

[37] S. Caorsi, A. Massa, M. Pastorino, and A. Randazzo, "Optimization of the difference patterns for monopulse antennas by a hybrid real/integer-coded differential evolution method," *IEEE Transactions on Antennas and Propagation*, vol. 53, no. 1, pp. 372–376, 2005.

[38] P. Lopez, J. Rodriguez, F. Ares, and E. Moreno, "Subarray weighting for the difference patterns of monopulse antennas: Joint optimization of subarray configurations and weights," *IEEE Transactions on Antennas and Propagation*, vol. 49, no. 11, pp. 1606–1608, 2001.

[39] P. Rocca, L. Manica, and A. Massa, "An improved excitation matching method based on an ant colony optimization for suboptimal-free clustering in sum-difference compromise synthesis," *IEEE Transactions on Antennas and Propagation*, vol. 57, no. 8, pp. 2297–2306, 2009.

[40] H. Oraizi and M. Fallahpour, "Sum, difference and shaped beam pattern synthesis by non-uniform spacing and phase control," *IEEE Transactions on Antennas and Propagation*, vol. 59, no. 12, pp. 4505–4511, 2011.

[41] A. Trastoy and F. Ares, "Phase-only control of antenna sum patterns," *Progress In Electromagnetics Research*, vol. 30, pp. 47–57, 2001.

[42] P. Yang, F. Yan, F. Yang, and T. Dong, "Microstrip phased-array in-band RCS reduction with a random element rotation technique," *IEEE Transactions on Antennas and Propagation*, vol. 64, no. 6, pp. 2513–2518, 2016.

[43] K. Tsui and S. Chan, "Pattern synthesis of narrowband conformal arrays using iterative second-order cone programming," *IEEE Transactions on Antennas and Propagation*, vol. 58, no. 6, pp. 1959–1970, 2010.

[44] Y. Liu, J. Bai, K. Da Xu, Z. Xu, F. Han, Q. H. Liu, and Y. J. Guo, "Linearly polarized shaped power pattern synthesis with sidelobe and cross-polarization control by using semidefinite relaxation," *IEEE Transactions on Antennas and Propagation*, vol. 66, no. 6, pp. 3207–3212, 2018.

[45] F. J. Ares-Pena, J. A. Rodriguez-Gonzalez, E. Villanueva-Lopez, and S. Rengarajan, "Genetic algorithms in the design and optimization of antenna array patterns," *IEEE Transactions on Antennas and Propagation*, vol. 47, no. 3, pp. 506–510, 1999.

[46] P. You, Y. Liu, K. Xu, C. Zhu, and Q. H. Liu, "Generalisation of genetic algorithm and fast Fourier transform for synthesising unequally spaced linear array shaped pattern including coupling effects," *IET Microwaves, Antennas & Propagation*, vol. 11, no. 6, pp. 827–832, 2017.

[47] S. Yang, Y. B. Gan, and T. P. Khiang, "A new technique for power-pattern synthesis in time-modulated linear arrays," *IEEE Antennas and Wireless Propagation Letters*, vol. 2, pp. 285–287, 2003.

[48] A. A. Akdagli, K. Guney, and D. Karaboga, "Touring ant colony optimization algorithm for shaped-beam pattern synthesis of linear antenna," *Electromagnetics*, vol. 26, no. 8, pp. 615–628, 2006.

[49] A. Pirhadi, M. H. Rahmani, and A. Mallahzadeh, "Shaped beam array synthesis using particle swarm optimisation method with mutual coupling compensation and wideband feeding network," *IET Microwaves, Antennas & Propagation*, vol. 8, no. 8, pp. 549–555, 2014.

[50] L. Marcaccioli, R. Sorrentino, and R. Vincenti Gatti, "Series expansion method for phase-only shaped beam synthesis and adaptive nulling," *Series expansion method for phase-only shaped beam synthesis and adaptive nulling*, pp. 1000–1004, 2004.

[51] D. P. Scholnik, "A parameterized pattern-error objective for large-scale phase-only array pattern design," *IEEE Transactions on Antennas and Propagation*, vol. 64, no. 1, pp. 89–98, 2015.

[52] J. Liang, X. Fan, W. Fan, D. Zhou, and J. Li, "Phase-only pattern synthesis for linear antenna arrays," *IEEE Antennas and Wireless Propagation Letters*, vol. 16, pp. 3232–3235, 2017.

[53] O. M. Bucci, T. Isernia, and A. F. Morabito, "An effective deterministic procedure for the synthesis of shaped beams by means of uniform-amplitude linear sparse arrays," *IEEE Transactions on Antennas and Propagation*, vol. 61, no. 1, pp. 169–175, 2012.

[54] L. I. Vaskelainen, "Constrained least-squares optimization in conformal array antenna synthesis," *IEEE Transactions on antennas and propagation*, vol. 55, no. 3, pp. 859–867, 2007.

[55] B. Fuchs, "Shaped beam synthesis of arbitrary arrays via linear programming," *IEEE Antennas and Wireless Propagation Letters*, vol. 9, pp. 481–484, 2010.

[56] G. Oliveri, E. T. Bekele, F. Robol, and A. Massa, "Sparsening conformal arrays through a versatile BCS-based method," *IEEE transactions on antennas and propagation*, vol. 62, no. 4, pp. 1681–1689, 2013.

[57] O. Bucci, A. Capozzoli, and G. D'elia, "Power pattern synthesis of reconfigurable conformal arrays with near-field constraints," *IEEE Transactions on Antennas and Propagation*, vol. 52, no. 1, pp. 132–141, 2004.

[58] Z. Xu, Y. Liu, M. Li, and Y. Li, "Linearly polarized shaped power pattern synthesis with dynamic range ratio control for arbitrary antenna arrays," *IEEE Access*, vol. 7, pp. 53621–53628, 2019.

[59] L. Josefsson and P. Persson, "Conformal array synthesis including mutual coupling," *Electronics Letters*, vol. 35, no. 8, pp. 625–627, 1999.

[60] Z.-C. Hao, M. He, and W. Hong, "Design of a millimeter-wave high angle selectivity shaped-beam conformal array antenna using hybrid genetic/space mapping method," *IEEE Antennas and Wireless Propagation Letters*, vol. 15, pp. 1208–1212, 2015.

[61] J. Ferreira and F. Ares, "Pattern synthesis of conformal arrays by the simulated annealing technique," *Electronics Letters*, vol. 33, no. 14, pp. 1187–1189, 1997.

[62] Y. J. Guo, M. Ansari, and N. J. Fonseca, "Circuit type multiple beamforming networks for antenna arrays in 5G and 6G terrestrial and non-terrestrial networks," *IEEE Journal of Microwaves*, vol. 1, no. 3, pp. 704–722, 2021.

[63] K. Sultan, M. Ikram, and N. Nguyen-Trong, "A multiband multibeam antenna for sub-6 GHz and mm-wave 5G applications," *IEEE Antennas and Wireless Propagation Letters*, vol. 21, no. 6, pp. 1278–1282, 2022.

[64] D. Gomez-Barquero, D. Navrátil, S. Appleby, and M. Stagg, "Point-to-multipoint communication enablers for the fifth generation of wireless systems," *IEEE Communications Standards Magazine*, vol. 2, no. 1, pp. 53–59, 2018.

[65] S. Gong, X. Lu, D. T. Hoang, D. Niyato, L. Shu, D. I. Kim, and Y.-C. Liang, "Toward smart wireless communications via intelligent reflecting surfaces: A contemporary survey," *IEEE Communications Surveys & Tutorials*, vol. 22, no. 4, pp. 2283–2314, 2020.

[66] M. Nosrati, S. Shahsavari, S. Lee, H. Wang, and N. Tavassolian, "A concurrent dual-beam phased-array Doppler radar using MIMO beamforming techniques for short-range vital-signs monitoring," *IEEE Transactions on Antennas and Propagation*, vol. 67, no. 4, pp. 2390–2404, 2019.

[67] J.-F. Li, Z. N. Chen, D.-L. Wu, G. Zhang, and Y.-J. Wu, "Dual-beam filtering patch antennas for wireless communication application," *IEEE Transactions on Antennas and Propagation*, vol. 66, no. 7, pp. 3730–3734, 2018.

[68] A. Khidre, K.-F. Lee, A. Z. Elsherbeni, and F. Yang, "Wide band dual-beam U-slot microstrip antenna," *IEEE transactions on antennas and propagation*, vol. 61, no. 3, pp. 1415–1418, 2013.

[69] C. Chen, Y. Guo, and H. Wang, "Wideband symmetrical cross-shaped probe dual-beam microstrip patch antenna," *IEEE Antennas and Wireless Propagation Letters*, vol. 14, pp. 622–625, 2014.

[70] Y.-S. Yeh and B. A. Floyd, "Multibeam phased-arrays using dual-vector distributed beamforming: Architecture overview and 28 GHz transceiver prototypes," *IEEE Transactions on Circuits and Systems I: Regular Papers*, vol. 67, no. 12, pp. 5496–5509, 2020.

[71] Y. Yu, W. Hong, Z. H. Jiang, H. Zhang, and C. Guo, "Multibeam generation and measurement of a DDS-based digital beamforming array transmitter at Ka-band," *IEEE Transactions on Antennas and Propagation*, vol. 67, no. 5, pp. 3030–3039, 2019.

[72] M. Comisso and R. Vescovo, "Fast iterative method of power synthesis for antenna arrays," *IEEE Transactions on Antennas and Propagation*, vol. 57, no. 7, pp. 1952–1962, 2009.

[73] M. Khalaj-Amirhosseini, "Synthesis of concurrent multibeam and conical beam antenna arrays," *International Journal of RF and Microwave Computer-Aided Engineering*, vol. 29, no. 12, p. e21966, 2019.

[74] M. Mouhamadou, P. Vaudon, and M. Rammal, "Smart antenna array patterns synthesis: Null steering and multi-user beamforming by phase control," *Progress In Electromagnetics Research*, vol. 60, pp. 95–106, 2006.

[75] D. Marcano, F. Duran, and O. Chang, "Synthesis of multiple beam linear antenna arrays using genetic algorithms," in *IEEE Antennas and Propagation Society International Symposium. 1995 Digest*, vol. 2, pp. 938–941, IEEE, 1995.

[76] M. Comisso, G. Palese, F. Babich, F. Vatta, and G. Buttazzoni, "3D multi-beam and null synthesis by phase-only control for 5G antenna arrays," *Electronics*, vol. 8, no. 6, p. 656, 2019.

[77] L. Cui, S. Qi, W. Wu, and D. Fang, "Dual-beam array antenna based on circular patch elements with conical beam pattern," *Progress In Electromagnetics Research M*, vol. 36, pp. 93–99, 2014.

[78] R. Ghayoula, N. Fadlallah, A. Gharsallah, and M. Rammal, "Phase-only adaptive nulling with neural networks for antenna array synthesis," *IET microwaves, antennas & propagation*, vol. 3, no. 1, pp. 154–163, 2009.

[79] X. Zhang, Z. He, B. Liao, X. Zhang, and W. Peng, "Pattern synthesis for arbitrary arrays via weight vector orthogonal decomposition," *IEEE Transactions on Signal Processing*, vol. 66, no. 5, pp. 1286–1299, 2017.

[80] Y. Hu, J. Zhan, Z. H. Jiang, C. Yu, and W. Hong, "An orthogonal hybrid analog–digital multibeam antenna array for millimeter-wave massive MIMO systems," *IEEE Transactions on Antennas and Propagation*, vol. 69, no. 3, pp. 1393–1403, 2020.

[81] Y. Hu, W. Hong, C. Yu, Y. Yu, H. Zhang, Z. Yu, and N. Zhang, "A digital multibeam array with wide scanning angle and enhanced beam gain for millimeter-wave massive MIMO applications," *IEEE Transactions on Antennas and Propagation*, vol. 66, no. 11, pp. 5827–5837, 2018.

[82] L. Kuai, J. Chen, Z. H. Jiang, C. Yu, C. Guo, Y. Yu, H.-X. Zhou, and W. Hong, "A N260 band 64 channel millimeter wave full-digital multi-beam array for 5G massive MIMO applications," *IEEE Access*, vol. 8, pp. 47640–47653, 2020.

[83] B. Yang, Z. Yu, J. Lan, R. Zhang, J. Zhou, and W. Hong, "Digital beamforming-based massive MIMO transceiver for 5G millimeter-wave communications," *IEEE Transactions on Microwave Theory and Techniques*, vol. 66, no. 7, pp. 3403–3418, 2018.

[84] J. Butler, "Beam-forming matrix simplifies design of electronically scanned antenna," *Electron. Design*, vol. 9, pp. 170–173, 1961.

[85] Y. Cao, K.-S. Chin, W. Che, W. Yang, and E. S. Li, "A compact 38 GHz multibeam antenna array with multifolded butler matrix for 5G applications," *IEEE Antennas and Wireless Propagation Letters*, vol. 16, pp. 2996–2999, 2017.

[86] S.-K. Zhao, M. Lv, Z.-y. Zhang, Q. Chen, and G. Fu, "Planar two-dimensional scanning multibeam array antenna based on a 3× 3 butler matrix network," *IEEE Antennas and Wireless Propagation Letters*, vol. 21, no. 6, pp. 1163–1167, 2022.

[87] A. M. A. Najafabadi, F. A. Ghani, and I. Tekin, "Low-cost multibeam millimeter-wave array antennas for 5G mobile applications," *IEEE Transactions on Vehicular Technology*, 2022.

[88] C. Liu, S. Xiao, Y.-X. Guo, M.-C. Tang, Y.-Y. Bai, and B.-Z. Wang, "Circularly polarized beam-steering antenna array with butler matrix network," *IEEE Antennas and Wireless Propagation Letters*, vol. 10, pp. 1278–1281, 2011.

[89] J. Blass, "Multidirectional antenna-A new approach to stacked beams," in *1958 IRE International Convention Record*, vol. 8, pp. 48–50, IEEE, 1966.

[90] J. Nolen, "Synthesis of multiple beam networks for arbitrary illuminations," *Bendix*, 1965.

[91] H. Ren, H. Zhang, Y. Jin, Y. Gu, and B. Arigong, "A novel 2-d 3×3 Nolen matrix for 2-d beamforming applications," *IEEE Transactions on Microwave Theory and Techniques*, vol. 67, no. 11, pp. 4622–4631, 2019.

[92] P. Li, H. Ren, and B. Arigong, "A symmetric beam-phased array fed by a Nolen matrix using 180◦ couplers," *IEEE Microwave and Wireless Components Letters*, vol. 30, no. 4, pp. 387–390, 2020.

[93] N. J. Fonseca, "Printed S-band 4×4 Nolen matrix for multiple beam antenna applications," *IEEE transactions on antennas and propagation*, vol. 57, no. 6, pp. 1673–1678, 2009.

[94] C. A. Guo and Y. J. Guo, "A general approach for synthesizing multibeam antenna arrays employing generalized joined coupler matrix," *IEEE Transactions on Antennas and Propagation*, vol. 70, no. 9, pp. 7556–7564, 2022.

[95] C. A. Guo, Y. J. Guo, H. Zhu, W. Ni, and J. Yuan, "Optimization of multibeam antennas employing generalized joined coupler matrix," *IEEE Transactions on Antennas and Propagation*, 2022.

[96] J. A. Zhang, X. Huang, Y. J. Guo, J. Yuan, and R. W. Heath, "Multibeam for joint communication and radar sensing using steerable analog antenna arrays," *IEEE Transactions on Vehicular Technology*, vol. 68, no. 1, pp. 671–685, 2018.

[97] J. A. Zhang, M. L. Rahman, K. Wu, X. Huang, Y. J. Guo, S. Chen, and J. Yuan, "Enabling joint communication and radar sensing in mobile networks,ÄîA survey," *IEEE Communications Surveys & Tutorials*, vol. 24, no. 1, pp. 306–345, 2021.

[98] Y. Luo, J. A. Zhang, X. Huang, W. Ni, and J. Pan, "Multibeam optimization for joint communication and radio sensing using analog antenna arrays," *IEEE Transactions on Vehicular Technology*, vol. 69, no. 10, pp. 11000–11013, 2020.

[99] Q. Wang, R. Gao, and S. Liu, "Mapping-based optimization method for pattern synthesis via array element rotation," *IEEE Transactions on Antennas and Propagation*, vol. 68, no. 4, pp. 2736–2742, 2019.

[100] Y. Liu, M. Li, R. L. Haupt, and Y. J. Guo, "Synthesizing shaped power patterns for linear and planar antenna arrays including mutual coupling by refined joint rotation/phase optimization," *IEEE Transactions on Antennas and Propagation*, vol. 68, no. 6, pp. 4648–4657, 2020.

[101] M. Li, Y. Liu, S.-L. Chen, J. Hu, and Y. J. Guo, "Synthesizing shaped-beam cylindrical conformal array considering mutual coupling using refined rotation/phase optimization," *IEEE Transactions on Antennas and Propagation*, vol. 70, no. 11, pp. 10543–10553, 2022.

[102] Y. Shi *et al.*, "Particle swarm optimization: developments, applications and resources," in *Proceedings of the 2001 congress on evolutionary computation (IEEE Cat. No. 01TH8546)*, vol. 1, pp. 81–86, IEEE, 2001.

[103] P. Nayeri, F. Yang, and A. Z. Elsherbeni, "Design of single-feed reflectarray antennas with asymmetric multiple beams using the particle swarm optimization method," *IEEE Transactions on Antennas and Propagation*, vol. 61, no. 9, pp. 4598–4605, 2013.

[104] M. D'Urso and T. Isernia, "Solving some array synthesis problems by means of an effective hybrid approach," *IEEE transactions on antennas and propagation*, vol. 55, no. 3, pp. 750–759, 2007.

[105] A. Corporation, "Ansoft high frequency structure simulation (HFSS)," *Version 13*, 2010.

[106] D. F. Kelley and W. L. Stutzman, "Array antenna pattern modeling methods that include mutual coupling effects," *IEEE Transactions on antennas and propagation*, vol. 41, no. 12, pp. 1625–1632, 1993.

[107] S. Weigand, G. H. Huff, K. H. Pan, and J. T. Bernhard, "Analysis and design of broad-band single-layer rectangular U-slot microstrip patch antennas," *IEEE transactions on antennas and propagation*, vol. 51, no. 3, pp. 457–468, 2003.

[108] J. I. Echeveste, M. Á. G. de Aza, J. Rubio, and J. Zapata, "Near-optimal shaped-beam synthesis of real and coupled antenna arrays via 3-D-FEM and phase retrieval," *IEEE Transactions on Antennas and Propagation*, vol. 64, no. 6, pp. 2189–2196, 2016.

[109] B. P. Lamichhane, "Finite element techniques for removing the mixture of Gaussian and impulsive noise," *IEEE Transactions on Signal Processing*, vol. 57, no. 7, pp. 2538–2547, 2009.

[110] W. P. Keizer, "Low-sidelobe pattern synthesis using iterative Fourier techniques coded in MATLAB [EM programmer's notebook]," *IEEE Antennas and Propagation Magazine*, vol. 51, no. 2, pp. 137–150, 2009.

[111] Y. Liu, J. Zheng, M. Li, Q. Luo, Y. Rui, and Y. J. Guo, "Synthesizing beam-scannable thinned massive antenna array utilizing modified iterative FFT for millimeter-wave communication," *IEEE Antennas and Wireless Propagation Letters*, vol. 19, no. 11, pp. 1983–1987, 2020.

[112] W. P. Keizer, "Fast low-sidelobe synthesis for large planar array antennas utilizing successive fast Fourier transforms of the array factor," *IEEE transactions on Antennas and Propagation*, vol. 55, no. 3, pp. 715–722, 2007.

[113] W. P. Keizer, "Large planar array thinning using iterative FFT techniques," *IEEE Transactions on Antennas and Propagation*, vol. 57, no. 10, pp. 3359–3362, 2009.

[114] M. Li, Y. Liu, Z. Bao, L. Chen, J. Hu, and Y. J. Guo, "Efficient phase-only dual- and multi-beam pattern synthesis with accurate beam direction and power control employing partitioned iterative fft," *IEEE Transactions on Antennas and Propagation*, vol. 71, no. 4, pp. 3719–3724, 2023.

[115] W. P. Keizer, "Low sidelobe phased array pattern synthesis with compensation for errors due to quantized tapering," *IEEE Transactions on Antennas and Propagation*, vol. 59, no. 12, pp. 4520–4524, 2011.

[116] M. Comisso and R. Vescovo, "Multi-beam synthesis with null constraints by phase control for antenna arrays of arbitrary geometry," *Electronics Letters*, vol. 43, no. 7, p. 1, 2007.

[117] S. Ahmed, J. S. Thompson, Y. R. Petillot, and B. Mulgrew, "Finite alphabet constant-envelope waveform design for mimo radar," *IEEE Transactions on Signal Processing*, vol. 59, no. 11, pp. 5326–5337, 2011.

[118] J.-U. Yoo and H.-W. Son, "A simple compact wideband microstrip antenna consisting of three staggered patches," *IEEE Antennas and Wireless Propagation Letters*, vol. 19, no. 12, pp. 2038–2042, 2020.

[119] C. Cui, W. T. Li, X. T. Ye, and X. W. Shi, "Hybrid genetic algorithm and modified iterative Fourier transform algorithm for large thinned array synthesis," *IEEE Antennas and Wireless Propagation Letters*, vol. 16, pp. 2150–2154, 2017.

[120] T. Zhang and W. Che, "A compact reconfigurable coupler with tunable coupling coefficients and frequencies," *IEEE Microwave and Wireless Components Letters*, vol. 27, no. 2, pp. 129–131, 2017.

[121] M. Li, Y. Liu, and Y. J. Guo, "Design of sum and difference patterns by optimizing element rotations and positions for linear dipole array," *IEEE Transactions on Antennas and Propagation*, vol. 69, no. 5, pp. 3027–3032, 2020.

[122] S. Mosca, F. Bilotti, A. Toscano, and L. Vegni, "A novel design method for Blass matrix beam-forming networks," *IEEE Transactions on Antennas and Propagation*, vol. 50, no. 2, pp. 225–232, 2002.